Technical University of Denmark

DTU

Microwave Receivers for Fast-Ion Detection in Fusion Plasmas

Furtula, Vedran; Michelsen, Poul; Leipold, Frank; Johansen, Tom Keinicke

Publication date:
2012

Document Version
Publisher's PDF, also known as Version of record

Link back to DTU Orbit

DTU Library
Technical Information Center of Denmark

Microwave Receivers for Fast-Ion Detection in Fusion Plasmas

PhD-Report

Vedran Furtula
PhD Thesis
February 2012

DTU Physics
Department of Physics

Author: Vedran Furtula
Title: Microwave Receivers for Fast-Ion Detection in Fusion
Plasmas
Division: Fusion and Plasma Physics

Contents

Abstract

The main objectives of this thesis are to determine fundamental properties of a millimeter-wave radiometer used to detect radiation associated with dynamics of fast ions and to investigate possibilities for improvements and new designs. The detection of fast ions is based on a principle called collective Thomson scattering (CTS). The Danish CTS group has been involved in fusion plasma experiments for more than 10 years and the future plans will most probably include the International Thermonuclear Experimental Reactor (ITER). Current CTS systems designed by the Danish group are specified for the frequency range from 100 to 110 GHz.

In this thesis we follow the path of the radiation from a fusion plasma to the data acquisition unit. Firstly, the scattered radiation passes through the quasi-optical system. Quasi-optical elements required to be installed on the high field side (HFS) on the ITER are assessed. For the ITER HFS receiver we have designed and measured the quasi-optical components that form a transmission link between the plasma and the radio frequency (RF) electronics. This HFS receiver is required to resolve the near parallel velocity components created by the alpha particles. Secondly, the radiation will encounter the RF part. This part is not yet designed for ITER, but instead the solution is addressed to the CTS receiver installed at ASDEX Upgrade (AUG). We have put effort to thoroughly examine and evaluate the performance of the receiver components and the receiver as an assembled unit. We have measured and analyzed all the receiver components starting from the two notch filters to the fifty square-law detector diodes. The receiver sensitivity is calculated from the system measurements and compared with the expected sensitivity based on the individual component measurements.

Besides the system considerations we have also studied improvements of two critical components of the receiver. The first component is the notch filter, which is needed to block strong probing radiation coming from a gyrotron. The newly designed notch filters within the scope of this thesis are superior to their predecessors and are installed in the CTS receiver. A filter was subsequently designed, built, and tested by the CTS group and installed by the German ECE group at AUG. Our filter enables the ECE group to make measurements in the frequency range corresponding to the gyrotron operation. The second component is the mixer. The conversion loss of the mixer, together with loss in waveguide components and quasi-optic parts, is the main contributor to the noise and thereby degrades the signal-to-noise ratio. The architecture of the mixer is a subharmonic type, optimized to be driven by a double local oscillator (LO) frequency in order to downshift the RF to intermediate frequency (IF). The simulated results are presented for the case of 140 GHz, which is relevant for a number of fusion plasma diagnostics such as ECE and interrogation of neo-classical tearing modes (NTM).

Finally, conclusions are drawn and future aspects presented. This study seeks to give insights towards new solutions and improvements of the existing CTS receiver architecture.

Acknowledgments

Nomenclature

List of abbreviations

ADS	Advanced Design System
ASDEX	Axially Symmetric Divertor EXperiment
AUG	ASDEX Upgrade
BPF	Bandpass filter
BS	Backscattering
BW	Bandwidth
CST	Computer Simulation Technology
CTS	Collective Thomson scattering
DC	Direct current
DR	Dicke radiometer
ECCD	Electron cyclotron current drive
ECE	Electron cyclotron emission
ECRH	Electron cyclotron resonance heating
eV	Electron volt ($1.602 \cdot 10^{-19}$ Joule)
FS	Forward scattering
GaAs	Gallium Arsenide
GHz	Gigahertz (10^9 Hertz)
HB	Harmonic balance
HEMT	High Electron Mobility Transistors
HFS	High field side
HPF	Highpass filter
IF	Intermediate frequency
InP	Indium Phosphide
IO	ITER Organization
ITER	International Thermonuclear Experimental Reactor
JET	Joint European Torus
LFS	Low field side
LNA	Low noise amplifier
LO	Local oscillator
LPF	Lowpass filter
mHEMT	metamorphic HEMT
MMIC	Microwave Monolithic Integrated Circuit
MHz	Megahertz (10^6 Hertz)
mm-WAVE	Millimeter wave
MOSFET	Metal Oxide Semiconductor Field Effect Transistor
NBI	Neutral beam injection
NF	Noise figure

NIR	Noise injection radiometer
NTM	Neo-classical tearing modes
PA	Power amplifier
pHEMT	pseudomorphic HEMT
RF	Radio frequency
SHM	Subharmonic mixer
SNR	Signal-to-noise ratio
TE	Transverse electric
TEXTOR	Tokamak Experiment for Technology Oriented Research
TM	Transverse magnetic
TOKAMAK	Toroidal'Naja Kamera v Magnitnych Katusjkach
TFTR	Tokamak Fusion Test Reactor
TPR	Total power radiometer

List of symbols

$\mathbf{E}$	Electric field vector
$\mathbf{B}$	Magnetic field vector
q	Tokamak safety factor
q_e	Electron charge
n_e	Electron density
m_e	Electron mass
m_i	Ion mass
T_e	Electron Temperature
T_i	Ion Temperature
λ	Wavelength in a medium
λ_0	Wavelength in a vacuum
λ_D	Debye length
$\mathbf{k}$	Wave vector
$\mathbf{k}^i$	Wave vector of incident radiation
$\mathbf{k}^s$	Wave vector of scattered radiation
$\mathbf{k}^\delta$	Wave vector of resolved fluctuation
ω	Angular frequency
ω^i	Angular frequency of incident radiation
ω^s	Angular frequency of scattered radiation
ω^δ	Angular frequency of resolved fluctuation
ω_p	Plasma frequency
α	Salpeter parameter
R	Tokamak radial coordinate
z	Tokamak vertical coordinate
θ	Poloidal tokamak angle
ϕ	Toroidal tokamak angle
σ	Electrical conductivity
τ_E	Plasma confinement time

Chapter 1

Introduction

The still growing world population and its increasing social and business activities in almost all regions of the world demand consumption of energy. In spite of the warnings from many independent energy research centers that humans rely heavily on energy sources from fossil fuels, limited progress has been achieved towards sustainable energy sources. However, the demand for more energy is increasing all over the world with highest growth rates in the fast developing countries known as BRIC (Brazil, Russia, India and China). Figure 1.1 shows consumption of energy in the World as function of time. In the years from 1990 to 2008 we have observed an increased consumption of all energy sources, especially coal and oil. In the mean time, the production of nuclear fission energy has the lowest growth rate, despite the fact that it is an energy source with no production of greenhouse gases. In the years from 2008 to 2035 we see projections of possible energy consumption showing growth in the consumption of all energy sources including fission.

Energy from oil, coal and similar fossil fuels are diminishing relatively fast which makes them unfit for energy plans for future generations [61]. The best solution would be to have a sustainable energy source that could fulfill the energy consumption needs for all times. This is for sure not an easy task, but we have come closer to a solution. Fusion provides a safe solution to exploit an unlimited source of clean energy. This thesis is dedicated to the design of microwave components used in diagnostic systems for analysis of fusion plasmas and hopefully provides a small step in human kind's fusion energy quest.

1.1 Thermonuclear energy

The main objective in fusion science is to copy the source of energy that exists in the Sun and stars across the Universe here on Earth. In a fusion process two light atomic nuclei fuse together to create a heavier nucleus. During this process a large portion of energy is released as electromagnetic radiation and fast particles. The basic physics behind fusion has been known for more than 70 years, but despite a lot of research work during last 50 years we still do not have a functional reactor that produces energy using controlled fusion. However, we know that fusion is possible, i.e. we feel joy of fusion every day in form of electromagnetic radiation from the Sun, but the questions are what physical circumstances and which technical aspects do we need to fulfil before we can achieve controlled fusion reactions here on Earth.

A fusion reactor is analogous to an old fashioned oven where coal and woodchips are used as fuel to produce energy. In such an oven, when the temperature is sufficiently high, combustion processes are started, and carbon and hydrogen atoms make chemical bounds to oxygen to produce carbon dioxide, water and heat. A part of the produced energy will
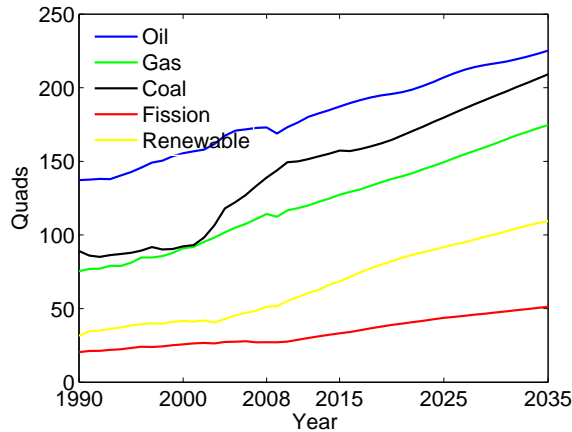
Figure 1.1: Consumption of energy divided into 5 different sources using data from U.S. Energy Information Administration. The unit for large quantity of energy is called "Quad" where 1 Quad $= 1.055 \cdot 10^{18}$ Joules $= 25,200,000$ Tonnes of oil. Renewable energy comes from natural resources such as sunlight, wind, tides, and geothermal heat.

also heat up the surrounding fuel so that the process becomes self-sustained for a longer period of time. In this combustion process only electron clouds of atom nuclei interact with each other, while nuclei itself are unaffected. Therefore, these reactions are relatively easy to sustain, and the ignition temperature is relatively low, i.e. most mixtures ignite at around 1000 ^oC.

In fusion reactors principles from the combustion oven remain the same but the physics is different. The fuel is a mixture of two isotopes of light atomic nuclei, deuterium and tritium. Both gases are heated up in a closed chamber; the gases get ionized and from this point we simply use term plasma to describe the hot mixture of ionized gases. At sufficiently high temperature and density, fusion reactions initiate and a part of the energy produced by fusion will remain in the plasma to self-sustain the ignited fusion reactions, i.e. no external heat sources are needed.

The temperature needed to start the chain of fusion reactions is around 100 million ^oC. High temperatures of that order raise a lot of technical challenges such as finding heat sources that are powerful and are able to couple large amount of their available power to plasma and building a fusion reactor that can contain these extremely hot plasmas. Besides that the fusion plasmas should not be in direct contact with surrounding walls or otherwise the plasma will immediately cool down and all the fusion chain reactions will stop. For the last several decades there have been developed methods for successful heating of the plasma beyond 100 million ^oC, while plasma containment is still a challenge we face and are obliged to solve. The difficulties with plasma containment is widely addressed in the fusion community and will hopefully be solved in the near future. At that time we will have a first prototype of fusion reactor, and we will be very close to a source of sustainable energy. The future generations will have an alternative eco-friendly energy source that is free of production of carbon dioxide and similar greenhouse gases created from the combustion of fossil fuels.

Several large projects on fusion energy have been started around the world such as the "Tokamak Fusion Test Reactor" (TFTR) in US, "Tokamak Experiment for Technology Oriented Research" (TEXTOR) in Germany, "Joint European Torus" (JET) in Culham, Great Britain, "Axially Symmetric Divertor EXperiment" (ASDEX) Upgrade in Germany and the future machine "International Thermonuclear Experimental Reactor" (ITER) in

South France. ITER will be the largest tokamak in the world, a gate to understand fusion plasma containment in detail. So, what do we expect to get in 30-40 years from ITER and the research effort and financial investments in fusion science? We expect to build fusion reactors that will

- give us an inexhaustible amount of energy since the fuels are easily accessible in nature.

- produce eco-friendly energy and save the environment from harmful waste products such as carbon dioxide, dangerous chemicals and radioactive materials.

- be able to produce energy for a compatible price relative to energy production price based on fossil fuels or nuclear fission.

Before we can achieve these goals, political organizations and educational institutions must provide necessary resources to the field of fusion science. Fortunately, the motivation for fusion among scientists is strong and the last decade's progress in fusion research has increased public confidence that fusion is possible here on Earth. During next few sections we will get familiar with basic concepts behind fusion.

1.2   Thermonuclear Fusion

Plasma is often referred to as the fourth state of matter, in which a gas may be fully or partially ionized, i.e. at least one electron is repelled from the electron cloud of the respective atom nucleus. In general terms, we identify as plasma any state of matter that contains enough free charged particles so its dynamics is dominated by electromagnetic forces. We need very small portion of gas to be ionized before the dynamics exhibit electromagnetic properties, for instance 0.1 percent ionization of a gas results in electrical conductivity almost half of the maximum possible.

Plasma dynamics is described by the self-consistent interaction between electromagnetic fields, governed by Maxwell's equations, and spatial resolution of a large amount of charged particles, governed by the Lorentz equation. In other words, given the instantaneous electric and magnetic fields $\mathbf{E}(\mathbf{x}, t)$ and $\mathbf{B}(\mathbf{x}, t)$, the forces on the particle j can be calculated using the Lorentz equation and then iteratively used to update the path $\mathbf{x}_j(t)$ and velocity $\mathbf{v}_j(t)$ of each particle. This procedure is, however, completely impossible to handle for computers of many years to come. The number of particles even in a single Debye sphere, i.e. a sphere with a radius of one Debye length, is just too large. The following three parameters are widely used to characterize a plasma:

1. the particle density n of each particle species measured in particles per cubic meter,

2. the temperature T of each particle species measured in eV,

3. the steady-state magnetic field B measured in Tesla, in the case plasma is confined by surrounding magnetic field.

The most common investigated fusion reactions are applied on light gases such as deuterium and tritium. Following three reactions may be used as a basis for design of fusion plasmas containment chambers

$$
{}^2_1H + {}^2_1H \longrightarrow \begin{cases} {}^3_1H + {}^1_1H & 50\% \\ {}^3_2He + {}^1_0n & 50\% \end{cases} \tag{1.1}
$$

$$
{}^2_1H + {}^3_1H \longrightarrow {}^4_2He + {}^1_0n \quad (17.6\,MeV) \tag{1.2}
$$

$$
{}^2_1H + {}^3_2He \longrightarrow {}^4_2He + {}^1_1p \tag{1.3}
$$
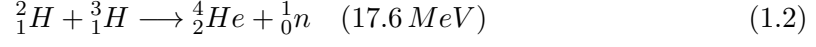
The energy output of deuterium-tritium (D-T) reaction is $\Delta E = 17.6$ MeV from which 3.5 MeV is associated with the alpha particle ${}^4_2He$ and 14.1 MeV is associated with the neutron ${}^1_0n$. Thereby, one fifth of the net energy gained from a D-T reaction is carried by the alpha particle while four fifth is carried by the neutron. The alpha particle is confined by the magnetic field that contains plasma and is used to heat the plasma in the background, i.e. the bulk plasma. The neutron carries no electric charge, and therefore it can pass the magnetic field lines and has to be absorbed by the surrounding wall blankets.

The D-T fuel cycle is, due to the low cross section described in Sec. 1.2.1, easiest and most promising fusion reaction to be used for fusion experiments. Deuterium is found in relatively large scales in the seawater while tritium is unstable and does not occur naturally. Therefore, D-T fuel cycle requires breeding of the tritium from e.g. lithium through one of the following reactions

$$
{}^6_3\text{Li} + {}^1_0n \longrightarrow {}^3_1\text{T} + {}^4_2\text{He}, \tag{1.4}
$$

$$
{}^7_3\text{Li} + {}^1_0n \longrightarrow {}^3_1\text{T} + {}^4_2\text{He} + {}^1_0n \tag{1.5}
$$

Preliminary calculations show that a 1 GW fusion power plant requires an annual D-T fuel consumption of 250 kg. D-T fuel required for continuous burning plasma in a 1 GW fusion power plant is few grams, implying that we have maximum some grams of D-T fuel in the power plant at all times. Therefore, safety is never compromised as it would be the case for a fission power plant.

1.2.1 The Lawson Criterion

In plasma physics it is convenient to use the electronvolt [eV] as a normalized unit of temperature, so that 1 eV is approximately 11600 Kelvin (K) due to the conversion $1 \cdot \frac{q}{k_B} = 11604.5\ K$ where k_B is the Boltzmann constant and q is the electron charge. The fusion energy generated by a D-T reaction is calculated as $P_{fusion} = n_D n_T < \sigma v > \Delta E$, where n_D and n_T are densities of deuterium and tritium, respectively, and $< \sigma v >$ denotes the reaction rate, σ being the collisional cross-section and v the relative velocity of colliding particles. For a D-T plasma with reaction temperature of 10 keV, we find $< \sigma v > \sim 1.1 \cdot 10^{-23}\ [m^3 s^{-1}]$ so that $P_{fusion} \sim 7.7 \cdot 10^{-35} n^2\ [Wm^{-3}]$. About 20% of this output is the kinetic energy associated with alpha particles which is available to sustain the process of fusion in the reactor chamber while the remaining 80% is kinetic energy of the neutrons which escape from the plasma to the surrounding wall blankets. Thus, the energy absorbed by the plasma is $P_\alpha = n_D n_T < \sigma v > E_\alpha$, where $E_\alpha = 3.5$ MeV. P_α is the heating power that is added to the unit volume of plasma per unit time caused by fusion. The reaction rate at temperatures of the order of 10 keV, corresponding to the temperature of 116 million K which are achievable and containable in nowadays plasma experiments, is sufficient for fusion to occur. If we assume $n_D = n_T = n_e/2$, where n_e is the electron density, the fusion power density becomes

$$
P_{fusion} = \frac{1}{4} n_e^2 < \sigma v > E_{fusion}. \tag{1.6}
$$

The fusion gain factor Q is analogous to the quality factor of an electric circuit, i.e. a ratio of internal and external sources

$$Q = \frac{P_{fusion}}{P_{aux}}, \tag{1.7}$$

where P_{aux} is, in many cases, a sum of several independent auxiliary heating sources. For the case $Q = 1$ is called break-even and $Q = \infty$ ignition. For the case the break-even point is surpassed, i.e. $Q > 1$, we call this condition for burning plasma. In 1997 researchers at JET reached fusion gain factor of $Q = 0.64$. Preliminary calculations show that the gain factor $Q > 5$ implies that the fusion power delivered to the absorbing blankets is greater than the external heating power. ITER, the new but not yet built device based on magnetic confinement, has the goal to reach $Q = 10$. Achieving a gain factor above $Q = 20$ is considered as good as ignition. This number will most probably not be reached in ITER, and we may have to go for another version of a fusion power plant in order to reach ignition.

The energy loss from the plasma is calculated using the energy confinement time τ_E and the energy stored in the plasma $3n_eT$

$$P_{loss} = \frac{3n_eT}{\tau_E} \tag{1.8}$$

The power generated by the fusion reactions and the power delivered to heat the plasma is calculated as

$$P_{in} = P_{fusion} + P_{aux} = P_{fusion} + \frac{P_{fusion}}{P_{aux}}, \tag{1.9}$$

$$= P_{fusion} \left(1 + \frac{1}{Q}\right). \tag{1.10}$$

Now, we can derive the Lawson criterion through the statement that the input power should be (at least) as large as the power loss. Thus we have

$$P_{in} \geq P_{loss} \Rightarrow \tag{1.11}$$

$$\left(1 + \frac{1}{Q}\right) \frac{n_e^2}{4} < \sigma v > E_{fusion} \geq \frac{3n_eT}{\tau_E} \Rightarrow \tag{1.12}$$

$$n_e T \tau_E \geq \frac{Q}{Q+1} \frac{12}{E_{fusion}} \frac{T^2}{< \sigma v >}. \tag{1.13}$$

When the Lawson criterion is written as in Eq. (1.13) it is called "the triple" product since it uses density, temperature, and confinement time to determine the figure of merit for a plasma, a state where ignition is reached. Put differently, we need to find a scenario in this four-dimensional space (3 independent parameters and the product) so heating of the plasma by means of fusion is sufficient to maintain the temperature of the plasma against all losses without use of external sources. In the case that we have ignition, i.e. $Q = \infty$, then for a D-T reaction we get from Lawson criterion $n_e T \tau_E > 10^{20} \; keV s/m^{-3}$.

1.3   The Tokamak

The fusion energy we intent to produce here on Earth seems to have best burning conditions in a chamber called tokamak. The tokamak is a toroidal device, shaped as a
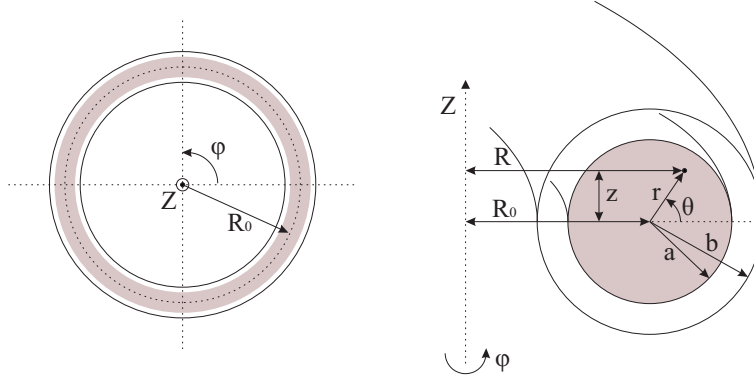
Figure 1.2: Tokamak geometry with plasma in the light red color. The left figure shows toroidal (horizontal) cut through the tokamak center plane while the right figure is a poloidal (vertical) cut at an arbitrary position.

doughnut, which confines the plasma by means of a toroidal magnetic field created by a number of coils and a poloidal magnetic field created by the toroidal plasma current. The plasma current is primarily created by a transformer action induced by using the plasma as the secondary winding around the transformer core. The pulse limitation in this approach has triggered research to investigate the possibility for driving current non-inductively, i.e. current drive without transformer action. A unique demonstration of fully non-inductive current drive was given in the Tore Supra tokamak in a nearly 6 minute steady state plasma discharge [34]. The standard pulse length of present day tokamaks is on the order of 0.1 - 30 seconds.

In Fig. 1.3 the magnetic field configuration for TEXTOR is shown. The TEXTOR tokamak has circular poloidal cross-section, while the ASDEX Upgrade tokamak, which we will consider in this work, has D-shaped poloidal cross-section. The geometry used to quantitatively describe radiation and particle motion in a tokamak is the cylindrical coordinate system with addition of the spherical angel θ. The tokamak geometry is depicted by Fig. 1.2 where b and R_0 are the minor and major radius of the toroidal vessel, respectively. For a given toroidal angle ϕ the (R, z)-plane defines the poloidal plane. The circular plasma column depicted by Fig. 1.2 is colored in light red and has a radius $a < b$. The tokamak geometry defined by (R, z)-plane and (θ, ϕ) angles is a widely used concept among scientists working with plasma diagnostic systems. These are the geometry parameters we use to determine the location of the scattering volumes discussed in chapter 2.

The magnetic field lines in a tokamak are nested in surfaces called flux surfaces. In the plasma center these flux surfaces collapse to a point called the magnetic axis. To first approximation, the current flows within these flux surfaces and the pressure on each flux surface is constant. The TEXTOR equilibrium has a toroidal magnetic field on axis ($R_0 = 1.75$ m) of 2.6 T and a plasma current of 400 kA [56]. The ASDEX Upgrade experiment operates with plasma radius of 1.65 m and plasma volume of 13 m^3, the maximum magnetic field is 3.1 T, a maximum plasma current of 1.6 MA and maximum heating power goes up to 27 MW [89].

Ideally, the tokamak is symmetric about the z-axis. Hence, to first approximation, the magnetic field lines and the plasma parameters are identical for all poloidal cross sections. In the Fig. 1.3, the flux surfaces are cut open and a poloidal cross section with magnetic field vectors is shown.

The safety factor, q, is defined as the number of toroidal turns divided by the number
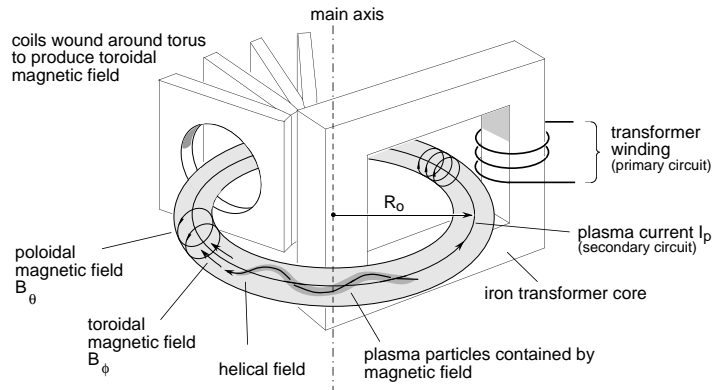
Figure 1.3: A universal image of a tokamak device. B_θ is the poloidal magnetic field produced
due to plasma current I_p while B_ϕ is the toroidal magnetic field produced due to coils
wound around torus. The resulting magnetic field will have a helical form increasing
plasma confinement of the charged particles.

of poloidal turns of a magnetic field line until it closes upon itself in the poloidal projection.
In the Fig. 1.3 a magnetic field line at the plasma edge, represented by a red curve, is
traced once around the torus. The q value at the edge of this magnetic configuration
is 3.8, which means that after 3.8 turns the magnetic field line will end up at the same
location in the poloidal projection. The q-profile are very useful when considering plasma
confinement in tokamaks. In standard tokamak operation, with a current density peaking
in the plasma centre, the safety factor, q, is slightly lower than 1 in the plasma centre
and increases monotonically towards the plasma edge.

1.4   ITER

ITER is going to be the largest and most promising next generation of magnetically
confined fusion devices, see Fig. 1.4. ITER is placed in Cadarache, South France and
is a joint project between seven international partners: China, European Union, India,
Japan, Korea, Russia and USA. The goal of ITER is a large-scale scientific experiment
that aims to prove that energy from fusion is possible to commercialize.

The fusion gain factor of ITER is $Q = 10$ and represents the scientific goal of delivering
ten times the power it consumes. With expected 50 MW of input power, the ITER
machine is designed to produce 500 MW of fusion power, an objective that has not
been achieved before. Besides the high gain factor, ITER will test a number of key
technologies necessary for the next step in the quest for fusion energy: a DEMO version,
the demonstration fusion power plant with higher gain factor than ITER and cheaper and
more adaptable construction suitable for commercial use.

Besides the work on the components necessary for ITER to operate, there will also
be a large number of diagnostic systems associated to the characterization of the plasma
behavior. Some of these systems are based on mm-wave technology due to the frequency of
the electron cyclotron emission. Such a diagnostic is collective Thomson scattering (CTS)
that uses a probing beam from a gyrotron and picks up the scattered light associated to
the dynamics of fast ions. The ITER organization has recently decided that CTS is
enabled and considered as a highly relevant diagnostic to be installed [29]. Many parts of
this thesis are dedicated to the technology used in CTS and other similar fusion plasma
diagnostics. Suggestions for CTS at ITER are given in conceptual studies [52] with
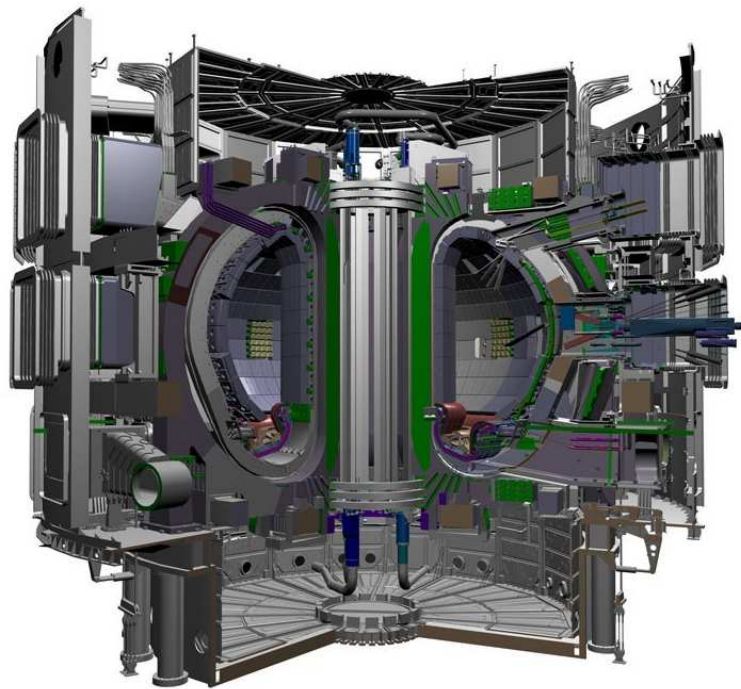
Figure 1.4: ITER is based on the tokamak concept with the plasma contained in a torus-shaped vacuum vessel. The fuel in ITER will be deuterium and tritium, the so called D-T reaction, with temperatures in excess of 150 million K. In contrast to most of the already existing tokamaks superconducting coils surrounding the vacuum vessel will be installed in ITER to keep the plasma away from the walls. The entire vacuum vessel is enclosed within a cryostat, which is shown in the top, the bottom, and the sides of this figure. The cryostat is a large cold box and provides thermal isolation for the superconducting coils and many other components. The figure is reproduced with permission, *iter.org*.

scattering geometry described in Sec. 2.4.

Chapter 2

Collective Thomson Scattering

2.1 Short background and introduction

The conditions for operating a diagnostic for fusion plasmas are, due to strongly radiative environment, relatively complicated and require careful attention to the hardware. Due to the harsh environment of the plasmas all contact diagnostics fail to survive in such difficult and hostile conditions. Otherwise temperature, density and even the distribution function of the charged particles could be measured by probes. Necessity of using electromagnetic radiation to characterize dynamics of charged particles, taking into account the technologies available for diagnostics, is inevitable. The electromagnetic radiation due to scattering off electrons is an important diagnostic in fusion as in other fields of physics dealing with charged particles. This chapter is intended as an introduction to the principle of CTS with a short description of the CTS diagnostic.

When charged particles are affected by an electric field they get accelerated and as a consequence radiation is emitted. Assuming that the charged particle is accelerated to some velocity $\Delta v \ll c$, then according to Larmor's equation [10] the radiated power scales as the acceleration squared multiplied by charge square. During scattering experiments in plasmas, the radiation from the probing beam accelerates both the ions and the electrons. Since the ions are much heavier than the electrons, and the magnitude of the acceleration is inversely proportional to the mass, the radiation emitted from the ions can be neglected. Thomson scattering is electromagnetic scattering off electrons not bound by atomic states. Due to the Doppler shift, scattered radiation off uncorrelated electrons contains information on electron dynamics such as thermal motion and hence the electron temperature. At higher densities the electron correlations are not negligible. Here, we assume an incident wave which scatters off fluctuations in the electron distribution. In plasmas, the electric field produced by a given test particle is screened by the electromagnetic fields emitted by the electrons. The length scale of this screening is usually described by a sphere with a radius λ_D called Debye length

$$\lambda_D = \sqrt{\frac{\epsilon_0 T_e}{n_e q_e^2}}, \tag{2.1}$$

where subscript T_e is electron temperature, n_e is electron density, and q_e is elementary charge. In a tokamak the Debye length is typically few millimeters, while in the Solar core the Debye length is in the nanometer range due to very high densities. In the case where the resolved fluctuation scale length is much smaller than the Debye length, the assumption on uncorrelated electrons is sufficient to describe the scattering process.
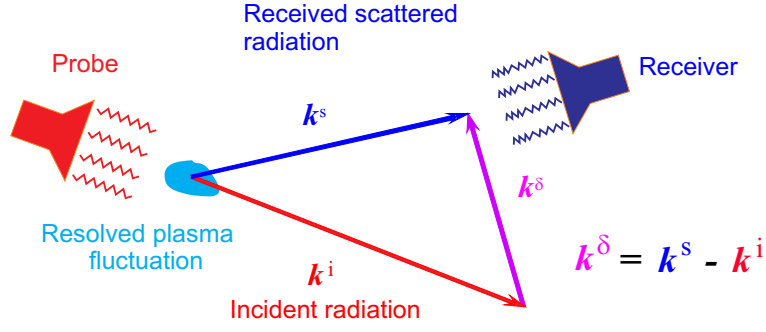
Figure 2.1: Collective Thomson scattering principle where the received spectrum carries information of the ion velocity distribution component along k^δ.

In the case where the resolved fluctuation scale length is larger than the Debye length, collective fluctuations are resolved. Ions in a plasma, particularly those with significant energies, affect fluctuations in the electron density and thereby the collective behavior of the electrons. By choosing the correct probing frequency and suitable scattering geometry, fluctuations induced by the ion motion may be resolved.

The principal geometry of Thomson scattering is best described as a three wave mixing process. The incoming wave, which is a probing beam described by a wave vector and an angular frequency $(\mathbf{k}^i, \omega^i)$, interacts with a plasma wave $(\mathbf{k}^\delta, \omega^\delta)$, and the two waves are summed to a scattered wave defined by:

$$(\mathbf{k}^s, \omega^s) = (\mathbf{k}^i + \mathbf{k}^\delta, \omega^i + \omega^\delta) \tag{2.2}$$

Salpeter [72] introduced a parameter defined as $\alpha = 1/|\mathbf{k}^\delta|\lambda_D$, and which was later named Salpeter parameter, that is used to describe limits between incoherent Thomson scattering (or simply Thomson scattering) and CTS:

$$\alpha \ll 1 \quad \Rightarrow \quad \text{incoherent Thomson scattering,} \tag{2.3}$$
$$\alpha > 1 \quad \Rightarrow \quad \text{collective Thomson scattering.} \tag{2.4}$$

The main difference between the two scattering techniques is the choice of probing frequency. For applications in tokamak plasmas, the incoherent scattering is achieved by using visible or near infrared laser light, while the conditions for CTS are usually satisfied when using far infrared or mm-waves. When the incident beam is around 100 GHz, we have that $k^\delta \approx k^i \approx 2000 \ [m^{-1}]$, then for a typical tokamak plasma no restrictions are present on the scattering geometry in order to have Eq. 2.4 fulfilled. In this work, we will only consider CTS. Figure 2.1 shows an example on CTS scattering geometry.

Fluctuations in the electron distribution are induced by the ion motion. Collective Thomson scattering is based on electromagnetic radiation scattering off ion driven collective fluctuations in a plasma. The principle behind such fluctuations can be depicted as a swan on a lake leaving a depression in the water and drawing a wake as it moves forward. The swan represents the fast ion and the water represents the electron distribution. The depression, created by the swan (fast ion) is associated to the Debye shielding surrounding the ion while the wake is associated to the weakly damped waves stimulated by the interaction with the ion motion. The scattered radiation induced by a probing beam can provide a range of information about the plasma, such as temperatures and relative densities of fuel ion species or impurities. All this information is contained in the power spectrum of the scattered radiation.

2.2   Example of a CTS spectrum

The evolution of the CTS spectrum of TEXTOR discharge 89509 is shown in Fig. 2.2 [56]. The CTS data is presented as a contour plot, where the spectral power density measured in eV is against time [s] and frequency [GHz]. The signal shown in Fig. 2.2 is strongly anisotropic due to an anisotropic source of fast ions in the TEXTOR tokamak (co-I_p neutral beam injection) and the scattering geometry. The signal from the fast ions was expected to be at frequencies higher than the gyrotron frequency due to the experimental geometry. Due to limited memory in ADCs different spectral resolution is used for the signals below the gyrotron line and the signals above the gyrotron line. An effect of switching the neutral beam injector off at $t = 2.2\ s$ is clearly pronounced. The probing frequency of the CTS experiments at TEXTOR is approximately 110 GHz and no data is collected in that frequency range because of the notch filters which protect the receiver components from stray radiation. Taking plasma parameters and scattering geometry into account, the 1-D projection of the fast ion velocity distribution function can be inferred from the measured spectrum [5, 8]. The CTS diagnostic can also be used for ion temperature measurements, measurements of the plasma isotope composition, and investigating instabilities. Frequency shift in the scattered light due to fast ions can be estimated as $\Delta v \approx \mathbf{k}^{\delta} \cdot \mathbf{v}$. For nearly backscattering geometry of the experiments, using neutral beam injectors with the maximum injection energy in the order of tens of keV, the frequency shift of the scattering radiation is expected to be in the order of 1 GHz. Total bandwidths of the TEXTOR and ASDEX Upgrade CTS receivers are 6 GHz and 10 GHz, respectively. In Fig. 2.2 we see that the spectral power density plotted after the electron cyclotron emission background subtraction. The fundamental properties behind the electron cyclotron emission are introduced in Sec. 2.4. The typical expected rate of change in CTS data due to detection of fast-ion signals is in the range 1 - 2 eV.

2.3   Why measure fast ions?

Populations of fast ions are a source of free energy which we can not afford to waste, otherwise the Lawson criterion will not be satisfied and thus no fusion will occur. In ITER [35], which is the next step tokamak, around 70% of the heating is expected to come from fast alpha particles produced in the D-T fusion reactions. This source of free energy is orders of magnitude larger than that of the energy of the thermal ions. In ITER we expect the fast ion density will only constitute around 0.8% of the plasma density in the center, but at the same time the fast ions will carry approximately 15% of the kinetic energy available in the center of the plasma [35]. These fast particles are expected to continuously slow down and deliver their energy to the bulk plasma, primarily to the electrons, through collisions.

Also fast ions generated by auxiliary heating will exist in ITER, as they are found in the most tokamaks. In ITER, energetic populations of tritium will be generated by ion cyclotron resonance heating with relatively high energies compared to the birth energy of the fusion born alpha particles. Beams of energetic neutral deuterium will also be injected with an energy of 1 MeV per atom. This may drive instabilities and plasma modes which in some cases may react back on the fast ions and expel them from the plasma which, however, may reduce the plasma heating. The driven modes may furthermore degrade the general plasma confinement, and energetic ions ejected from the plasma is a concern regarding heat loads on the first wall. The dynamics of these energetic particles is one of the important physics parameters in the ITER design, especially the interaction with
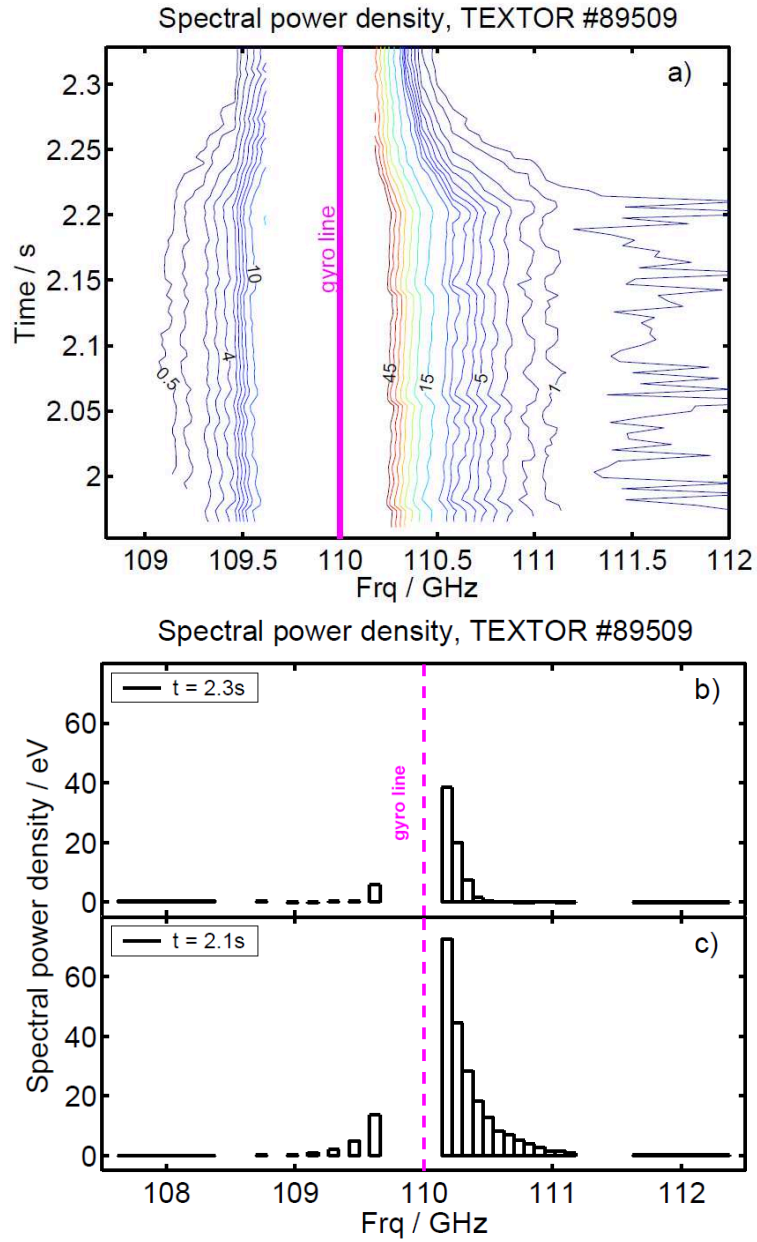
Figure 2.2: A typical contour plot of CTS spectral power density reprinted with permission [56]. In (a) the ion heating is turned off at $t = 2.2\ s$ consequently decreasing the width of the CTS spectrum. The CTS spectrum at $t = 2.3\ s$ (heating off) is shown in (b) while that at $t = 2.1\ s$ (during heating flattop) is shown in (c).
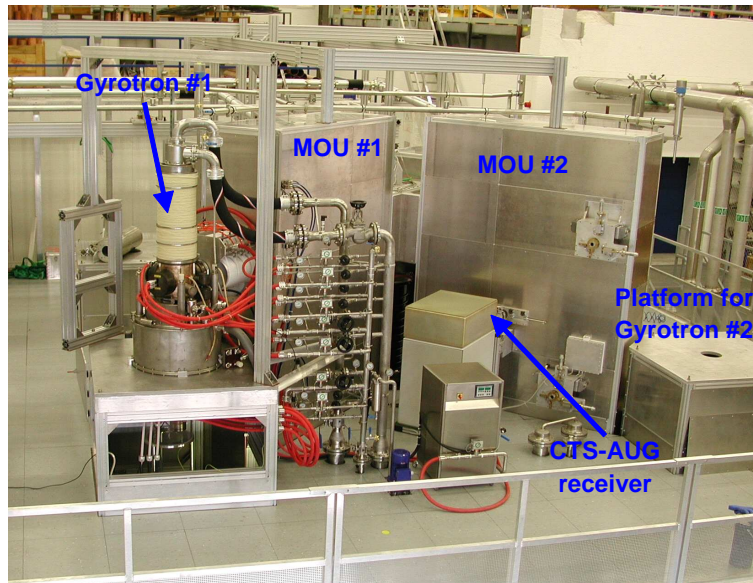
Figure 2.3: Overview of the gyrotron hall at ASDEX Upgrade.

instabilities, in order to avoid scenarios where fast ions are lost. Further development and successful experimental measurements, through reliable diagnostics such as CTS, of fast ions resolved in time, space and velocity are needed.

2.4   CTS systems today and in future

At ASDEX Upgrade, Garching, Germany, a fully equipped CTS system is in operation. The front-end electronic part of the receiver is placed inside the gyrotron hall due to flexible access of the receiving beam. The gyrotron hall together with the CTS receiver is shown in Fig. 2.3 where we also see matching optics unit (MOU) boxes relatively close to the receiver. The MOU is a large, enclosed aluminium box that contains quasi-optic components for beam shaping, polarization selection, and calorimetric measurements. Figure 2.4 shows the inside an MOU box in two operating modes; gyrotron mode and the CTS mode which is governed by a movable mirrors that intercepts the incoming signal into the CTS receiver, as shown in Fig. 2.4(b).

The maximum signal will occur at particular mirror angles according to the ray tracing calculations under assumption that the alignment of the polarizers and mirrors is performed correctly. This is shown in Fig. 2.5.

CTS can provide spatially and temporally resolved measurements of the one-dimensional (1-D) fast-ion velocity distribution along the direction of k^δ vector which is determined by the scattering geometry. The components of the k^δ vector are defined with respect to the direction of the magnetic field **B**, and thus the fast-ion distribution may be measured as a function of velocity parallel or perpendicular to **B**. For fusion plasmas, measured distributions are a sum of alpha and other fast ions distributions where each population is weighted by the square of the species charge. CTS technique has successfully provided spatially and temporally resolved measurements of the one-dimensional fast ion velocity distribution on JET [6]. Also a range of successful fast ion measurements has been demonstrated in TEXTOR [56, 8, 57, 58, 59]. Promising and still on-going work on fast ion data at ASDEX Upgrade has been demonstrated [53, 54, 42].

The CTS hardware consists of a transmitting and receiving part. In microwave based

(a)   (b)
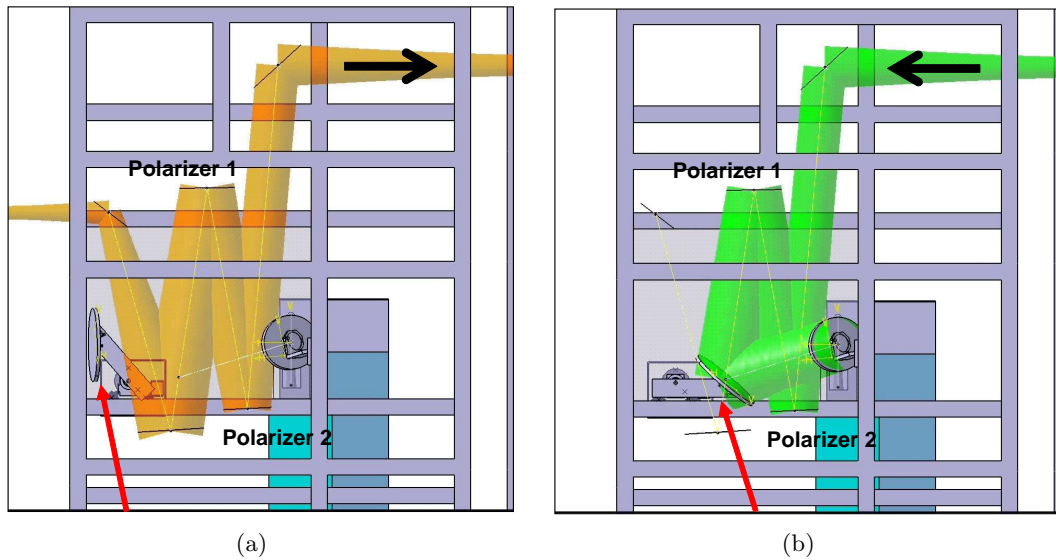
Figure 2.4: CTS transmission line coupled to ECRH #2 transmission line: (a) ECRH opera-
tion with red arrow showing the interception mirror in the neutral position. The
gyrotron beam is launched from the left; (b) Collecting the scattering signal plus
the background radiation with the interception mirror in the CTS operation mode.
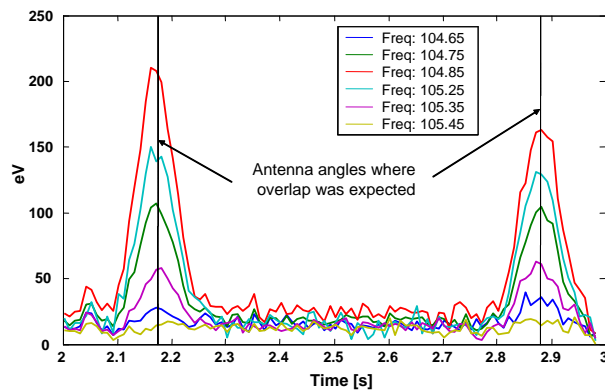
Figure 2.5: Time traces (shot #22328) of the scattered radiation for the centermost channels
during a double poloidal scan of the receiver beam across the probe beam. The two
vertical lines are the time points where the receiver antenna position is expected to
have maximum overlap from calculations based on prior in-vessel alignment of the
antenna and ray tracing [53].

CTS systems, the transmitting part resembles that used for ECRH with a powerful microwave source called gyrotron. Gyrotrons are primarily used to heat plasma but we also use it as a probing source. A gyrotron generates an electromagnetic beam of mm-wave which is guided toward the plasma through a transmission line, formed as an overmoded circular waveguide and a number of reflectors and polarizers. The transmission line from the plasma to the receiver is similar but is passed through in reverse direction. The probe beam and the receiver intersect in the plasma in the so-called scattering volume whose size is 10 to 15 cm. The location of the scattering volume is controlled by the quasi-optical antenna mirrors. Typically we place the scattering volume in the plasma center, but also off-axis scattering volumes have been used. The scattering spectrum carries information on the distribution of ion velocity components projected along the fluctuation wave vector $\mathbf{k}^\delta$.

In a magnetically confined plasma, the electrons gyrate around the magnetic field lines with frequencies that depend on three quantities: charge and mass of the particle and magnetic field strength. Due to this centripetal acceleration electrons emit electromagnetic radiation at the gyrotron frequency

$$\omega_{ce} = \frac{eB}{m_e}, \qquad (2.5)$$

and its harmonics $n\omega_{ce}$ where $n = \{1, 2, \ldots\}$, e/m_e is the charge-to-mass ratio and B the magnetic field strength. The radiation emitted by the gyrating electrons is called electron cyclotron emission (ECE and is the most dominant contribution to the spectral power density picked up by the CTS receiver. In order to minimize the ECE signal that reduces the dynamic range of the receiver and to minimize absorption of the probe by the resonance layer, the scenario is chosen such that the resonance layers are located outside the plasma. B is usually in the range $2-3\,T$ or sometimes even higher. Other plasma parameters such as temperature or density play no role at this cyclotron frequency, assuming the temperature does not reach levels where Doppler- and relativistic effects start to occur. Therefore, if an electromagnetic wave with cyclotron resonant frequency is launched into the plasma, all the targeted particles (defined by mass and charge) are heated, provided that the magnetic field complements the resonant condition. In tokamaks, the magnetic field decreases as a function of the tokamak major axis. This allocates the resonant region to a narrow vertical layer in the poloidal geometry. Also, the plasma ions are at least three orders of magnitude heavier than the electrons implying that the ions are much less exposed to the acceleration from the fields in the probing beam compared to the electrons. Therefore, the ions do not contribute to the power spectrum of scattered radiation in the mm-wavelength range as much as the electrons, i.e. the scattering cross section of the ions is smaller than that of the electrons. Scattering due to plasma ions is therefore neglected.

In the Fig. 2.6 we show scenarios for electron cyclotron resonance layers for CTS operation in 3 tokamaks. For instance, a comprehensive study has shown that CTS operation in ITER is well supported by choosing the probing frequency below the fundamental electron resonance frequency in order to minimize the ECE background levels in the expected high levels of the electron temperature T_e and density n_e [52]. CTS at TEXTOR and ASDEX Upgrade operate with probing frequency between the fundamental and the first harmonic [53].

In the Figs. 2.7(a) and (b) we see two examples on raw CTS data detected by the CTS receiver at TEXTOR. The probing beam (gyrotron) is modulated 2 ms on/off in order to subtract the ECE signal where the residual signal is the scattered CTS signal we aim to measure. In Fig. (a) the CTS receiver measures a relatively large amount of
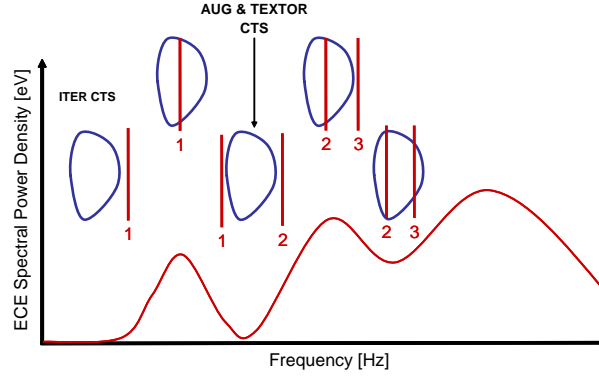
Figure 2.6: Resonance layers for CTS scenarios in different tokamaks as function of the probing frequency. For experiments at ASDEX Upgrade and TEXTOR the fundamental resonance layer (number 1) is located on the high field side outside the plasma while the second harmonic resonance layer (number 2) is located on the low field side outside the plasma, as well. ITER CTS will operate below the fundamental resonance layer, which is located on the low field side outside the plasma. Assuming the **B** field is linearly changing, the resonance layers are located equidistantly from each other according to the Eq. (2.5). However, in a tokamak, the **B** field is proportional to $1/R$, so the distance between the fundamental and the second harmonic is not comparable to the distance between the second- and the third harmonic.

scattered signal approximately 1.5 GHz below the probing frequency, while in Fig. (b) the CTS receiver does not pick up any scattered signal at approximately 2 GHz above the probing frequency. The data in both graphs is taken for the same plasma discharge.

CTS has already successfully provided spatially and temporally resolved measurements of the fast ion velocity distribution in one dimension on JET [6] and TEXTOR [56, 57, 58]. CTS has recently been enabled by the ITER Organization (IO) and therefore the Danish group carried out a feasibility study on CTS design for ITER at the 60 GHz range [52]. The feasibility study was concluded with a proposal for two separate systems. Each system is equipped with its own radio frequency (RF) probing beam and separate set of quasi-optical detectors. The first system, shown in Fig. 2.8, measures with $\mathbf{k}^\delta$ perpendicular to the **B** field vector. It consists of a radially directed RF probing beam and the receiver, both located in the equatorial port at the low field side of the vacuum vessel. This system is often referred as a low field side backscattered (LFS-BS) system, due to the position of the receiver and the fact that we measure a backscattering signal, a direction nearly opposite of the RF probing beam. The second system, shown in Fig. 2.9, measures with $\mathbf{k}^\delta$ parallel to the **B** field vector. It consists of the same RF probing beam as in the LFS-BS system whereas the receiver is mounted in the inner vacuum vessel wall and views the plasma through a slit between two blanket modules [46]. This system is referred as a high field side forward-scattered (HFS-FS) system, due to the position of the receiver where **B** field is high and the fact that we measure a forward-scattered signal, forward since this is also similar direction of the RF probing beam.

2.5   The gyrotron

Throughout this chapter we have several times mentioned that gyrotrons [28] are used as the probing radiation source for CTS experiments at TEXTOR and ASDEX Upgrade. At TEXTOR we have used a 110 GHz gyrotron capable of delivering up to 300 kW

(a)   (b)
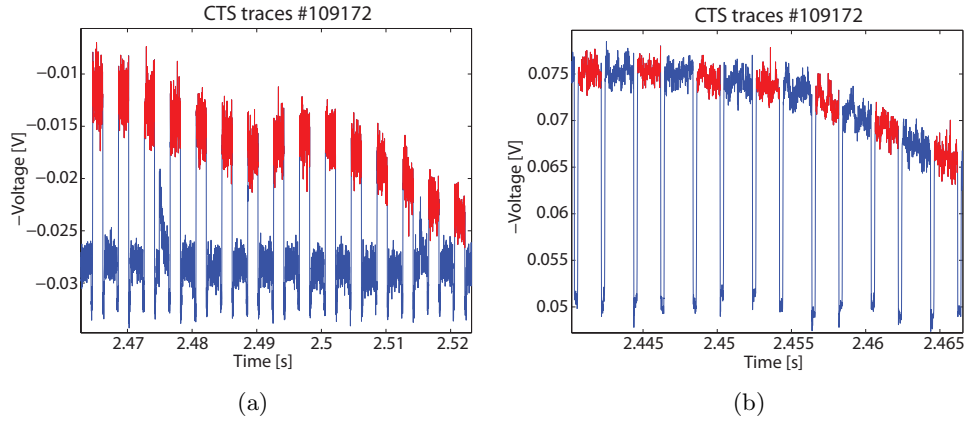
Figure 2.7: TEXTOR CTS receiver with gyrotron on-period colored in red and gyrotron-off period colored in blue: (a) Channel 9 with a high CTS signal; (b) Channel 42 with no CTS signal.

(a)   (b)
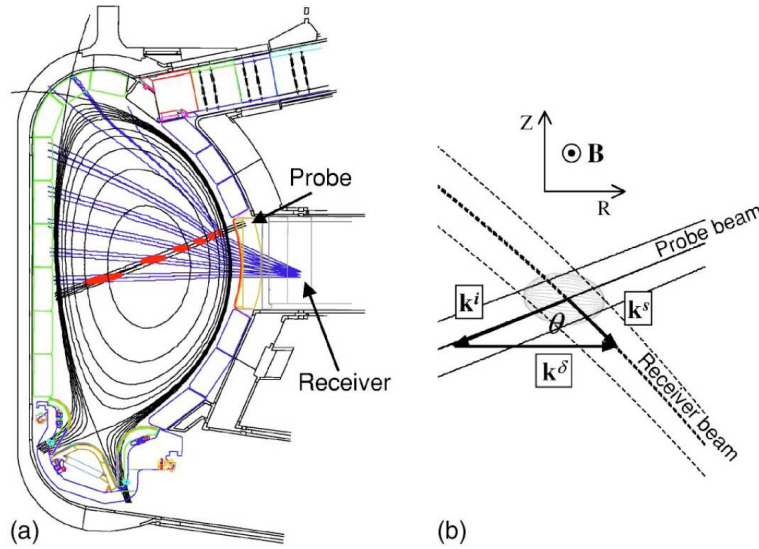
Figure 2.8: ITER vacuum vessel poloidal cut with the LFS-BS setup: (a) beam traces of the LFS-BS system and (b) a closeup view of the probe beam and one of the receiver beams where the scattering volume is colored in grey. The drawing shows the wave vectors of the received scattered radiation $\mathbf{k}^s$, probe radiation $\mathbf{k}^i$, and the fluctuation wave vector $\mathbf{k}^\delta$ (see Fig. 2.1) which is almost perpendicular to $\mathbf{B}$. The figure is reproduced with permission [52].
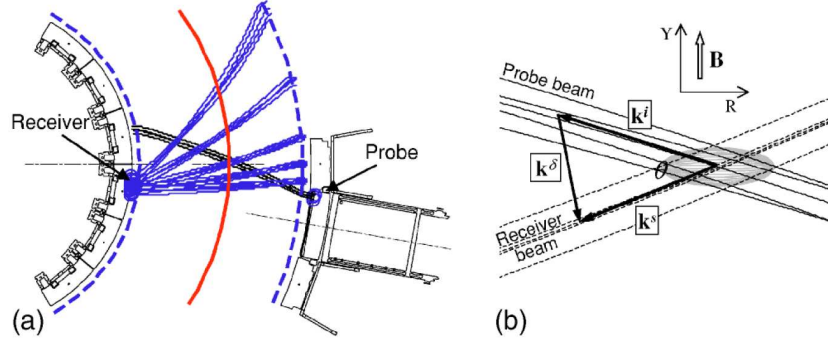
Figure 2.9: ITER vacuum vessel toroidal cut with the HFS-FS setup:(a) Top view of beam traces for the HFS-FS with a the LFS probing beam and HFS-FS detector. (b) Closeup view of the probe beam and one of the receiver beams with the scattering volume colored in grey. Furthermore, we see the wave vectors of the received scattered radiation $\mathbf{k}^s$, the incident probe radiation $\mathbf{k}^i$, and the fluctuation vector $\mathbf{k}^\delta$ which is almost parallel to $\mathbf{B}$. The figure is reproduced with permission [52].

for continuous on-time of 200 ms. Measurements performed in 2006 [94] demonstrated 180 kW forward power with start frequency at 109.970 ± 0.005 GHz and a thermal drift up to 27 MHz downshift depending on the duty factor. For the most relevant scenario in CTS experiments, a duty factor of 50% is used with 2 ms on and 2 ms off for 400 ms, a chirping of 23 MHz downshift was observed. The gyrotron has been constructed and tested by Gycom, Russia [90, 19], while the daily operation was responsibility of a team working at FOM Institute for Plasma Physics, Netherlands. The gyrotron activities at TEXTOR are today terminated due to resource reallocation within FOM. At ASDEX Upgrade, the gyrotron called Odissey-1 was characterized [94]. Odissey-1 was able to deliver 500 kW forward power with the frequency start at 104.786 GHz and chirped down 104 MHz, with 90% of the chirp occurring in the first 100 ms, as shown in Fig. 2.10. At lower output power the frequency downshift also occur but with lower values.

Generally, gyrotrons consist of a beam of weakly relativistic electrons injected into a cavity tube which is embedded in a static magnetic field. The emitted radiation caused by the gyro-motion of the electrons couples to a resonance cavity mode which is converted into a Gaussian beam using phase correcting mirrors. The high power in the 110 GHz TEXTOR gyrotron is obtained by using a large cavity and high mode number, namely $TE_{15,43}$. It couples up to 35% of the electron power to the cavity mode which is then converted into a Gaussian beam with an efficiency of 95%. After passing through the cavity, the electrons are dumped in the collector area. Odissey-1, the gyrotron used at ASDEX Upgrade, is a dual-mode gyrotron meaning it can operate at several frequencies, which broadens experimental possibilities with respect to the magnetic field. Odissey-1 had demonstrated an output power of 630 kW for 10 seconds and 950 kW for 10 seconds at 105 GHz and 140 GHz, respectively [47, 87]. The modes used by Odissey-1 are $TE_{17,6}$ for 105 GHz and $TE_{22,8}$ for 140 GHz. Details of gyrotron principles and development are described in [60, 82].
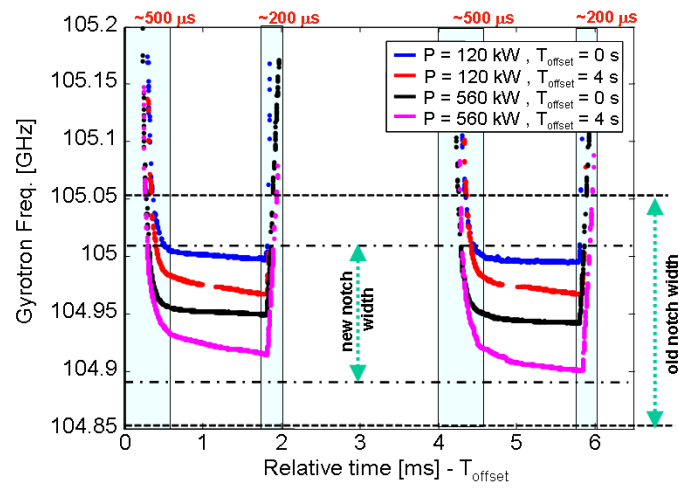
Figure 2.10: Time evolution of a gyrotron installed at AUG for two output powers at time=0 and 4 s of the pulse. Two pulses are shown during an on/off modulation operation with 2 ms on time at 50% duty cycle. The set of horizontal dashed lines and dash-dot lines show rejection bandwidths of the old and new notch filters, respectively [53].

Chapter 3

Millimeter wave Quasi-Optics for ITER

3.1   Short background and introduction

A considerable amount of work in CTS group is dedicated to design of quasi-optical components. Due to the convenient integration possibilities and increased flexibility, the path where CTS signal is backscattered to the electronic part of the receiver is physically the same as the path used for ECRH (RF heating) of the plasma. In other words, the existing ECRH sources set up a standard how quasi-optics should be designed for CTS experiments. Therefore, quasi-optics such as reflectors, polarizers, and waveguide transmissions are similar in size and shape for both CTS and ECRH. This chapter is intended to give an impression how quasi-optical reflectors for millimeter-wave diagnostics, installed at fusion devices, are constructed and tested.

The quasi optics is the first part of the front-end hardware electromagnetic radiation, coming from a plasma, encounters on its way to the receiver. Therefore any losses due to standing waves or radiation leakage will directly add to the noise figure of the receiver. Careful investigation of all quasi-optical parts is needed and here we present design of mirrors used in a proposal for CTS at the next generation tokamak, ITER [52].

The physics on fast ions will play an important role for the ITER, where confined alpha particles will affect and be affected by plasma dynamics and thereby have impacts on the overall confinement. A fast ion CTS diagnostic using gyrotrons operated at 60 GHz will meet the requirements for spatially and temporally resolved measurements of the velocity distributions of confined fast alphas in ITER by evaluating the scattered radiation [52]. While a receiver antenna on the low field side of the tokamak, resolving near perpendicular (to the magnetic field) velocity components, has been enabled, an additional antenna on the high field side (HFS) would enable measurements of near parallel (to the magnetic field) velocity components. The author of this thesis has been involved in the design and measurements of a compact solution for the proposed mirror system on the HFS and the results are presented in [46]. The HFS CTS antenna is located behind the blankets and views the plasma through the gap between two blanket modules. The viewing gap has been modified to dimensions 30×500 mm to optimize the CTS signal. A 1:1 mock-up of the HFS mirror system was built demonstrating that the measurements of the beam characteristics for mm-waves at 60 GHz used in the mock-up agree well with the modeling.

In Chapter 2 we have learned that CTS can provide information using one-dimensional scattering geometry, but since fast ion distribution may be highly anisotropic the velocity distribution should optimally be resolved in at least two directions. Choosing geometries

as perpendicular and parallel to the magnetic field seem to be a good option. The spatial location of the measuring volume and the spatial resolution are given by the intersection of the probe beam and the receiver beam collecting the scattered signal. Here we discuss the CTS system for the international thermonuclear experimental reactor (ITER) which is designed to meet ITER diagnostics requirements [7, 52, 62]. The CTS system on ITER is composed of two subsystems: the near perpendicular velocity components of the fast ions with respect to the magnetic field can best be resolved with a receiver antenna on the low field side (LFS), whereas a receiver antenna on the HFS will be best for resolution of the near parallel velocity components. It has been shown that the CTS signal to be measured in a burning ITER plasma will be dominated by alpha particles whereas contributions from neutral beam injection (NBI) and ion cyclotron resonance heating (ICRH) will be relatively small [67, 68, 21]. Space for the CTS subsystem with the antenna on the LFS has been reserved, but the other subsystem with the antenna on the HFS is not part of the ITER baseline design [13]. In Sec. 3.3, we briefly describe the CTS system at ITER. Section 3.4 is focussed on the HFS antenna. In Sec. 3.5, measurements and simulations of beam propagation through a 1:1 mock-up of the envisaged HFS ITER CTS system are presented and discussion of the results are drawn in Sec. 3.6.

3.2   The Gaussian beam

Let us consider radiation with a vacuum wavelength of λ_0 in free space propagating in uniform lossless media with the refractive index of n. Such a media is, in electromagnetic contents, called simple media. The wavelength in this medium becomes $\lambda = \lambda_0/n$. The beam propagates along the z-axis, and has suppressed time dependence of $\exp(i\omega t)$. We also assume that the radiation is not too far from a plane wave, which means that z-dependence is contained primarily in the form of $\exp(ikz)$ where $k = 2\pi/\lambda$ is called the wavenumber. For the system symmetric about the axis of propagation, the solutions to the Helmholtz' wave equation are a set of Gaussian beam modes. The lowest order, known as fundamental Gaussian mode, has the electric field distribution described as [66]

$$E(r,z) = E_0 \frac{w_0}{w(z)} \exp\left[\frac{-r^2}{w^2(z)}\right] \exp(-ikz) \exp\left[\frac{i\pi r^2}{\lambda R(z)}\right] \exp\left[i\arctan\frac{\lambda z}{\pi w_0^2}\right] \tag{3.1}$$

where r is the radial distance from the center axis of the beam $r = \sqrt{x^2 + y^2}$, and $E_0 = |E(0,0)|$ is the electric field strength at the beam center. Equation (3.1) has several important properties worth to mention. The quantity w is the beam radius (spot size) and is a function of z, the distance from the beam waist. At the beam waist then w attains its minimum size ,w_0, also called the beam waist radius. The third exponential term gives the phase produced by a spherical wavefront with radius of curvature $R(z)$. All Gaussian modes have the same dependence of w and R on z, that is given by

$$w(z) = w_0 \sqrt{1 + \left[\frac{\lambda z}{\pi w_0^2}\right]^2}, \quad \text{and} \tag{3.2}$$

$$R(z) = z \left[1 + \left[\frac{\pi w_0^2}{\lambda z}\right]^2\right]. \tag{3.3}$$

The total power density of a Gaussian mode is proportional to $P \sim |E(r,z)|^2$. At the beam waist w_0, the radius of curvature R is infinite which means that we have plane

waves when $w(z = 0) = w_0$. Notice however, that the position $z = 0$ is not necessarily the position of the source producing the plane waves. The source is very likely to be placed on the negative side of the z-axis which is mostly the case. At large distances from the beam waist, the divergence of the beam radius is given by

$$\Theta_{w_0} = \frac{\lambda}{\pi w_0} \tag{3.4}$$

which can be derived from the Eq. (3.2). The term Θ_{w_0} is also called *divergence angle.* It turns out that the minimum waist radius $w_{0,min}$ for the Gaussian beam solution to be accurate is not defined precisely, but is approximately $\lambda/2$. This minimum waist is ensured in the case for all the measurements done on the ITER horn. The equations (3.2) and (3.3) are widely used in optics and will be used throughout this chapter to fit the measurements with the expectations.

3.3   The CTS diagnostic for ITER

Following the ITER design review, the CTS subsystem with the receiver antenna on the LFS has been enabled in the current ITER baseline design [13]. With this CTS subsystem, the near perpendicular velocities of fast ions can be measured at several locations simultaneously. Here, we discuss a CTS subsystem with the receiver antenna on the HFS which would enable resolution of near parallel velocities of the fast ions. The design of both CTS subsystems has progressed considerably [84, 52, 39, 69]. The envisaged additional CTS system with the receiver on the HFS will utilize a 60 GHz gyrotron with 1 MW power as probing beam. The system is capable of resolving the fast ion distribution in at least 16 velocity intervals with a spatial resolution of at least $1/10^{th}$ of the minor radius and a time resolution better than 100 ms [7]. The probing beam enters the plasma from the LFS equatorial port plug and is received on the HFS. In terms of technology, the CTS system for ITER differs from the previous successful CTS experiments on other machines due to much larger heat and neutron fluxes in the ITER experiment. This radiative environment results in different choices in materials and design as compared to other machines. Secondly, the CTS system for ITER has to be designed within the geometric constraints given by the machine. To protect the other systems (e.g., the superconducting coils) from the severe neutron and heat flux, the slits providing optical access to the plasma have to be as narrow as possible. The scattered CTS signal captured on the HFS in the vessel first needs to go from the plasma through the slit in the blanket of the inner wall of the vessel. Therefore, a slit with a dimension of 500 mm width and 30 mm height should be cut in the blanket. Figure 3.1 shows the part of the blanket out of which the slit needs to be cut. A microwave beam passing through this aperture is an astigmatic Gaussian beam for which the horizontal beam width is 100 mm and the vertical beam width is 10 mm. The aperture should be large enough to capture 1.6 times the Gaussian beam width in order to catch 99.4% of the radiation and to avoid reflections. This will result in an aperture opening of 300×30 mm. The minimum required vertical slit dimension was obtained from a full wave simulation. The beam passing this aperture is astigmatic. However, at the receiver antenna, an isotropic beam is preferred because of the design of the receiver horn antenna. Therefore, mirrors behind the blanket are required to reshape the astigmatic Gaussian beam into an isotropic Gaussian beam. We refer to this beam as the center beam. Hereby we also assume that the scattered radiation coming from the plasma is not too far from the plane wave, meaning slowly varying amplitude of the electric field in the z direction. The mirror system and the horn antenna are designed for optimal transmission
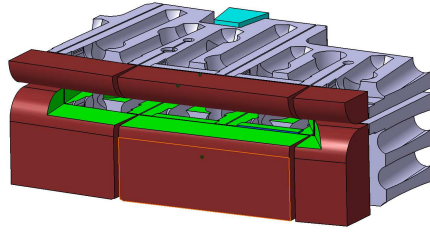
Figure 3.1: The additional envisaged CTS system on ITER with an antenna on the HFS would require a slit (green, 500×30 mm) in the blanket of the inner wall. The figure is reproduced with permission [46].

of the center beam. Since the fast ion distribution shall be measured at several locations in the plasma, beams from different incident angles ($\pm 15°$) in the horizontal plane shall be accepted. This requires the enlarged aperture in the horizontal direction with a width of approximately 500 mm. Beams coming from different angles with respect to the center beam require different horn positions since the mirrors are fixed. The distance between these horn antennas determine the distance between measurement locations in the plasma. In this work, only the center beam is considered.

3.4   Design of the HFS antenna

The space for the mirrors behind the blanket is limited to 190 mm vertically, 300 mm horizontally, and 230 mm radially. The beam parameters at the slit in the blanket are given by the slit dimensions. The mirror shapes for a quasioptical transmission line were assumed to be a surface of a torus, while the major and minor radii of the torus could be varied in the computations. The reflection of an incoming beam on a surface (in our case the torus surface) was calculated and fitted to an astigmatic Gaussian beam. Several iterations where required to find a good solution. The computing code is based on Matlab language and has been written in-house by Henrik Bindslev.

The distance between two adjacent measurement locations in the plasma is determined by the distance between two adjacent horn antennas and therefore limited by the beam size. A small beam size allows a close arrangement of the horn antennas and therefore allows decreasing the distance between measurement locations in the plasma. In order to reshape an astigmatic beam with given widths and curvatures at the beginning and at the end of the beam, at least two mirrors are required. Due to the large difference in the beam dimensions between slit and horn antenna, the reshaping should be performed on a propagation path long enough to be well within the paraxial approximation of Gaussian beam propagation. Due to the limited space, a long, straight path is not possible. Therefore, two additional mirrors were employed to increase the optical path length between the slit and the horn antenna. The mirror shapes, which are required to reshape the beam according to these boundary conditions, are calculated. Mathematically, the mirrors are surfaces of tori. The mirror surfaces and the beam shape are shown in Fig. 3.2. The beam enters the receiver at the top and leaves at the bottom. Figure 3.3 shows the beam width for the two major axes along the path of propagation through the quasi-optical transmission line. The triangles indicate positions of the mirrors, the diamond indicates
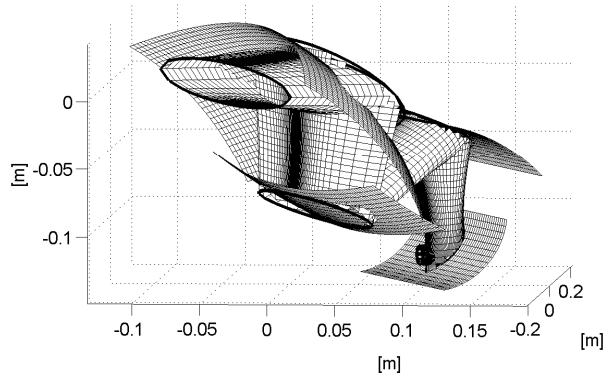
Figure 3.2: Calculated mirror shapes and transmission of the astigmatic Gaussian beam. The four mirrors are shown as toroidal surfaces. The beam is indicated by the surface containing 99.4% of the beam power. The beam enters the receiver at the top and leaves at the bottom. The figure is reproduced with permission [46].

the position of the beam waist. At this position, the isotropic Gaussian beam has a waist of 4.5 mm, and it is located 3.4 mm inside the horn antenna. The horn antenna is connected to a fundamental waveguide by means of a taper. The data for the mirror surfaces were imported into the computer-aided design (CAD) software CATIA Version 5 where the hardware design was made. Figure 3.4 shows the mirror assembly, and Fig. 3.5 shows the mirror assembly integrated in the blanket. Figure 3.5 shows also the design which has been set up in the laboratory as a 1:1 mock-up in order to verify the calculation of the beam propagation. The corrugated horn antenna shall accept an isotropic Gaussian beam with a beam waist of 4.5 mm corresponding to a divergence angle of 20.3°. A corrugated horn antenna for a frequency of 60 GHz was designed and built based on previous work [95].

3.5 Beam characteristics of the HFS antenna

The designed horn and mirrors are tested by the CTS group in Denmark. These components are purely passive so in order to characterize them we need a source and a detector for the frequency range of interest. The source is shortly described in Sec. 3.5.1 while the detection is somewhat more involved since we need to measure a radiation pattern. A convenient way to do this is to use a planner microwave scanner controlled by two step-motors for the horizontal and vertical movements, respectively. The scanner needs to have a certain size of the scan platform, typically 1.5 × 2 meters, in order to cope with large radiation patterns. Similarly, the distance between the quasi-optic component to be characterized and the scanner should correspond to the experimental set up during plasma discharge, i.e. distance between the component and a plasma or distance between the component and the next quasi-optic element. The scanner can be used for any desirable frequency, it all depends on the the type of detector installed on the moving arm. An example on data from the microwave scanner is depicted in Fig. 3.6. Generally, it is advantageous to choose the distance between two connecting quasi-optical elements large enough that the far-field approximation is valid [1]

$$r \geq \frac{2D^2}{\lambda}, \tag{3.5}$$
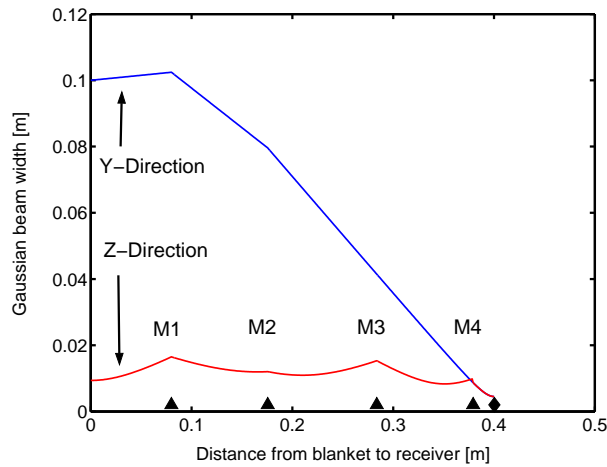
Figure 3.3: Gaussian beam widths in the two orthogonal directions in the transmission lines. Between the reference point and mirror M1, the two orthogonal directions coincide with the y-axis (blue curve) and the z-axis (red curve). The triangles indicate the mirror positions M1 to M4 and the diamond indicates the position of the waist which is located slightly inside the horn antenna. See also Fig. 3.8. The figure is reproduced with permission [46].
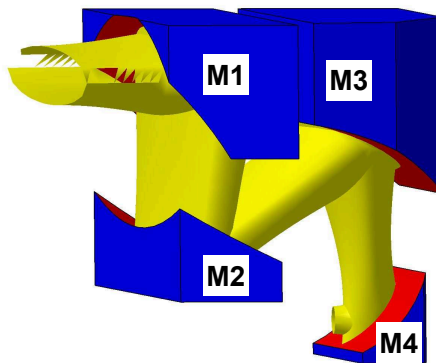
Figure 3.4: Mirror assembly (Mirrors M1-M4) for the HFS CTS transmission line. The red surfaces are the mirror surfaces calculated and imported into CATIA. The yellow surface represents 1.6 times the Gaussian beam width of the astigmatic Gaussian beam. See also Fig. 3.8.
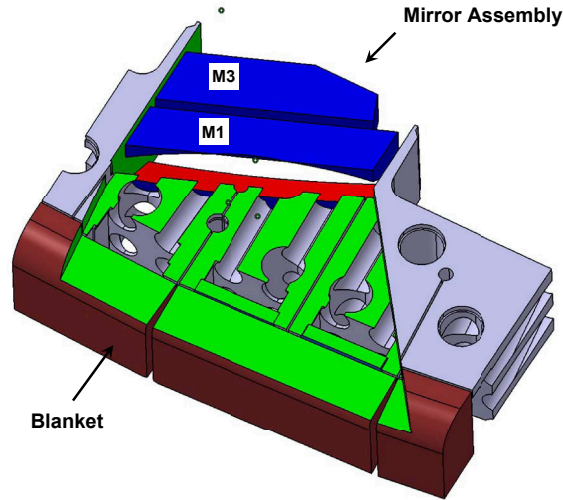
Figure 3.5: Mirror assembly for the proposed antenna on the HFS integrated in the blanket of the inner wall of ITER. The cutting surface of the blanket is depicted in green. Only the mirrors M1 and M3 (blue) and the surface of mirror M2 (red) of the mirror assembly can be seen. See also Fig. 3.4 and 3.8. The figure is reproduced with permission [46].

where D is the largest dimension of the radiating element and λ is the wavelength of the source. Additionally, the far-field approximation implies maximum phase error of 22.5^o. However, testing in far-field is far from possible for any frequency or radiator. For instance in our case, the wavelength of a 60 GHz signal is 5 mm in free space and the approximate size of the mirrors, we present here, is 200 mm. Inserting these numbers into Eq. 3.5 we get $r \geq 16\ m$. For electrically large radiators, the distance to the far-field is relatively long and therefore the measurements are associated with loss. In fusion experiments, the distance between the quasi-optic components is sufficiently short that the electric and magnetic fields are described by the near-field- or near far-field approximation [1].

3.5.1   The characteristic of the corrugated horn antenna

In order to verify whether the horn meets the requirements, a 60 GHz oscillator was mounted at the port of the horn, and the device was used as a mm-wave source. The beam pattern in front of the horn opening was measured at various distances from the horn. Figure 3.7 shows the Gaussian beam width versus the distance for two orthogonal directions. From these measurements, the divergence angle is obtained. The beam was found to be slightly elliptical with a measured deviation of less than 3% from the ideal circular pattern. The divergence angles for the major and minor axes were found to be 19.0° and 19.8°, respectively. This corresponds to beam waists of 4.8 mm and 4.6 mm (inside the horn antenna), respectively. The measured beam sizes in two orthogonal directions are in good agreement with the designed beam sizes.

3.5.2   The characteristic of the mirror system

In order to test the propagation of radiation through the entire receiver optics, the horn antenna is integrated into the mirror assembly (see Fig. 3.8). A detector, which is movable
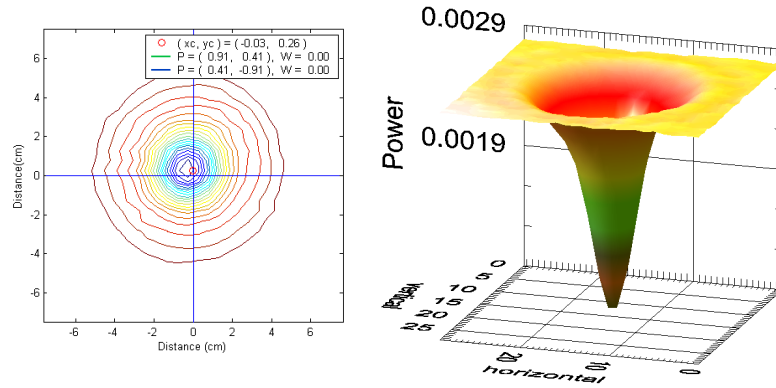
Figure 3.6: The plot with linear contour levels showing an example of a horn calibration for ASDEX Upgrade using planner microwave scanner. Distance between the horn and the detector is 605 mm. The source is an up-converter using an LO at 97.2 GHz and a signal generator at 7.8 GHz with 2.5 dBm signal power with an output of approximately 0 dBm at 105 GHz. The detector is from Millitech, type DXP-10 also called "general purpose detector".
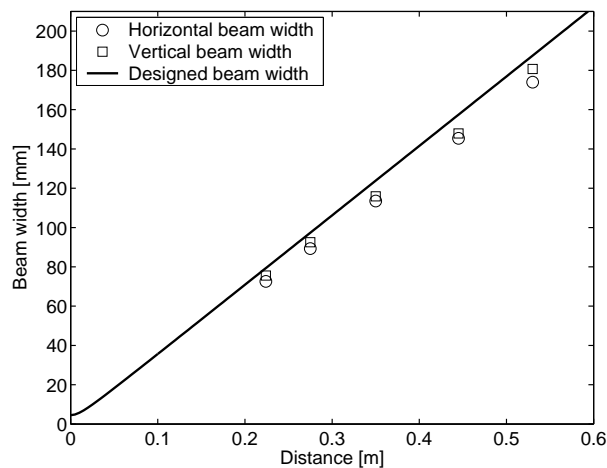
Figure 3.7: Gaussian widths of the beam leaving the horn antenna. The horizontal and vertical beam widths should be identical, as the horn has a circular symmetry. The error is less than 3% between the measured beams in two orthogonal directions. The solid line represents the designed beam width.
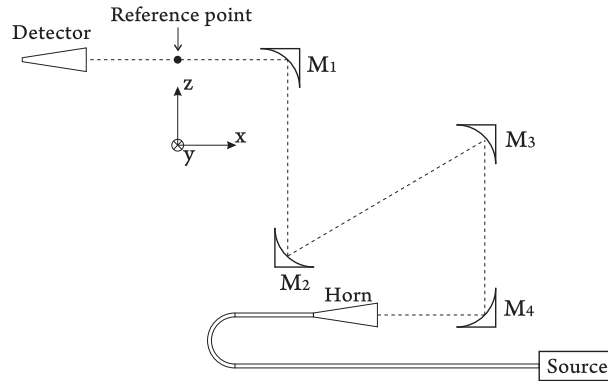
Figure 3.8: Schematic of the mirrors (M1-M4), the horn antenna, and the detector diode. The origin of the graphs in Fig. 3.3 and Fig. 3.10 coincides with the reference point. The distance on the abscissa in Fig. 3.3 is measured from the reference point toward the horn antenna; in Fig. 3.10 it is measured toward the detector.
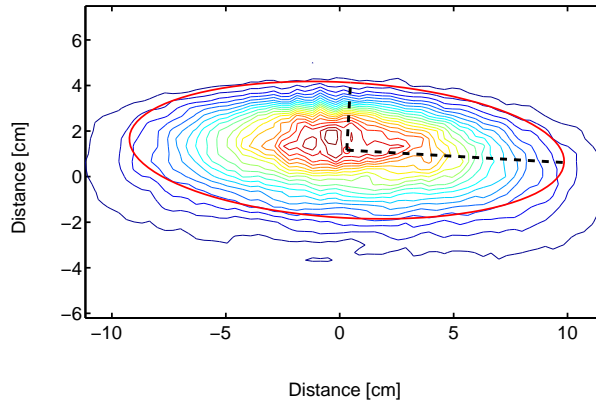
Figure 3.9: The plot with linear contour levels shows the radiation intensity in the y-z-plane at a distance of 166 mm from the reference point (see Fig. 3.8). The dashed lines show the width in the direction of the major axes of the astigmatic beam.

in the y-z plane, is used to characterize the beam pattern at various distances x from the reference point (Fig. 3.8). Figure 3.9 shows a contour plot of the beam intensity in the y-z plane at a distance of 166 mm from the reference point. The distance between the reference point and M1 is 80 mm. The beam widths in the y- and z directions at various distances from the reference point are shown in Fig. 3.10. The circles in Fig. 3.10 show the divergence of the beam from the reference point in the z-direction. The beam waist is calculated from the divergence angle and is found to be 8.3 mm. This is within an error of 13% compared to the calculated value of 9.4 mm. The squares in Fig. 3.10 show the beam width at approximately 100 mm in the y direction. A converging beam can be seen in the y-direction. The calculation (solid curve through the squares in Fig. 3.10) shows a converging beam with a beam waist of 47 mm at a distance 2.7 m away from the reference point. The beam could not be measured at distances larger than 0.35 m from the reference point due to a low detected signal (low signal-to-noise ratio) which gives rise to a high uncertainty for the fitting to the Gaussian beam. However, the general characteristic is in agreement with the calculation. Microwave sources providing higher output power will be employed to gain more signal and thereby overcome this problem.
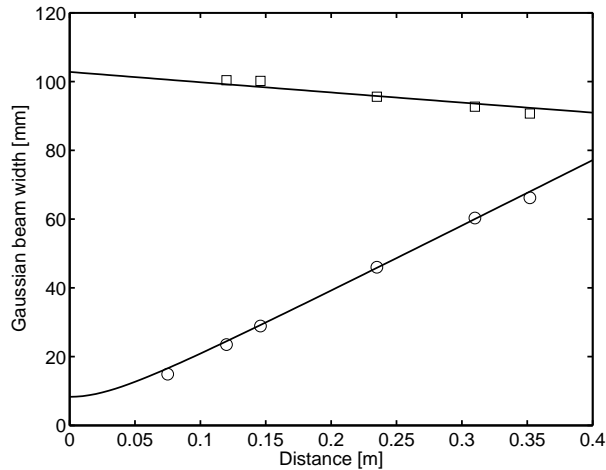
Figure 3.10: Propagation of the y- and z component of the astigmatic Gaussian beam into the vessel. The squares show the horizontal component and the circles show the vertical component. The solid lines represent the calculated beam widths. See also Fig. 3.8.

3.6   Discussion

We find it important to resolve the near parallel velocity components of the fast ion distribution. Here we presented a compact design solution of an antenna for such a system which can be accommodated on the HFS of ITER. A design for an additional antenna on the HFS for the CTS system at ITER is machined and measured. The required shape of the mirrors in order to ensure an acceptable beam has been computed. The antenna system, consisting of mirror assembly and horn antenna has been verified experimentally with a 1:1 mock-up. Also, during ITER plasma heating the HFS side will be exposed to a substantial amount of heat due to electromagnetic radiation and neutron flux that will influence impact on the surface of the designed mirrors [69]. However, since the surface area of the HFS mirrors and the opening in the vessel wall are relatively small the impact due to radiation and neutron flux is expected to be limited.

Chapter 4

CTS Receiver at ASDEX Upgrade

4.1 Short background and introduction

The principles behind CTS receiver installed at ASDEX Upgrade are presented in this chapter. The receiver can detect spectral power densities of a few eV against the ECE background on the order of 100 eV under presence of gyrotron stray radiation that is several orders of magnitude stronger than the signal to be detected. We present measurements of the transmission characteristics and performance of the main receiver components operating at mm-wave frequencies (notch-, bandpass- and lowpass filters, a voltage-controlled variable attenuator, and an isolator), the down-converter unit, and the intermediate frequency (IF) components (amplifiers, bandpass filters, and detector diodes). Furthermore, we determine the performance of the receiver as a unit through spectral response measurements and find reasonable agreement with the expectation based on the individual component measurements.

Radiometers are remote sensing instruments that collect electromagnetic radiation in the millimeter and submillimeter wavelength range (30 GHz-3 THz) and measure its spectral power density. The CTS receiver we discuss here is a radiometer designed to detect radiation in the frequency range 100-110 GHz with a heterodyne detection scheme. This is the expected Doppler-shift frequency range for gyrotron 105 GHz radiation scattered due to presence of fast ions with energies up to 500 keV in the plasma at ASDEX Upgrade (AUG). Seen from a broader perspective, there exist three types of radiometer that are suitable for usage as microwave receivers in hot plasma diagnostics. The first type is the total power radiometer (TPR [83, 75]) which is the type that we use to detect the scattered signals from fusion plasmas. A TPR is characterized by simple detection of the electromagnetic radiation seen by the quasioptical mirrors and horn. The radiation is then divided in several channels by a heterodyne method, and then the average power in each channel is converted linearly to a voltage using square law diodes. The second type is the Dicke radiometer (DR [75]) which is used not to measure directly the antenna temperature as in TPR, but rather difference between this and some known reference temperature. The sensitivity of the measurement to gain and noise temperature instabilities is greatly reduced. The third type is the noise-injection radiometer (NIR) which represents a step towards best achievable accuracy, meaning the output is independent of gain and noise temperature fluctuations. NIR is a specialized type of DR where the condition of equal reference temperature and antenna temperature is continuously ensured by a servo loop. Overviews of heterodyne methods used for plasma diagnostics are given
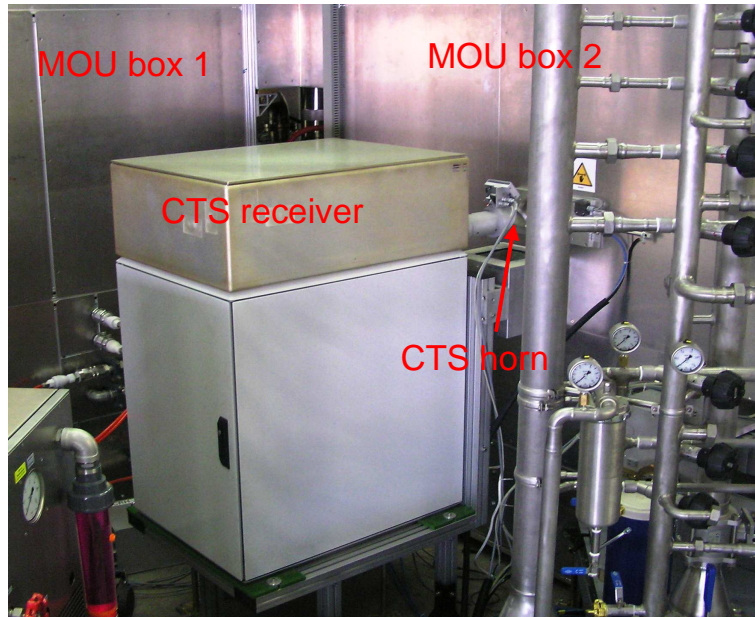
Figure 4.1: AUG CTS receiver.

in [33, 48].

CTS receivers have been used for a variety of measurements at several tokamaks and stellarators, for example at JET [6], W7-AS [78, 79], FTU [80, 81], TEXTOR [55, 58, 59, 91], ASDEX Upgrade [53, 54, 70] or LHD [44]. Many parameters can be measured by CTS [40], for example the ion temperature [78] or the fuel ion ratio [41, 77]. The setup of the AUG CTS receiver presented here is designed to detect energetic particles [53, 54, 70]. The technical challenge is to design a radiometer that can detect spectral power densities of a few eV against the ECE background on the order of 100 eV. To distinguish the CTS signal from the ECE background, the gyrotron is modulated using on/off periods. While the gyrotron is off, we measure the ECE radiation, and while the gyrotron is on, we measure the sum of ECE background and CTS signal. The difference between the two levels is the CTS signal. During the phases in which the gyrotron is on, one additionally has to deal with gyrotron stray radiation that is several orders of magnitude stronger than the signal to be detected. CTS, as well as other diagnostics using millimeter waves, is well-suited for the strongly radiative environments of ITER or future fusion reactors [69, 52, 46]. A CTS diagnostic has been enabled in ITER and will allow detection of the energy distribution of alpha particles in the burning plasma of ITER [71, 67, 68].

In this chapter we will discuss the design and performance measurements of the main components of the CTS receiver installed on AUG. AUG is equipped with dual frequency 1 MW gyrotrons (105 GHz and 140 GHz) which is operated at 105 GHz for CTS experiments [89, 88]. The radiation from the gyrotron is launched into the plasma via a quasi-optical transmission line consisting of five reflectors and an electrically long, circular, overmoded waveguide. The receiver collects part of the scattered radiation via a similar quasi-optical transmission line. After the quasi-optics the scattered radiation enters a circular horn antenna which is tapered down to a single-mode circular waveguide. Then we use a circular-to-rectangular waveguide converter to guide the radiation further into the heterodyne microwave receiver.

A schematic of the AUG CTS receiver is shown in Fig. 4.2. All components are placed in an electrically shielded box, called "AUG CTS box" in Fig. 4.2. The radiation enters
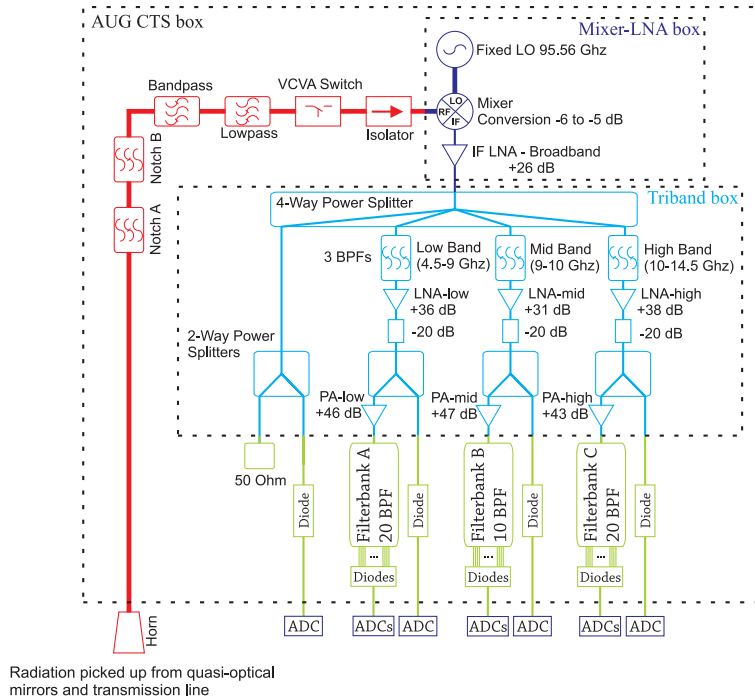
Figure 4.2: Schematic of the AUG CTS receiver. The dashed lines represent shielding boxes in which the receiver components are installed. The RF line is shown in red; the mixer, the LO and the broadband LNA in the mixer-LNA box are shown in dark blue; the components in the triband box are shown in blue; and the filterbanks A, B and C and the detector diodes are shown in green.

the horn antenna and passes through the RF line (red in Fig. 4.2) consisting of the horn antenna, two notch filters (General Atomic), a bandpass filter (ELVA-1, BPF-10/104/8), a lowpass filter (ELVA-1, LPF-10/112), a voltage controlled variable attenuator (VCVA by ELVA-1, VCVA-10/105/2) and an isolator (ELVA-1, IF-10). Then the RF signal enters the mixing stage where the signal is heterodyned to intermediate frequencies (IF). The local oscillator (LO by ELVA-1, CIDO-08/95.5/20), the mixer (ELVA-1, BM-08/95.5/14.5) and a wideband low noise amplifier (LNA by Mini-Circuits, ZVA-183) are placed in a shielded compact copper box, called "Mixer-LNA box" (dark blue in Fig. 4.2), in order to screen out LO signals. The IF signal at the LNA output is divided using a four-way power divider and three bandpass filters into three frequency bands. Each of the three frequency bands is furthermore equipped with a cascade of two IF amplifiers, the first is an LNA (Miteq AFS4) and the second is a power amplifier (PA by Miteq AFSD6). These components are located in a shielded box that is called "Triband box" shown in blue (Fig. 4.2). The fourth branch in the triband box is used for auxiliary purposes only. After the triband box the IF signal is fed to the filterbanks A (4.5 - 9 GHz), B (9 - 10 GHz), and C (10 - 14.5 GHz) and divided into a total of 50 channels using bandpass filters and power dividers. Filterbanks A and C have 20 channels each whereas filterbank B has 10 channels. In each channel, the power after the bandpass filter is converted to a DC voltage using a square-law detector diode. The voltage is recorded using a 24 bit analog-to-digital converter (ADC).

Before plasma discharges with CTS experiments, the receiver is calibrated. The receiver views eccosorb at liquid nitrogen temperature and at room temperature, giving two calibration points, i.e. the so called hot-cold calibration or Y-parameter method. A straight line is drawn between the points and thereafter extrapolated to the experimental
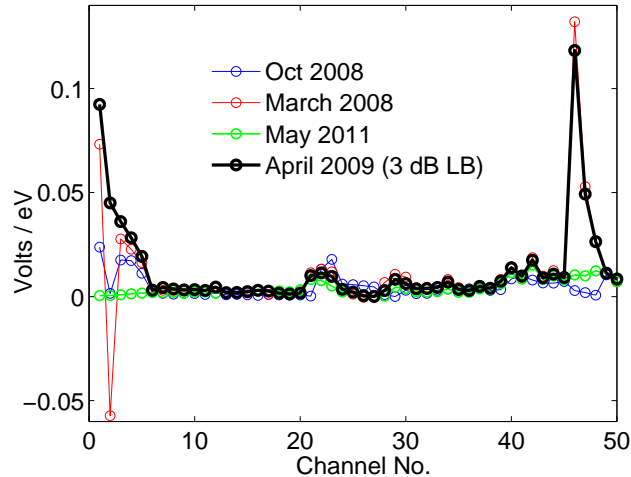
Figure 4.3: Progressive calibration procedure of the CTS receiver at ASDEX Upgrade. The y-axis is given in volts per eV which is equivalent to volts per power. We see that the outer channels collected a substantial amount of power and therefore we used attenuators before the square-law diodes in order to flatten out the calibration curve as a function of channel number.

temperature viewed by the receiver. The present calibration method assumes linearity in the temperature range radiated from the plasma. If possible a third calibration point can be taken by viewing a plasma with a resonance in X-mode. Here the plasma temperature must then be available from an independent measurement. In Fig. 4.3 we show present and old curves using hot-cold calibration method. Since we use 3 IF amplifiers in the chain the receiver is sensitive to relatively small changes in the temperature. Also, the first five- and the last five channels are at least four times broader than the rest of the channels making it possible to pick up more signal during hot-cold calibration. Therefore, adjustments performed with attenuators before the square-law diodes are the best solution to flatten out the calibration curve as a function of channel number. Finally, the sensitivity of the square-law diodes can vary considerably between two random diodes.

In the following we will discuss performance measurements of each component in the order the radiation encounters them on its way through the receiver: The notch filters, the bandpass and lowpass filters, the VCVA and the isolator in the RF line (Sec. 4.2), the mixer and the LNA in the mixer-LNA box (Sec. 4.3), the power divider, bandpass filters and amplifier chains in the triband box (Sec. 4.4), the filterbanks (Sec. 4.5), and the diodes (Sec. 4.6). We will conclude with a measurement of the spectral response of the entire receiver and compare it with the expectation based on the individual component measurements (Sec. 4.7). Our conclusions are drawn in Sec. 4.9.

4.2   Components in the RF Line

The RF line contains two notch filters in cascade, a bandpass and a lowpass filter, a VCVA and an isolator (see Fig. 4.2). In this section we discuss these components. Radiation entering the RF line via the horn antenna encounters first two cascaded notch filters. Their stopband center frequency f_0 is tuned to the gyrotron frequency 104.95 GHz. Gyrotron stray radiation is suppressed whereas scattered radiation in the range 100-110 GHz passes on either side of the stopband [23, 24, 26, 17, 15, 16]. The attenuation of each notch filter
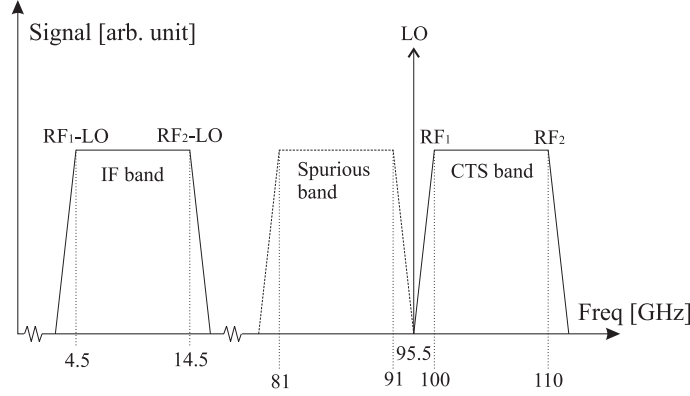
Figure 4.4: CTS band and the image band (spurious band) that converts through the mixer stage to the same IF band.

is more than 50 dB in the stopband as shown in Fig. 4.5(a). The insertion loss is about 2 dB in most of the passband. We define insertion loss (IL) as the ratio between received (port 2) and inserted power (port 1) in dB, i.e. IL $= -20\log_{10}|S_{21}|$ in terms of two-port S-parameters. This is the well-known S-parameter S_{21} with a negative sign. The attenuation of both notch filters is stronger for frequencies above 108 GHz, such that the attenuation at 110 GHz is about 10 dB. This is due to the selected cavity diameter and the ratio between the cavity diameter and the cavity length that place the cavity resonances close to the upper range of the desired passband ($\sim$110 GHz) and thereby introduce additional attenuation.

The 3 dB bandwidth of notch filter A is around 280 MHz and that of notch filter B is around 250 MHz. For a bandwidth of 130 MHz centered at 104.95 GHz, we find that the stopband attenuation is more than 54 dB for notch filter A and more than 52 dB for notch filter B. Due to the fact that the gyrotron probing beam is considerably stronger compared with ECE levels, we need two notch filters in cascade to damp the gyrotron stray radiation to the level of the ECE. High incoming power can saturate or even damage active components in the receiver. Radiation at the horn antenna is only a fraction of the available gyrotron power ($\sim$600 kW or 88 dBm), so if for example 0.1% (58 dBm) of the gyrotron power enters the horn antenna, the power at the output of notch filter B will be less than -48 dBm. Since a dynamic range more than 70 dB for signals in W-band is not easily measured with present network analyzers, we use two matched notch filters with stopband attenuation in the range 50 - 60 dB each to assure sufficient attenuation of the gyrotron stray radiation.

The next component along the RF line is the bandpass filter. Plasmas radiate in a wide range of frequencies, also below 100 GHz. As our LO frequency is about 95.5 GHz, radiation at 81 - 91 GHz will be mixed to the same IF frequencies as radiation at 100 - 110 GHz. This is indicated in Fig. 4.4 where the radiation at 81 - 91 GHz is called upper and lower side band. The RF bandpass filter has a passband that covers the range 100-110 GHz but suppresses the image response at 81 - 91 GHz more than 70 dB as shown in Fig. 4.5(b). The bandpass filter has an opening (low damping) at around 140 GHz, which is unfortunate since AUG plasmas are frequently heated by electron cyclotron resonance heating with gyrotrons at 140 GHz. A low-pass filter is installed in the RF line after the bandpass filter to block stray radiation from these 140 GHz gyrotrons. The transmission characteristic of the bandpass filter has also been measured. The attenuation at 140 - 200 GHz is more than 25 dB whereas the insertion loss at 100 - 110 GHz, the relevant

frequencies for CTS, is in the range 2.5 to 3 dB. The cut-off frequency of the lowpass filter is 112 GHz.

The next component in the RF line is the VCVA. In CTS experiments the gyrotron is frequently modulated: 2 ms on / 2 ms off. During the switching phases the gyrotron chirps so that for a short time the gyrotron frequency, though at power levels much lower than maximum, is outside the stopband of the notch filters [54]. The chirping of the gyrotron installed at AUG is shown in Fig. 2.10 where the relatively high chirping drawn as light-blue area is attenuated with VCVA. Gyrotron stray radiation would then bypass the notch filters and enter the receiver which could lead to gain compression of the IF amplifiers. We place a VCVA in front of the mixer to attenuate the signal during the gyrotron switching phases. While the VCVA is in closed mode, it will attenuate the input signal by 40 dB or more, but it will introduce ∼2 dB insertion loss when it is open (see Fig. 4.5(c)).

The last component in the RF line is the isolator which is used to damp back-reflections and prevent signals, for example from the LO, from leaking back into the RF line. The isolator will minimize standing waves in the RF line at the cost of additional insertion loss that we measure to be around 1 to 2 dB.

We can calculate the transmission of the cascaded system from the individual component measurements by summing up the S-parameters of all components in the RF line. The results are presented in Fig. 4.5(d). We used a linear summation of the component insertion loss (S_{21} in dB) because the return losses at connecting ports of each component are low, i.e S_{11} and S_{22} less than -15 dB are considered to be matched. We define return loss (RL) as the ratio between reflected and inserted power in dB, i.e. $\mathrm{RL}_{in,out} = -20 \log_{10} |S_{11}| \approx -20 \log_{10} |S_{22}|$ at input port 1 and output port 2, respectively. Such reflections are low since the connecting waveguide ports have the same dimensions implying that the characteristic impedance is the same. We therefore assume that we can predict transmission characteristics reliably if we just know S_{21}. In the passband range outside the deep notch, we measure an insertion loss of about 9 dB at frequencies below 108 GHz and up to 26 dB in the frequency range 108 - 110 GHz.

4.3   Mixer and IF Broadband Amplifier

After the isolator the radiation in the W-band range enters the mixer in the mixer-LNA box (Fig. 4.2). The mixer down-converts the radiation from W-band to the IF band. The IF is chosen at frequencies lower than the RF input since the sharpness of the IF filters determines how good different channels are separated in frequency. The mixer is pumped by an IMPATT diode [49] LO at 95.51 GHz with 13 dBm output power. The RF input power where the 1-dB compression point appears at the IF output is around 0 dBm. The mixer conversion loss is defined as difference between output and input powers evaluated at the IF and RF ports, respectively. The conversion loss is measured using a frequency multiplier (RPG, AFM6-110) (× 6, i.e. at the sixth harmonic) driven by a signal generator (Rohde & Schwarz, SMR20) and the output power is measured at the IF port using a power meter (Agilent Technologies, E4416A). The measurements are presented in Fig. 4.6. We find the conversion loss to be almost constant in the range 5 dB to 6 dB for the RF input in the range 100 - 110 GHz. The isolator will partly prevent LO self-mixing since any fraction of the LO signal leaking into the RF port will to a large part be absorbed in the isolator. Any unabsorbed part will be reflected back into the mixer RF port causing DC signals at the IF output port. Therefore a DC-block is integrated at the IF port of the mixer.

(a)   (b)

(c)   (d)
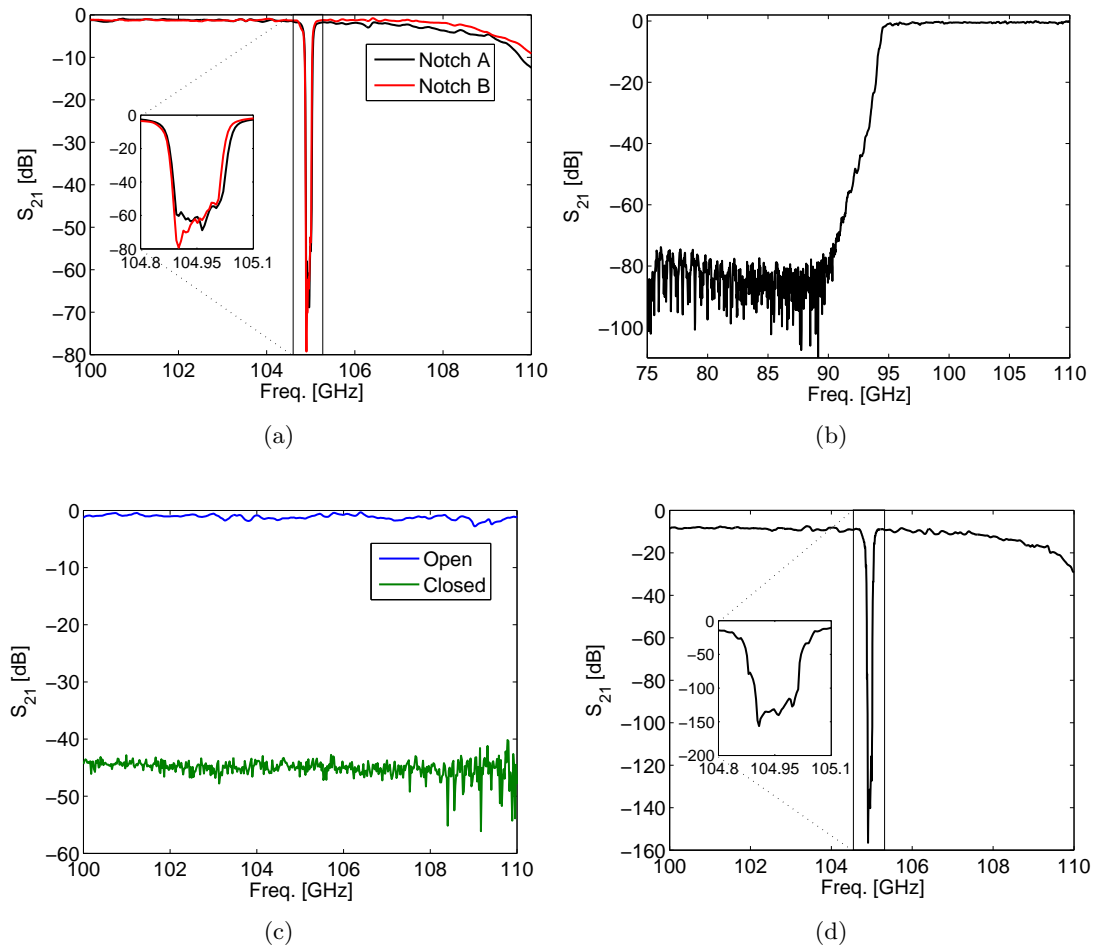
Figure 4.5: Insertion loss of components in the RF line: (a) two notch filters measured separately for the frequency range relevant to CTS experiments at ASDEX Upgrade (100 - 110 GHz); (b) bandpass filter; (c) VCVA in open and closed mode; (d) Total insertion loss of the RF line.
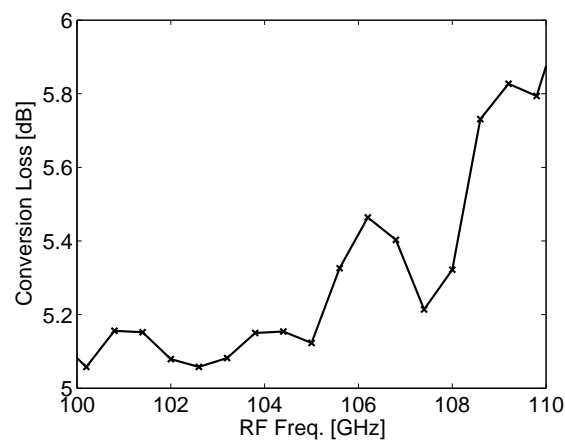

Figure 4.6: Mixer conversion loss in the frequency range relevant to CTS experiments.

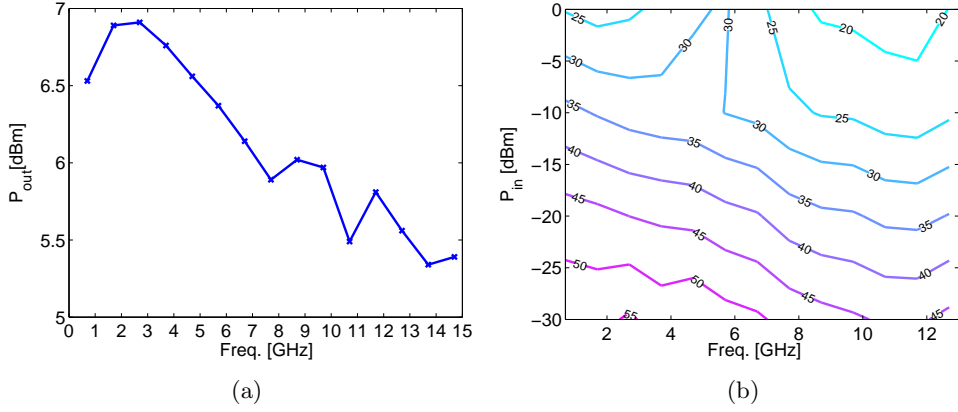(a)   (b)

Figure 4.7: IF amplifier characteristics: (a) Measured output power spectrum of the IF amplifier for an input power of $P_{in} = -20$ dBm; (b) The second harmonic generated at various frequencies and input powers. The isocontours represent the ratio of the power between second harmonic and fundamental at the output in dB.

In order to reduce the receiver noise figure (NF), an IF broadband amplifier is placed right after the mixer IF port in the mixer LNA-box and is the first stage of amplification. It covers the full CTS IF spectrum from 4.5 to 14.5 GHz with amplification of about 26 dB as shown in Fig. 4.7(a). The amplifier gain has been tested for several input powers for the frequency range from 2 to 15 GHz and is confirmed to vary only by 1 to 2 dB in all cases. The noise figure is in the range from 3.0 to 5.5 dB. The 1 dB compression point is about 0 dBm input power, which is orders of magnitude higher than the power expected during CTS experiments.

The broadband amplifier is expected to operate linearly in the IF range from 4.5 to 14.5 GHz. However, second harmonics generated from signals between 4.5 and 7.25 GHz can erroneously be interpreted as CTS signals between 9 and 14.5 GHz. Therefore the generation of second harmonics has been measured for various input power levels, as seen in Fig. 4.7(b). The second harmonic is suppressed by more than 40 dB (relative to the fundamental) at low frequencies (2 to 6 GHz) and low input powers (-30 to -15 dBm). At high frequencies (8 - 12 GHz) and high input powers (-10 to 0 dBm) the suppression is more than 25 dB, but the frequency range of the second harmonics (16-24 GHz) is outside the reception spectrum of the receiver and does not interfere with the CTS signal. Input power higher than -30 dBm is unlikely during CTS experiments, so we expect to have at least 45 dB suppression of the second harmonic in the IF frequency range.

We can determine the total noise factor F_{chain} from the horn antenna to the output of the IF broadband amplifier and further to the four-way power divider using Friis' formula [45] for cascaded two-port devices.

$$F_{chain} = F_1 + \frac{F_2 - 1}{G_{av,1}} + \frac{F_3 - 1}{G_{av,1}G_{av,2}} + \dots \qquad (4.1)$$

where F_1 is the noise factor of stage 1 and $G_{av,1}$ is the available power amplification from stage 1 and similarly for stage 2, 3 and further on. The terms on the right-hand-side of Eq. (4.1) are expressed in linear scale. The noise factor of the RF line together with the mixer (RF to IF), F_1, is equal to the system loss, i.e. for passive components $F_1 = G_{av,1}^{-1}$. F_2 and $G_{av,2}$ represent the noise factor and available gain of the broadband LNA, respectively. F_3 is the loss of the four-way power divider discussed in Sec. 4.4.
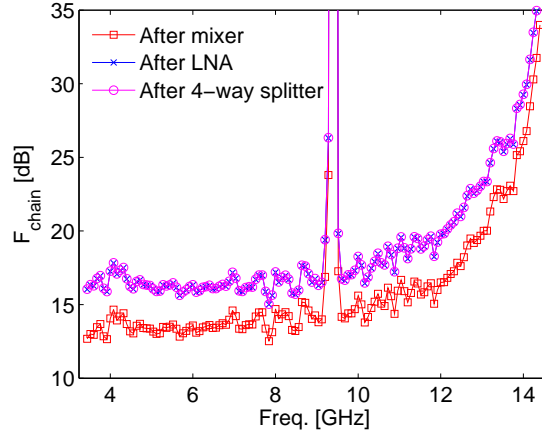
Figure 4.8: Noise figures of the cascade from the horn antenna to various places along the transmission line. The noise figures after the LNA and after the four-way power divider are very similar.

Eq. (4.1) can be simplified to

$$F_{chain} = F_1 F_2 + \frac{F_1(F_3 - 1)}{G_{av,2}} + \ldots \approx F_1 F_2. \tag{4.2}$$

When the noise factor F_{chain} is converted to dB by $\mathrm{NF}_{dB} = 10\log_{10} F_{chain}$, we refer to it as noise figure.

Figure 4.8 shows the noise figures at various points along the transmission line: after the mixer, after the LNA and after the four-way power divider. The total noise figure F_{chain} is very similar before and after the four-way power divider and in fact at any other place in the transmission line thereafter. F_{chain} is dominated by the losses in the RF line (F_1) times the noise figure of the LNA (F_2), as Eq. (4.2) also shows. The IF broadband amplifier is placed right after the mixer, so that the contribution to the receiver noise figure of all IF components further down the transmission line is as low as possible. This will lead to the optimum noise figure for the entire system.

4.4   Triband Box

After the IF radiation has passed the first stage of amplification, it enters the triband box which splits and further amplifies the IF signal as shown in Fig. 4.2. The first component in the triband box is the four-way power divider leading to three branches consisting of each a bandpass filter (Micro-Tronics) and a two-stage amplifier chain. The fourth branch is used for auxiliary measurements. The insertion loss of the four-way power divider is in the range from 6.5 to 7.5 dB over the frequency range 4.5 to 14.5 GHz. The insertion loss covers the inevitable loss of 6.0 dB due to four-way power splitting and 0.5 to 1.5 dB due to frequency dependent loss in the microstrip lines. The triband box splits the radiation into three frequency bands; a low band (4.5 - 9 GHz), a mid band (9 - 10 GHz) and a high band (10 - 14.5 GHz). The selection is made by a lowpass- and two bandpass filters with insertion- and return losses shown in Fig. 4.9. The filters have good selectivity, low insertion loss in the passband and broad rejection bandwidth.

The main reason for dividing the receiver line into three separate frequency bands is the different spectral power density ranges of the detected radiation. We expect larger spectral
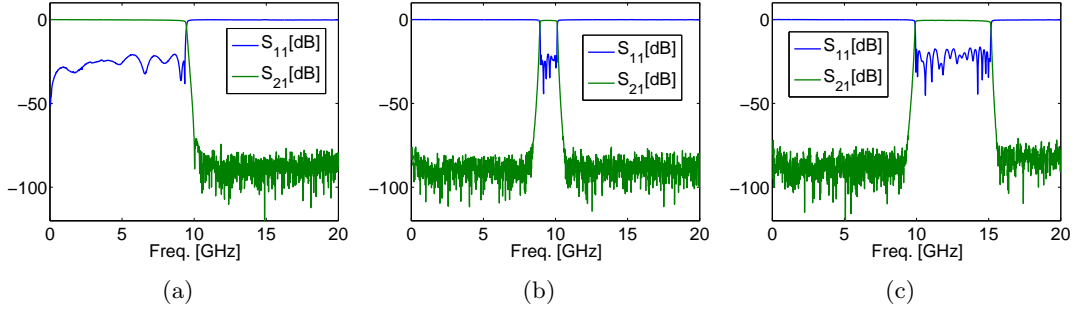
(a)   (b)   (c)

Figure 4.9: Insertion loss and return loss of the bandpass filters in the three frequency banks: (a) low frequency bank; (b) mid frequency bank; (c) high frequency bank.
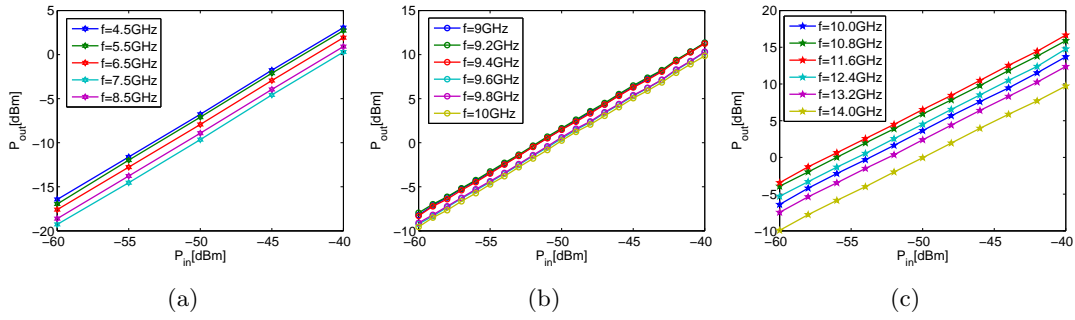

(a)   (b)   (c)

Figure 4.10: Output power versus input power for various frequencies: (a) Low bank amplifiers; (b) Mid bank amplifiers; (c) High bank amplifiers.

power densities in the range ± 500 MHz around the gyrotron frequency corresponding to scattering from bulk ions. Therefore our mid branch is 1 GHz wide while the two neighbor branches, where less radiation is expected, are each 4.5 GHz wide to cover the expected CTS frequency range. Another advantage of dividing CTS band into 3 sub-bands is channel protection of the low and high branches in the case of strong gyrotron stray radiation. That way only the mid branch is at risk to saturate while the low and high branches will be unaffected assuming the mixer is not saturated. The attenuators shown in Fig. 4.2 in each of the three bands are used to adjust the signal levels and to prevent standing wave arising between the amplifiers.

We investigate the linearity of the amplification in the triband box at different frequencies (Fig. 4.10). Since the slopes of the curves in Fig. 4.10 are unity, the response of the triband box is linear for input powers up to -40 dBm evaluated at several frequencies of interest in each of the three bands. Figure 4.11 shows the gain of the triband box in the IF frequency range (4.5 to 14.5 GHz) for an input power of -60 dBm. The low band is relatively flat with a gain in the range from 36 to 39 dB; the mid band is reduced in bandwidth due to the bandpass filter and has a gain in the range from 47 to 48.5 dB; and the high band has the largest gain variation in the range from 46.5 to 54 dB.

Electrical properties of the seven amplifiers in the receiver are shown in Tab. 4.1. In case we receive a broadband signal with increasing power level at the horn antenna, the components will saturate in the following order: the three PA's right before filterbanks A, B and C, the three LNA's driving the PA's, the mixer, and finally the broadband LNA driven by the mixer. These results are found by calculating the power budget at the input port of each component.
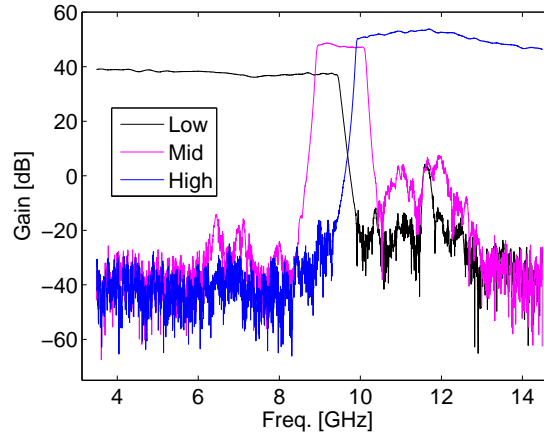
Figure 4.11: Gain of the triband box measured with a network analyzer. The test input power is -60 dBm. The signal is split into the three frequency bands given by the bandpass filter discussed in Fig. 4.9.

	Freq. [GHz]		Gain [dB]		Max output power [dBm]		Noise Figure [dB]	
	f_l	f_u	Min	Max	Min	Max	Min	Max
LNA-broadband	0.7	18	24	26	21	24	3.0	5.5
LNA-lowband	3	9	35.2	36.2	15.6	17.2	1.25	1.98
LNA-midband	9	10	30.4	31.1	15.1	16.5	0.92	1.31
LNA-highband	10	16	35.23	38.08	15.21	16.56	1.29	1.74
PA-lowband	3	9	42.5	46.1	25.2	26.7	3.34	4.97
PA-midband	9	10	45.7	47.7	25.3	26.0	1.27	1.30
PA-highband	10	16	40.46	43.19	24.19	24.42	3.29	3.59

Table 4.1: Amplifier specifications. The maximum output power is defined at the 1 dB gain compression point. f_l and f_u represent the lower and upper frequencies of operation, respectively.
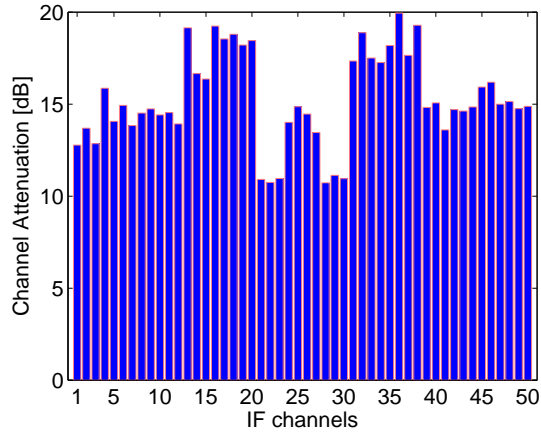
Figure 4.12: Attenuation (insertion loss) of each IF channel at its center frequency of the corresponding bandpass filters.

4.5   Filterbanks

The three IF branches leaving the triband box enter the filterbanks A, B and C. The three filterbanks consist of power dividers, jumpers and bandpass filters that are used to obtain tightly spaced channels in the frequency space. The bandpass filters have relatively sharp roll-off attenuation in the range 0.1-0.15 dB/MHz and a passband insertion loss in the range 0.2 - 0.6 dB. Filterbank A has 20 channels (4.5 - 9 GHz), filterbank B 10 channels (9 - 10 GHz) and filterbank C 20 channels (10 - 14.5 GHz). The channels are numbered consecutively from 1 to 50 in the order of ascending channel center frequency. The attenuation at the center frequency across all channels varies from 10 to 20 dB due to different types of power dividers needed to split the signal in the three main branches into 50 channels. Fig. 4.12 gives an overview of the design attenuation of the filterbanks. The spectral resolution in channels 6 to 45 is 100 MHz. In the outer channels larger bandwidths are chosen to increase the signal-to-noise ratio, i.e. bandpass filters with 3 dB bandwidths of around 500 MHz are used in channels 2-5 and 46-49 and of around 1.1 GHz in channels 1 and 50.

We have measured all microwave components from the horn antenna down to the output ports of the bandpass filters in the 50 channels. Using this measured data we can calculate the gain through the CTS receiver. Figure 4.13 shows the gain for a few representative channels in their relevant frequency ranges. The suppression of radiation at frequencies outside their prescribed passbands is more than 70 dB.

4.6   Square-Law Detector Diodes

The final stage of our interest in the AUG CTS receiver are the square-law Schottky detector diodes [96] (Herotek, High sensitivity zero bias Schottky detectors) that are connected to each of the 50 IF channels. The diodes transform the IF signal to a DC level which is then amplified by a factor 60 using operational DC amplifiers and afterwards recorded using ADC cards (National Instruments 4472). The ADC cards accept voltages from -10 V to 10 V giving 20 V in total dynamic range. The theoretical voltage resolution is $V_{ADC} = 20/2^{23}$ $V \sim 2.38$ μV which is far below the noise level detected during liquid nitrogen calibration. Since the square-law diodes have negative output polarity,
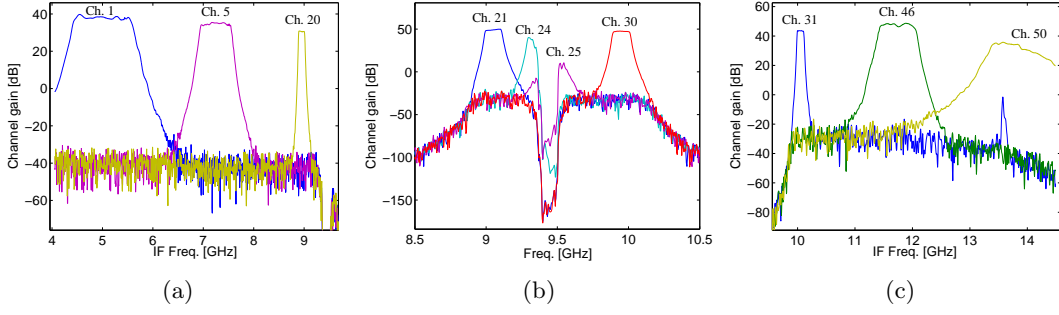
Figure 4.13: Calculated gain from the horn to the output port of bandpass filters for a few
representative channels in filterbank A (a), in filterbank B (b) and in filterbank C
(c).

we only use half of the total dynamic range, i.e. from -10 V to 0 V. The power-voltage
characteristics of the diodes are shown in Fig. 4.14. The diodes are tested using a signal
generator at the frequency that corresponds to the channel number at the IF input port.
The power of the signal generator is swept in power from -40 dBm to 0 dBm in 1 dB
steps, and the voltage at the output is measured with a voltmeter. Fig. 4.14(a) presents
the output voltage, U_{out}, as a function of input power, P_{in}.

Fig. 4.14(b) shows that the values of the gradient $-\mathrm{d}U_{out}/\mathrm{d}P_{in}$ are in the range from
300 to 3000 V/W for input powers from 0 to -40 dBm. These gradients are also called
diode sensitivities. For powers below -20 dBm, the diode operates in the square-law region
with approximately constant sensitivity of around 1000 V/W for all the channels except
42, 44 and 46. For powers more than -20 dBm, the diode operates in the resistive region
where the sensitivity decreases down to 300 V/W for 0 dBm power input. The diodes
in channels 42, 44 and 46 have sensitivities as high as 3000 V/W which are taken into
consideration during receiver calibration.

We can estimate the output voltage with good accuracy for arbitrary power in the
range between -40 dBm and 0 dBm. For low power input, < -30 dBm, we get uncer-
tainties in the voltmeter readout up to 0.1 mV. If the signal is lower ($<$-40 dBm), which
would be the case in most channels during experiments, we extrapolate the diode output
based on the measured data assuming that in this range the response should be linear.
The slope of the line is now determined as the intercept point with the y-axis is set to
zero since the diode voltage is zero for zero input power.

Since we can record signals in the voltage range -10 to 0 V and have $\times$ 60 DC am-
plification, the output voltage signals right after the diodes are in the range -0.167 to
0 V. A voltage level of -0.167 corresponds to an input power in the range -9 to -7 dBm
according to Fig. 4.14(a) which is far inside the resistive region of the diodes according to
Fig. 4.14(b). Since the square-law region for all the diodes is below -20 dBm, the output
voltage U_{out} is in the range -30 to -10 mV which after DC amplification becomes -1.8 to
-0.6 V. Therefore the recorded voltage at the ADC's should not be lower than -1.8 V, so
the square-law Schottky diode characteristics is in its desired operation range.

4.7   Characterization of the Receiver

The receiver performance can be investigated by applying a single frequency signal at the
input of the RF line and measuring the output at the 50 ADC channels. We use a setup
with a frequency multiplier, a signal generator and two variable attenuators to construct
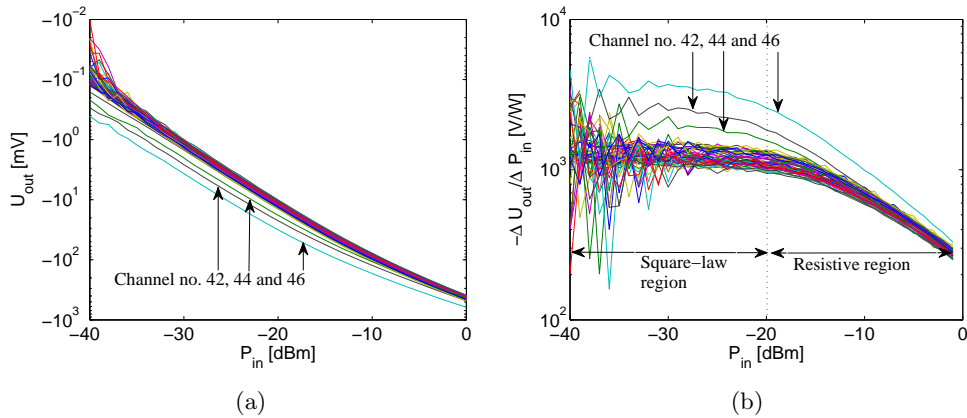
Figure 4.14: 50 square-law detector diodes terminating the 50 channels in the CTS receiver: (a) Voltage-power characteristic; (b) Slope versus input power.
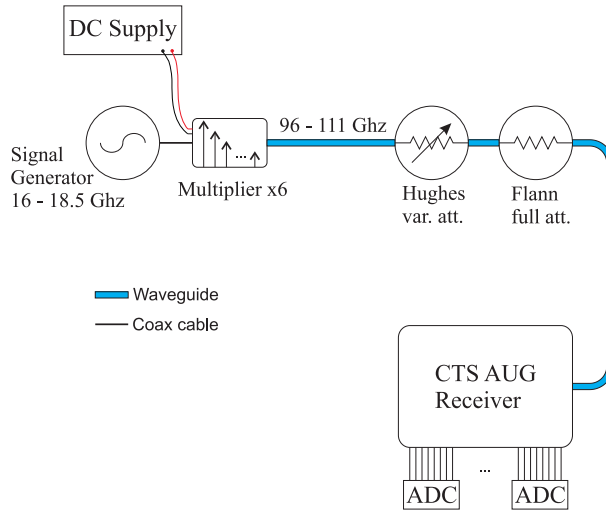
Figure 4.15: Measurement setup to determine the frequency response of the CTS receiver.

a tunable RF signal source. The frequency multiplier is driven by a signal generator used in the range from 16 to 18.5 GHz in 2.5 MHz steps. The multiplier outputs are single frequency signals in the range 96 to 111 GHz in 15 MHz steps with a total power varying from 4 to 6 dBm. The output power from the frequency multiplier is too high for testing purposes, so we need to attenuate it with at least 50 dB before it enters the RF line. For this purpose we use two attenuators, the first one (Hughes) is tunable while the second (Flann) is set to maximum attenuation. We performed separate calibrations since W-band attenuators are not necessarily linear for each frequency or setting option. The experimental setup is shown in Fig. 4.15. During the experiment we vary the signal power by using the variable attenuator (Hughes) and the frequency by tuning the signal generator, and we record the readings on the ADC's at each channel.

We show the global frequency response of the CTS receiver at one power level, here -55 dBm, and measure the ADC voltages as function of the multiplier frequency. Figures 4.16(a) and 4.16(b) present the measurements and the corresponding expectation based on the measurements of the individual components, respectively. To calculate the expectation, we disassembled the receiver and measured the transmission characteristics (S-parameters) of each component in the transmission line. The entire receiver as a unit

Figure 4.16: Voltage response to multiplier single frequency signal with a fixed power of -55 dBm. The channels containing the notch (24 and 25) are emphasized as vertical black lines and the notch filter 3 dB bandwidth limits are shown as red horizontal lines: (a) Measured frequency response using the frequency multiplier; (b) Calculated frequency response.

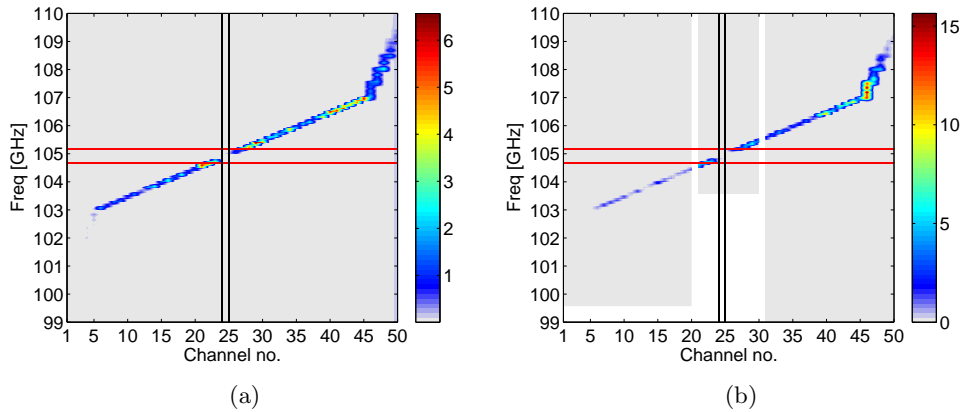was measured after it has been assembled again. Each channel only has a voltage response at its design frequency, indicating that the filters have proper attenuation outside their design passband. Different color shades along the CTS channels show that they do not have a flat frequency response, corresponding to the transfer characteristics shown in Fig. 4.13.

A second way to characterize the receiver is to increase the power and monitor the response of the 50 channels. Here we show data for a few representative channels: channels (10 , 19), (23 , 29) and (36 , 48) from filterbanks A, B and C, respectively. The channel voltages are shown as function of signal power in Fig. 4.17. The measurements are compared with the expectation based on the measurements of the individual components. We find reasonable agreement to within a factor of about 2.5.

The discrepancies in the voltage levels between the simulated and measured results, found in Fig. 4.17, indicate that we probably have standing waves arising between the different components. This is also confirmed by the fact that we mostly measure less signal compared with the simulations, which means that a part of the signal is absorbed in the system due to reflections. Another explanation is that the sensitivity of the diodes is susceptible to the environment temperature, since we know that the temperature inside the receiver box is higher than room temperature of 300 K. Since the CTS receiver has been used for plasma discharges there is some risk that the incoming radiation has been amplified to such high levels that the diode sensitivities have, possibly degraded, on a part of the available 50 channels. However, the simple method of adding S-parameters through the system, which we used for the prediction, can give us a qualitative and inexpensive picture of the receiver characteristics and is helpful when individual components of the system have to be replaced.

The sensitivity (volts per nanowatt, V/nW) of each channel as function of power can be found from the derivatives of the curves presented in Fig. 4.17. Most of the presented channels are linear and therefore have constant sensitivity as function of input power. The sensitivities of the different channels in the CTS receiver are in the range 0.5 to 3 V/nW for power inputs in the range -70 to -50 dBm.

The sensitivity [V/nW] of each channel as function of power can be found from the
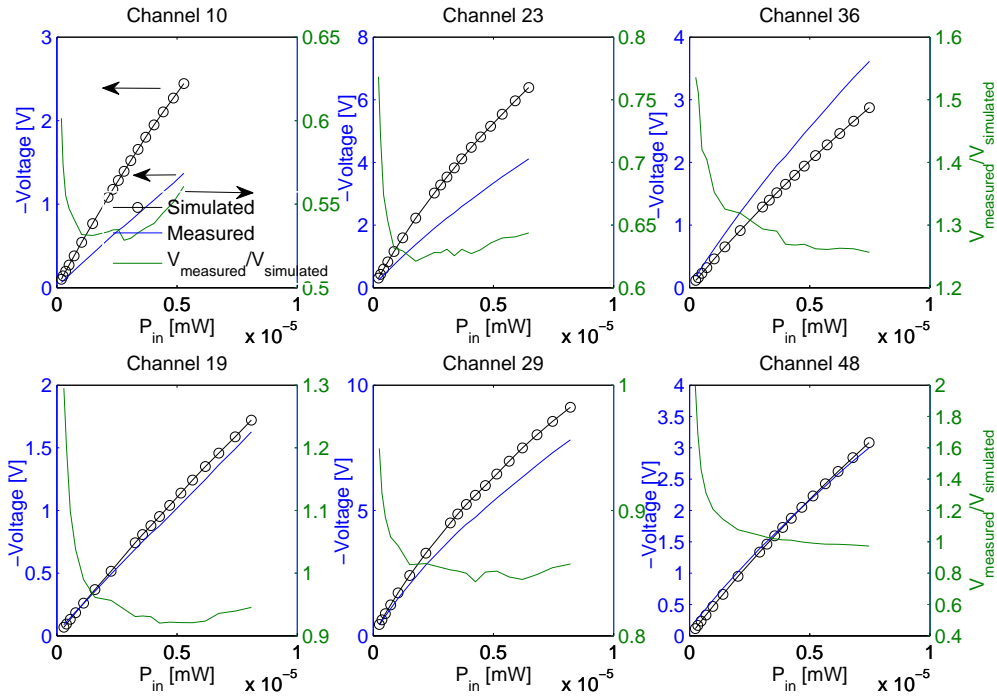
Figure 4.17: Voltage-power characteristic of a few representative receiver channels with measurements in black and calculations based on individual component measurements in blue.
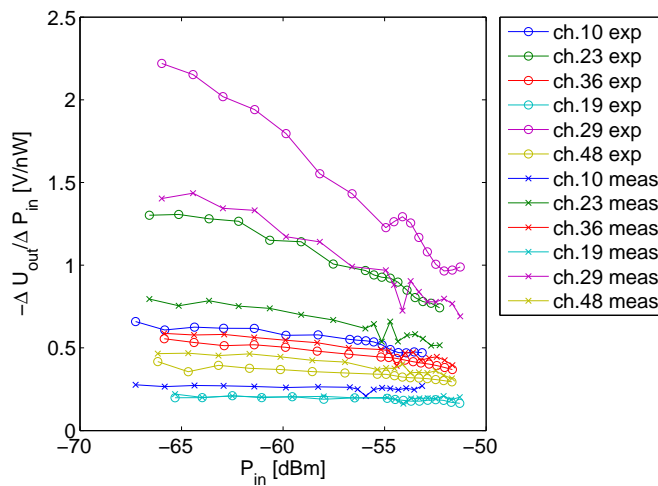

Figure 4.18: Measured and corresponding expected channel sensitivity in volts per nanowatts as function of input power.
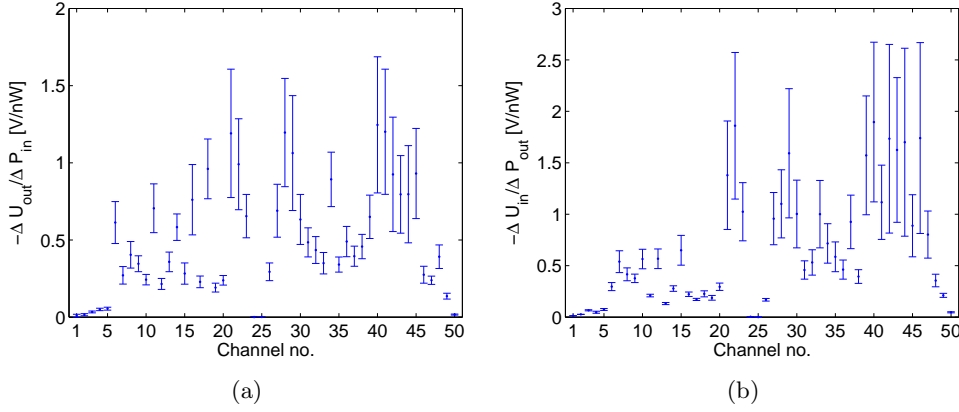
Figure 4.19: Sensitivity in volts per nanowatts at all 50 channels in the AUG CTS receiver: measured sensitivity is shown in (a) while expected sensitivity is shown in (b).

derivatives of the curves presented in Fig. 4.17. We see that most of the presented channels have rather constant sensitivity in the range from 0.25 to 1 V/nW which indicates that we operate in the square-law region of the Schottky diodes. The curves for channel 29 shows that the measured and the expected sensitivities decrease with the input power level which indicates that we operate in the resistive region of the square-law diodes. This is also the channel where the discrepancies between the measured and the expected sensitivities are highest.

We elaborate on the sensitivity calculations shown in Fig. 4.17 and determine the sensitivities of all channels for several input powers for measurements and expectations, as shown in Fig. 4.19. Channels with large attenuation such as 1 - 5 and 25 have almost no variation in the sensitivity and therefore operate in the square-law region. Channels with large amplification such as 40 - 45 have large variation in the sensitivity from 0.5 to 2.5 V/nW and therefore these channels operate in the resistive region and possibly the square-law region as well.

A different way to present a global picture of the differences between the measurements of the entire receiver and the prediction based on individual component measurements is by a definition of the voltage ratio in dB as

$$\Delta = 10 \log \left\{ \frac{V_{\text{measured}}}{V_{\text{predicted}}} \right\} \tag{4.3}$$

where V_{measured} is the voltage measured at the assembled receiver as one unit and $V_{\text{predicted}}$ is the voltage predicted due to the individual component measurements. These ratios of measured and predicted voltages in dB for our scan in frequency channels and input power are presented in Fig. 4.20. Note that the logarithm of the voltage ratio is negative for most channels and powers, which means that the measured voltage is lower than predicted. We also note that the voltage ratio Δ in each channel is approximately independent of the power but can vary from channel to channel.

4.8   IF Filters and Channel Overlap

Due to selective IF filters we are able to convert the detected voltage values to spectral power density. In other words, the IF filters help us to define the spectral components of the signal that we try to detect. In order to be sure that a voltage value from a
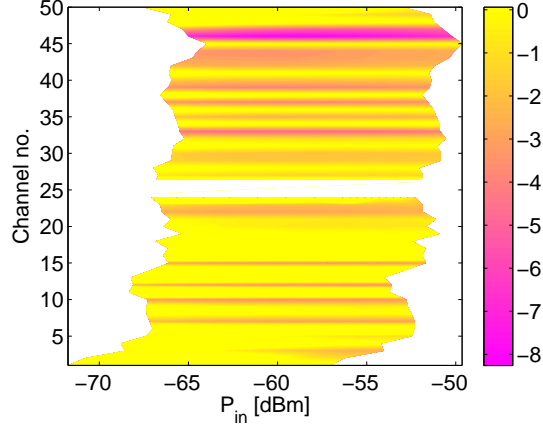
Figure 4.20: Voltage ratio Δ in dB measured at the 50 channels of the CTS AUG receiver for various power levels. Yellow colors indicates that the predicted voltage values are approximately similar to the measurements while pink indicates that the measured values are smaller compared with the expectation.

certain channel corresponds to a spectral component that is not overlapping with neighbor channels or any other channel in the receiver, the IF filters must be extremely selective, i.e. the roll-off of the IF filters should be vertical lines. This is, even in the filter theory, not possible to realize. Therefore it is beneficial for us to investigate how IF filters impact on quality of the detected spectral power density.

In fusion plasma microwave diagnostics we usually assume that the IF bandpass filters are perfectly selective in order to calculate the spectral power density. In practice, this is not the case. The roll-off of the IF filters is in the range 0.1-0.15 dB/MHz for the broadband channels and 0.5-1.0 dB/MHz for the narrowband channels. The filters have relatively poor roll-off attenuation taken into account that the 3 dB points are very close to each other along the frequency axis and sometimes even overlap (which is not the same as channel overlap defined later). Existence of finite roll-off attenuation and neighbor channels that overlap have significant impact on estimation of the spectral power density.

Let us first investigate roll-off attenuation in a radiometer channel, as inspired by Fig. 4.21(b). The most common expression to determine the power P_1 detected in an IF channel is

$$P_1 = k_B \cdot BW_{3dB} \cdot G_c \cdot (T_A + T_N) \qquad \text{(Watts)}, \qquad (4.4)$$

where k_B is the Boltzmann's constant, BW_{3dB} is the 3 dB bandwidth of the IF channel and G_c is the corresponding gain from the horn to the output port of the IF filter, T_A is the antenna temperature at the horn while T_N is the noise temperature of the receiver. The power P_1 is thereby a function of temperature T, bandwidth BW_{3dB}, and gain G_c. The Eq. (4.4) is the most simplified case since we assume that the receiver transfer function from the horn down to the output port of the IF channel is a perfect rectangular function with height G_c and width BW_{3dB}. Taken into account variations in the gain and the attenuation roll-off the power P_2 detected in an IF channel is more correctly written as

$$P_2 = k_B \cdot (T_A + T_N) \cdot \int G(f) df \qquad \text{(Watts)}, \qquad (4.5)$$

This scenario is presented in Fig. (4.21(b)) where blue color presents area of a perfect rectangular gain function and blue plus yellow colors present the actual behavior of the

transfer function with gain variation and attenuation roll-off. Figure 4.22 shows examples on measured gain functions versus frequency for filterbanks A and C, respectively, where large channel overlaps supported by attenuation roll-of are clearly seen. By dividing the Eq. 4.4 with Eq. (4.5) we get

$$\text{Channel ratio} = \frac{P_2 - P_1}{P_2} = 1 - \frac{BW_{3dB} \cdot G_c}{\int G(f)\mathrm{d}f}. \tag{4.6}$$

Applying all the transfer function measurements of the CTS radiometer into Eq. (4.6) we get an output shown as the red curve in Fig. 4.23. The red curve clearly shows that simple assumption from Eq. (4.4) will underestimate the total integrated power in each channel by 10 - 20%. Converting this result into the terms of a perfect rectangular function with height G_c and width BW_{3dB}, we can state that the *absolute* 3 dB bandwidth is a bit broader than BW_{3dB} defined in Eq. 4.4.

Since we have measured all the IF filters we can also determine the overlap area of a channel with its two nearest neighbor channels. Since we do not have theoretical gain transfer functions available we need to use logical statements in order to find overlap areas that are common to neighbor channels and the channel in consideration as shown in Fig. 4.21(a). Caution needs to be taken during overlap area calculation since for instance channels 1 and 3 may have a large overlap that is placed inside channel 2. Therefore all the overlap calculations are divided into the region below the point where channel 1 and 3 cross and the region after channel 1 and 3 cross. This procedure is repeated exactly the same way for channels 2, 3, and 4 etc. with the channel overlap ratio presented as the blue curve in Fig. 4.23. The information contained in the blue curve can be interpreted as follows; values around zero indicate channels that are spectrally divided very well, while values around one indicate channels that are poorly spectrally divided. In our case we have a surprising result showing us in average around 50% of overlap signal across all channels. In other words, 50% of the signal we detect in one channel can also be found in the two neighbor channels, i.e. the channels that are close to each other are also strongly correlated. The worst case scenario with overlap larger than 80 % is seen in channels 6 and 45, and naturally in channels 24 and 25 which correspond to notch filter channels. Thereby, channels such as 6 and 45 have very little information that are unique and not shown in any neighbor channels. Poor spectral selection of the IF filters increase the cost of the receiver and at the same time it limits the dynamic resolution of the spectral power density because channel overlap areas are too large. Notice that the knowledge of channel overlap ratio does not necessarily uncover more information on attenuation roll-off or gain variation in the channels, for that we need to have transfer function versus frequency available.

4.9   Conclusions

The individual components of the CTS receiver at ASDEX Upgrade and their performance characteristics are presented. The receiver uses a heterodyne scheme, i.e. converts signals in the W-band down to IF signals in a down-mixing stage. We find losses in the range 10 to 26 dB in the receiver RF line which is sometimes inevitable due to filtering requirements. The mixer has conversion losses in the range from 5 to 6 dB which adds to the receiver noise figure. The down-converted IF signal is amplified and divided into three bands using three bandpass filters in the triband box. There are two further amplifiers in each branch of the triband box, making it seven amplifiers in total. Thereby every branch has three amplifiers in cascade of which the first one is common for all three branches.

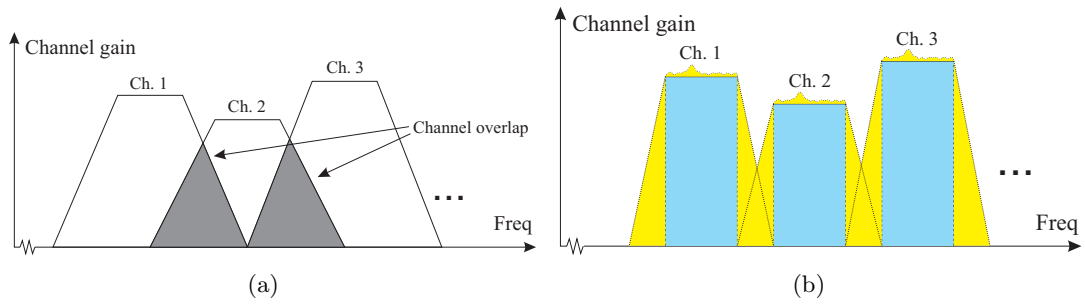**Figure 4.21:** Overlap area between the neighbor channels is shown in (a) while simple integration covering spectrum defined by 3 dB points is shown in (b).
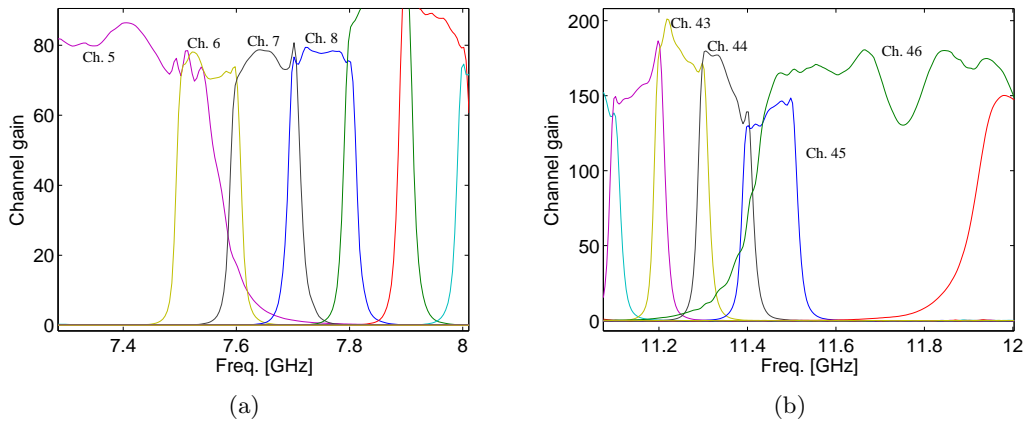

Figure 4.22: Gain for channels in the filterbank A shown in (a) while gain for channels in the filterbank C shown in (b). The curves for channels presented in both graphs are linear in scale and calculated on basis of voltage gain.
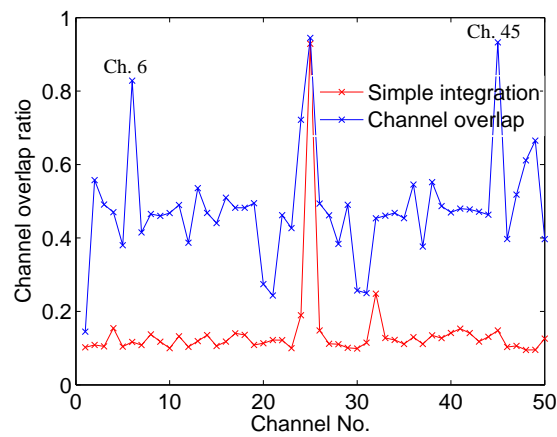

Figure 4.23: Channel overlap ratio.

The amplifiers have gain in the range from 24 to 46 dB and power output at 1 dB gain compression from 15 to 27 dBm. The IF filterbanks A, B and C containing 50 bandpass filters will assure passage of signals in the frequency range from 4.5 to 14.5 GHz, each channel only in its design frequency bandwidth of typically 100 MHz. Schottky square-law detector diodes are used to convert the IF signal down to DC voltage levels which are acquired by 24 bit acquisition cards. They operate in the square-law region for input powers up to -20 dBm. Their sensitivity in this region varies from 900 to 1300 V/W. The total receiver noise figure is frequency dependent and in the range between 11 and 20 dB except for in the notch filter channels. The largest contributions to the noise figure are the losses in the RF-line and the mixer conversion loss.

The characterization of the individual components allows us to calculate the receiver response to RF signals at various frequencies. This expectation of the receiver response is compared with the measured receiver response. To measure the entire receiver response, we use a signal generator and a frequency multiplier as a tunable single frequency signal source and a variable attenuator to control the output power. A scan with varying RF frequency and power has been performed. The measurement of the entire receiver response agrees reasonably well with the expectation based on the individual component measurements within a factor of about 2.5. In both measurement methods we find that the voltage response across channels is not flat and can vary by several volts. Generation of harmonics in the mixer or amplifiers and radiation leakage are well suppressed in the present CTS receiver design.

We have calculated the sensitivity as function of input power for all 50 channels for measurements as well as for the expectations. For the channels with low amplification the sensitivity is relatively constant. For most of the channels we find that the sensitivity is in the range from 0.5 to 3 V/nW for the measurements and expectations. Furthermore, we have investigated the influence of the finite filter roll-off attenuation on the power detected at the channels. From the system point of view, we find it acceptable to use individual component measurements to predict the overall performance of the CTS AUG receiver.

Chapter 5

Notch Filter Design

5.1 Short background and introduction

Due to large stray radiation and frequency drift of the probing beam we find it necessary to design and build these filters in our lab facilities. We have made several designs on notch filters based on two different approaches. Both approaches are based on the same technology where we use cylindrical stubs as resonators connected to the main waveguide by narrow apertures. The difference in these two approaches is the orientation of the resonators relative to the main waveguide.

Since the Danish CTS group is abundantly involved in the campaigns at ASDEX Upgrade five notch filters have been designed to support the ongoing experimental work. Two notch filters with 105 GHz center frequency, more than 20 GHz passband coverage, and 1 GHz rejection bandwidth have been constructed. One of the filters is based on a rectangular waveguide with cylindrical cavities coupled by narrow iris gaps, i.e. small elongated holes of negligible thickness. The other filter is based on approach by aperture coupling using thin slits. Furthermore, a notch filter for the ECE group at ASDEX Upgrade, based on aperture coupling using thin slits, 140 GHz center frequency, and 1 GHz rejection bandwidth has been designed and tested. The two last notch filters with 105 GHz center frequency and only 100 MHz rejection bandwidth were designed and tested for the newly installed CTS receiver at ASDEX Upgrade.

We use numerical simulations to study the sensitivity of the notch filter performance to changes in geometry and in material conductivity. The constructed filters are tested successfully using a self-made measurement setup or a commercial vector network analyzer monitoring bandwidths from 10 and up to 20 GHz. The typical insertion loss in the passband is below 1.5 dB while the attenuation in the stopband is varying from 40 dB and up to 90 dB, depending on the approach and number of the resonators used. Extensive aspects on coupled cavity resonators are presented in [11, 65, 51].

5.2 105 GHz notch filter for CTS

In magnetic confinement devices, such as tokamaks or stellarators, mm-wave notch filters are used to protect diagnostic instruments from gyrotron stray radiation. Typical mm-wave diagnostics are ECE spectroscopy, reflectometry, and CTS [48]. Gyrotrons produce high power mm-waves and are used for electron cyclotron resonance heating (ECRH) and current drive (ECCD) [89, 88], for mitigation of tearing modes [91], and as a probing radiation source in CTS experiments [53, 54, 70]. Notch filters can make mm-wave plasma diagnostics compatible to plasma experiments with gyrotron operation.

The tokamak ASDEX Upgrade is equipped with dual frequency 1 MW gyrotrons [88, 89]. Operation at 140 GHz is used for ECRH and ECCD [89, 88]; operation at 105 GHz is used for CTS experiments [53, 54, 70]. The velocity distribution function of fast ions [70, 6, 57, 58] and the ion temperature [3] have been measured on various magnetic confinement devices using CTS. Important prerequisites for CTS measurement of the fuel ion ratio have been demonstrated [40, 76], and it may also be possible to infer the ion rotation and the ion densities [40].

The requirement for the notch filter rejection bandwidth depends on whether stray radiation from a single gyrotron or from many gyrotrons has to be blocked. For a single gyrotron, a rejection bandwidth of 130 to 200 MHz centered at the nominal gyrotron frequency is sufficient to accommodate gyrotron chirp [53]. CTS experiments require only a single gyrotron. The front-end CTS receiver has two notch filters in series which strongly attenuate the gyrotron stray radiation. The rejection bandwidth has to be sufficiently wide just to cover the gyrotron beam, but not wider than that since otherwise valuable information about the distribution of bulk ions would be lost. Depending on scattering geometry and bulk ion temperature, the width of the measured bulk ion CTS spectra can be as narrow as ± a few hundred MHz. The CTS passband required for the notch filter is ± 5 GHz wide, so as to measure fast deuterons with energies up to 500 keV [53] expected in plasmas at ASDEX Upgrade.

If many gyrotrons are used, typical for ECRH or ECCD, the notch filter rejection bandwidth has to be wider due to slightly different center frequencies of the gyrotrons (from 500 MHz to 1 GHz [53, 23, 25]). A notch filter with a relatively broad stopband has been presented [23]. The ECE spectroscopy system at ASDEX Upgrade requires a notch filter with rejection depth of 60 dB and notch bandwidth of $\sim$1 GHz since several gyrotrons are used simultaneously [88]. Additionally, these notch filters should have a broad passband to cover the ECE band, they should have a low, frequency independent insertion loss, and the portion of reflected power should be low. The ECE spectroscopy system at ASDEX Upgrade requires a passband of ±9 GHz in order to cover the complete plasma ECE range.

Diagnostics using mm-waves can well be used in the strongly radiative environment of future plasma confinement devices with fusion processes [69], and gyrotrons are also foreseen for such devices. Several gyrotrons are foreseen to be installed on ITER with frequencies of 170 GHz for ECRH and ECCD [64, 38], of 120 GHz for machine start-up [12, 22] and of 60 GHz for the CTS diagnostic [39, 46, 67, 68]. ITER will most probably be equipped with reflectometry diagnostic [86, 63] and ECE spectrometry [85, 14]. So notch filters will be necessary for ITER. Several options of notch filters for ITER are available [93]. F-band notch filters with notch frequencies up to 140 GHz and up to 100 dB rejection and passband coverage of several GHz have been designed [23, 20, 26, 15, 43, 16]. Waveguide notch filters with a center frequency below 100 GHz have also been presented [9]. Notch filters for higher frequencies are more difficult to construct as the dimensions of the filter become so small that precise machining becomes difficult [93]. However, one can use quasi-optical resonance notch filters [27, 17, 74] or the absorption lines of molecules [92, 93].

To extract satisfactory diagnostic data, the bandwidth of the passband on each side of the notch has to be adequate where at the same time insertion loss (IL) should be as small as possible and possess flat frequency response. In addition, the larger the passband coverage, the more likely the same notch filter can be used for several diagnostics reducing the overall system cost. Due to their robustness to high radiative and neutron flux environment, mm-wave based diagnostics will play a key role in future burning plasma
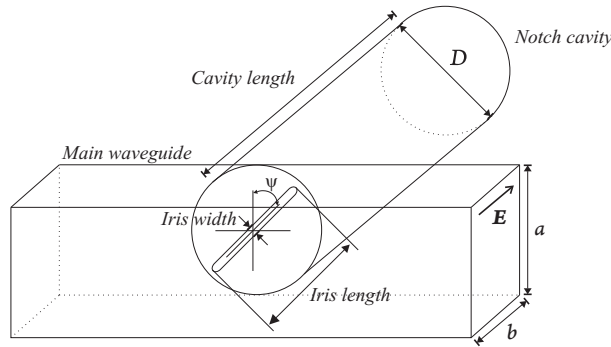
Figure 5.1: T-junction aperture coupling using iris and horizontal cavity scheme. If we choose $\psi = 90°$, transverse magnetic (TM) modes will be dominant inside the resonant cavity.

devices [69]. Hence high performing notch filters will play an important role in a strongly radiative environment. In this section we present a design of a compact and sensitive F-band notch filter with 1 GHz rejection bandwidth and a possibility of tuning the center frequency $\pm 2\%$. We measure the spectral response of the notch filter and compare it with numerical simulation. Additionally, we assess the sensitivity to changes in physical parameters and in material conductivity by 3-D simulations in Computer Simulation Technology (CST).

5.2.1   Iris coupled T-junction in a circular waveguide

If a waveguide with uniform cross-section is terminated at both ends by metal planes perpendicular to the axis of the guide and if the guide length is equal to a full number of half wavelengths, $\lambda_g/2$ where λ_g is defined as the distance between two equal phase planes along the waveguide, electromagnetic fields can resonate in the guide. Such a waveguide can be a cylindrical cavity and is used here to form a tunable notch filter. Requirements for the notch filter are: 3 dB rejection bandwidth around 300 MHz, center frequency $f_0 \sim 105$ GHz, and passband of at least 18 GHz centered at f_0. The 3 dB rejection bandwidth BW_{3dB} is defined here as a bandwidth between the two 3 dB points of the insertion loss. We require 300 MHz between the two 3 dB points due to gyrotron operational bandwidth of around 100 MHz (see Fig. 2.10) that must be attenuated as much as possible. A way to design such a notch filter is to use a symmetrical right-angle T-type junction of a rectangular and a circular guide coupled by a small elliptical aperture (iris) in a metallic wall of negligible thickness [51] as shown in Fig. 5.1. A great benefit of an iris design is the simple cavity adjustment with only a single tuning screw per cavity. The major axis of the elliptical aperture forms the angle ψ with respect to the vertical axis. The angle ψ is restricted to 0° to ensure good coupling to all the TE_{nml} modes in a cylindrical cavity and among these the dominant TE_{11} mode. The subscript n refers to the number of circumferential (ϕ) variations, m refers to the number of radial (ρ) variations, and l refers to the full number of half wavelengths along the z axis according to the cylindrical coordinate system (ρ, ϕ, z). Sometimes we omit subscript l referring to a TE_{nm} mode with any integer of half wavelengths along the z axis. The dominant mode has optimum passband coverage and relatively low loss compared with higher order modes.

In the main guide the TE_{10} mode exists and is the dominant mode for the rectangular waveguide. From the previous discussion we know that an iris wall has ideally no thickness,
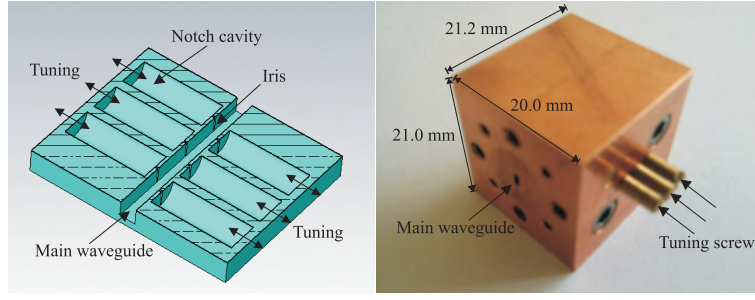
Figure 5.2: Left: planar cut of the notch filter. Right: the constructed notch filter with tuning screws. The adjustment screws are not depicted in the sketch.

but we choose an aperture in the metallic wall with 0.2 mm thickness because smaller sizes cannot be realized. The finite iris thickness introduces only a slight translation in frequency characteristics. The effect of finite iris thickness is small because 0.2 mm is much smaller than the vacuum wavelength $\lambda_0 = c/f_0 = 2.86$ mm. The cut-off wavelength λ_c determines the lowest frequency in a waveguide. For the main guide $\lambda_c = 2a = 4.06$ mm, where $a = 2.03$ mm is the broad side of the guide. A waveguide with circular cross-section has a cut-off wavelength $\lambda_{c,nm} = \pi D/p'_{nm}$ where $D = 2$ mm is the cavity diameter and p'_{nm} is the m'th root of the derivative of first order Bessel function $J'_n(p'_{nm}) = 0$. For the TE_{11l} mode we find the cut-off wavelength $\lambda_{c,11} = \pi \cdot 2/1.841 = 3.41$ mm, i.e. $\lambda_c > \lambda_0$ as required. The desirable distance between two resonators is an odd number of quarter wavelengths, so the notches can be tuned independently of each other:

$$\Delta l = \frac{\lambda_g}{4}\left(1 + 2N\right) \quad \text{where} \quad \lambda_g = \frac{\lambda_0}{\sqrt{1 - \left(\frac{\lambda_0}{\lambda_c}\right)^2}}, \tag{5.1}$$

and $N = \{0, 1, 2 \ldots\}$. The wavelength for the main guide is $\lambda_g = 4.0$ mm and ideally $N = 0$; we get $\Delta l = 1.0$ mm. Setting $N = 0$ will give us smaller device but the Δl value will leave no space for the tuning screw thread. The simulations have shown that a slightly higher value for Δl ($\Delta l = 1.3$ mm) will have a negligible impact on the notch shape since the resonance frequencies are not affected by the distance Δl but only by the cavity length d and by the diameter D. The constructed notch filter and the 3-D graphical sketch are shown in Fig. 5.2.

Figure 5.3 shows the first four transverse electric (TE) modes appearing in a cylindrical cavity resonator: TE_{11l}, TE_{21l}, TE_{01l}, and TE_{31l}. Each mode is plotted with the first three resonating lengths $d = l\lambda_g/2$ where $l = \{1, 2, 3\}$. Using Eq. (5.1) and assuming cavity modes TE_{11l} with $\lambda_c = 3.41$ mm we find that $\lambda_g = 5.2$ mm where possible resonator lengths are $d = \{2.6, 5.2, 7.8 \ldots\}$ mm. The distance between the curves along the vertical direction shows the distribution of resonance frequencies when D/d is constant. The product of resonance frequency and cavity diameter of our notch filter is $f_r D = 21$ [GHz-cm] resulting in $D/d \sim 0.77$ for the TE_{111} mode. The calculated cavity length becomes $d = 2.6$ mm. The chosen point of resonance can vary ± 10 GHz without intercepting another resonance line which means there are no other notches within this band. This is the main reason why we operate the notch filter using the dominant TE_{111} mode.

The quality factor Q for, among others, TE_{111} mode is depicted in Fig. (a) [51]. The value of Q is normalized with skin depth divided by free space wavelength, for copper given as $\sigma_s/\lambda_0 = 6.95 \cdot 10^{-6}\sqrt{f_{GHz}}$. Since we have that $2a/d \sim 0.77$ and $\sigma_s/\lambda_0 \sim 0.27$ for the TE_{111} mode, than at the resonance frequency of 105 GHz the quality factor becomes
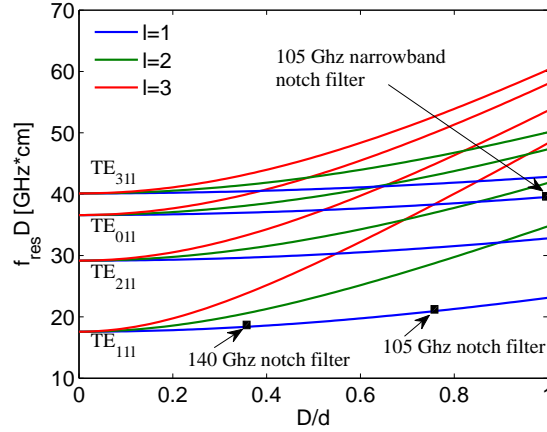
Figure 5.3: TE mode chart for the first four modes using a cylindrical cavity resonator. The mode characteristics become straight lines if one plots $[f_r D]^2$ versus $[D/d]^2$. The small rectangles show the points of resonances for the notch filters designed.

	Main waveguide	Resonator cavity
Mode	TE_{011}	TE_{111}
Vacuum λ_0 [mm]	2.86	2.86
Cut-off λ_c [mm]	4.06	3.41
Waveguide λ_g [mm]	4	5.2

Table 5.1: Characteristic λ values for the main rectangular waveguide and the cylindrical resonator waveguide.

$Q \sim 3800$.

5.2.2 Experimental and numerical methods

The notch filter is measured using a broadband Anritsu millimeter wave vector network analyzer (VNA) ME7808B with a calibrated bandwidth of 20 GHz. A pair of waveguide tapers has been used to adapt the WR-8 notch filter ports to the WR-10 VNA ports. The port 1 test power is approximately +2 dBm, and the output dynamic range is approximately 60 dB (for a sweep of 2 s) which is sufficient for us to localize the notches.

In the simulations we solve Maxwell's equations and boundary conditions which describe the electromagnetic field distribution inside a waveguide and resonator cavities. If we know the fields existing in the structure, we can uniquely determine the scattering parameters. CST Microwave Studio with a real time domain simulator based on the finite element method is used to characterize the filters. For the simulation we assume air as medium where the fields can exist; the notch filter body is chosen to be copper. The notch filter is excited using waveguide ports at the ends of the main rectangular guide.

5.2.3 Measured and computed notch filter performance

The center frequencies of the measured and the simulated notch filters, shown in Fig. 5.5, coincide as expected. The measured notch filter has a much wider 3 dB rejection bandwidth, approximately 1.8 GHz, compared with the simulated value of approximately 380 MHz. The quality factor, or Q factor, with $Q \sim \frac{f_0}{BW_{3dB}}$ is then lower for the constructed filter by a factor 5 compared with the simulated filter. It is not obvious to explain
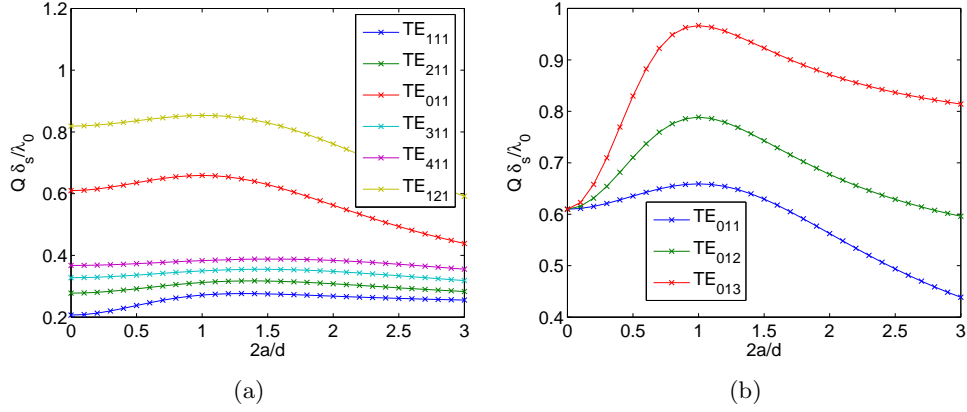
(a)   (b)

Figure 5.4: Quality factor Q for the few selected TE modes in cavities with circular cross section where $a = D/2$ is the radius: (a) Normalized Q assuming $l = 1$, where σ_s is the skin depth; (b) Normalized Q for TE_{01} modes. We see that assumption $2a/d \approx 1$ gives optimum Q for all TE_{01} modes.
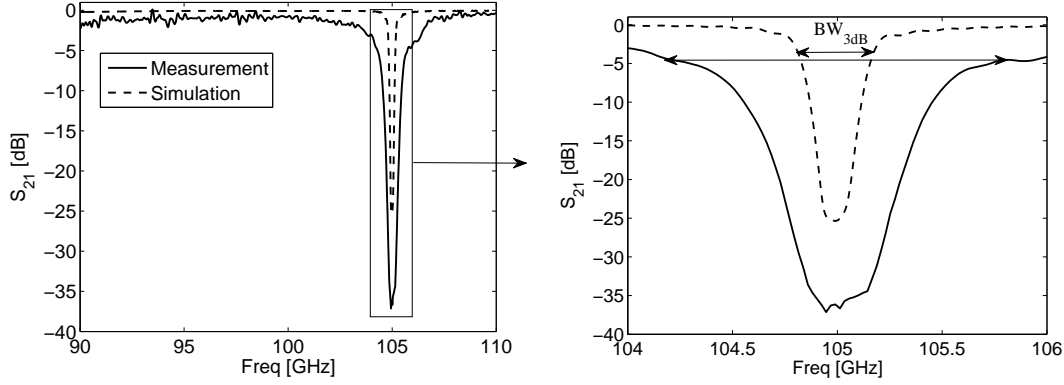

Figure 5.5: A wide band and a narrow frequency band with a zoom close to the notch. The two lines on the right figure show 3 dB bandwidth, BW_{3dB} with respect to carrier, for the simulated and constructed notch filter.

this discrepancy in the bandwidth from the electromagnetic point of view. However, we know that the best way to couple to a cylindrical resonator is by directing the E-field in the circumferential direction in order to reduce the current component in the longitudinal direction. The way we couple to the resonator shown in Fig. 5.1 is far from ideal and therefore we most probably have large current components in the longitudinal direction. The instabilities in the mechanics such as loose tuning screws or tuning plates, low torque on assembly screws, etc., can corrupt the electrical response of the resonators and possibly change the 3-dB bandwidth considerably.

Figure 5.6 (left) shows the spectral position of the modes in a 45 GHz bandwidth range. The cutoff frequency is located around 73 GHz due to the rectangular waveguide dimensions (WR-8). Below the cut-off no wave can propagate through the filter. A spurious mode is observed using the geometry defined by Fig. 5.1. This mode is not cylindrical since it exists below the dominant TE_{11} mode. Further analysis have shown that this spurious mode is independent of the circular resonator length (as presumed) while the mode frequency drifts by several gigahertz when the ratio between iris length and the cavity diameter is perturbed. Simulations have demonstrated that if this ratio is approximately
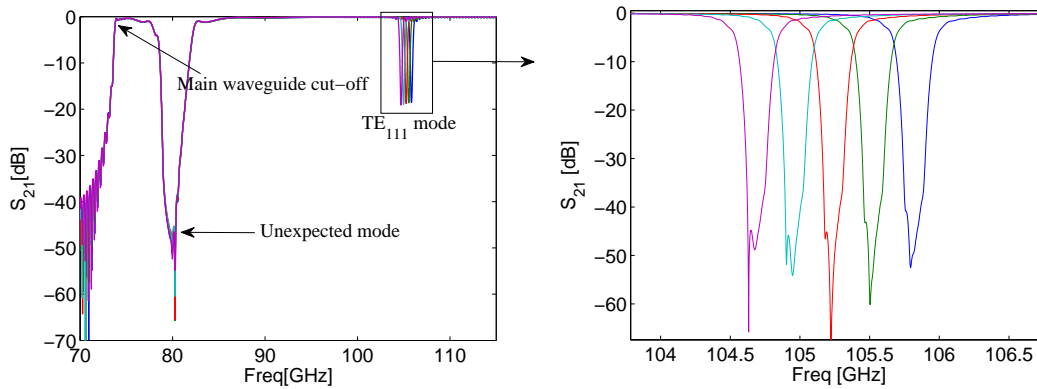
Figure 5.6: S-parameter narrowband simulation showing 5 different cavity lengths.

one, the spurious mode is very close to the cut-off region; if the ratio is deviating from one, the spurious mode moves to the right in the spectrum. Furthermore, simulations at frequencies where the spurious mode appears show dominant surface current densities at the top and the bottom of the iris.

The frequency resolution in Fig. 5.6 (left) is not sufficient to resolve the spectral region centered about the notch at 105 GHz, and the notch depth cannot be obtained with this coarse resolution. We increase the frequency resolution in Fig. 5.6 (right) by a factor of 5 where the frequency step is much smaller than the 3 dB bandwidth. In addition $\lambda_{mesh} \ll \lambda_g$ is hard to keep when simulating strongly resonating structures (such as a filter) due to relatively long solving time. The measurements have demonstrated that the notch depth is strongly dependent on the attachment between the tuning screws and the filter body and can vary up to ± 10 dB when shifting the center frequency by ± 2 %. The filter Q factor can be degraded, so mechanical stability of the tuning screws will increase the notch depth with less variation during adjustment.

5.2.4 Sensitivity study of the computed results

In this section we address the sensitivity of the computed results to changes in physical and numerical parameters. We consider first how the results change when the mesh is refined. Second, we consider how the results depend on the key geometry parameters. The sensitivity to all parameters, physical and numerical, has a bearing on the accuracy of the comparison between the computed and measured results. Figure 5.7 shows the notch frequency, the 3 dB bandwidth, and the shape factor, $\text{BW}_{20dB}/\text{BW}_{3dB}$, as a function of lines per wavelength where $L/\lambda_0=20$ corresponds to 1.4 million meshcells. The shape factor measures how efficient the filter is in the rejection band. For instance if the 3 dB rejection bandwidth is 1 GHz and the shape factor is 0.8, then we can be sure that a bandwidth of 800 MHz will reject at least 20 dB of the input signal centered around f_0. The center frequency changes by few tens of MHz if increasingly finer meshes are used, the 3 dB bandwidth settles in the range from 340 to 370 MHz and the shape factor from 0.51 to 0.55. These ranges show how accurate the parameters could be determined by the simulation, given the physical parameters were set correctly. But the results are highly sensitive to the physical parameters, and so the grid accuracy gives only an incomplete picture. We will now demonstrate the sensitivity of the results to physical or geometrical parameters: the cavity length, the iris width, the iris length, and lastly the material choice.
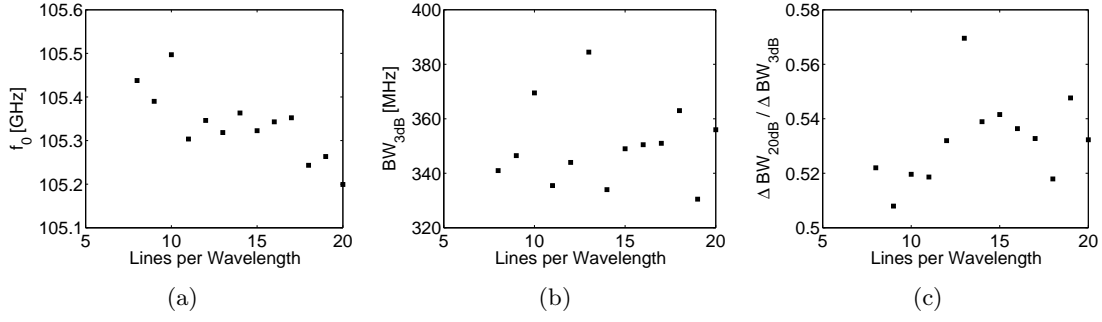
Figure 5.7: Convergence study of the filter parameters plotted as functions of lines per wavelength (L/λ_0): (a) Center frequency; (b) 3 dB bandwidth; (c) shape factor.
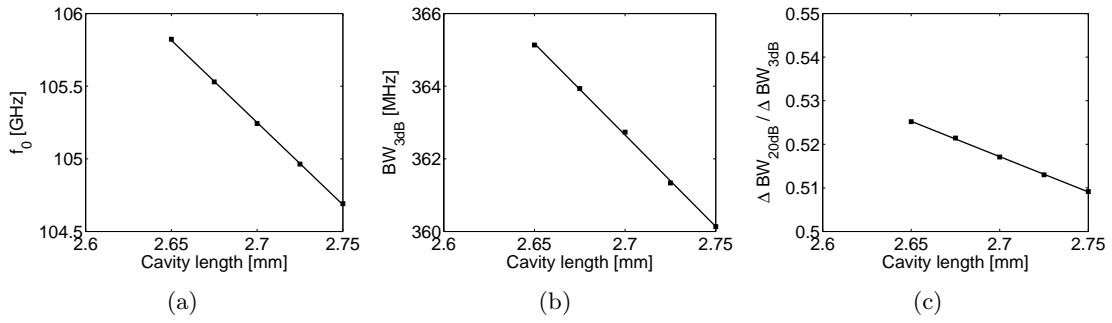

Figure 5.8: Sensitivity of the center frequency f_0, the 3 dB bandwidth, and the shape factor to changes in the cavity length, see Fig. 5.1. Symbols: simulations; line: least squares fit: (a) Center frequency; (b) 3 dB bandwidth; (c) shape factor.

The new design for the F-band notch filter is found to differ from the approach presented in [23, 25]. The center frequency is nearly eight times more sensitive to change in the cavity length with the gradient of -11.32 GHz/mm as seen in the upper graph in Fig. 5.8. Higher sensitivity enhances the possibility to move the resonance frequencies up or down making the notch filter more attractive for other experiments. The 3 dB rejection bandwidth is less sensitive compared with the design in [23], and has a slope of -50 MHz/mm. The shape factor has values in the range from 0.51 to 0.53, which are acceptable. The sensitivity analysis results are reported in Tab. 5.2.

The six cavities have the same length in the simulations. The initial cavity lengths d typed in the simulator environment are calculated by hand using theory described in section 5.2.1. The length between two cavities, Δl, is calculated from the theory in section 5.2.1 and is not optimized in the simulator. Any resonances that appear in the range 90 to 140 GHz are due to cylindrical cavities only. The filter coupling geometry can help us to excite certain modes better than others, but shifting in frequency or creating and destroying modes is not possible by changing coupling geometry.

The iris width (see Fig. 5.1) has relatively small impact on the slope of the center frequency but high impact on the 3 dB bandwidth as seen from Fig. 5.9. The shape factor gets even better with the iris width but at the same time the 3 dB bandwidth gets larger. The key values for the iris width are reported in table 5.2.

The iris length is interesting since it shows non-linear dependence of the 3 dB bandwidth as shown in Fig. 5.10. The iris length must be kept at approximately 1.9 mm in order to keep the rejection bandwidth narrow. For this iris length, the sensitivity of the
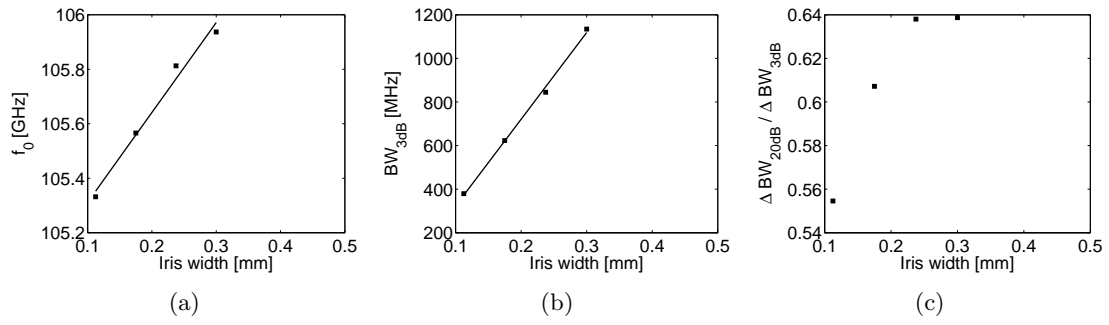
Figure 5.9: Sensitivity of the center frequency f_0, the 3 dB rejection bandwidth, and the shape factor to changes in the iris width. Symbols: simulations; line: least squares fit: (a) Center frequency; (b) 3 dB bandwidth; (c) shape factor.
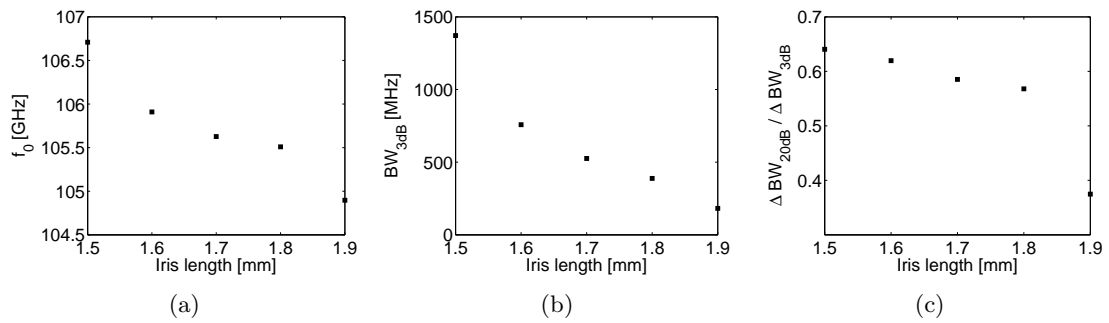

Figure 5.10: Sensitivity of the center frequency f_0, the 3 dB bandwidth, and the shape factor to changes in the iris length. Symbols: simulations; line: least squares fit: (a) Center frequency; (b) 3 dB bandwidth; (c) shape factor.

3 dB rejection bandwidth with respect to changes of the iris length is small as can be seen from the curve gradient. Small imperfections in the machining have a small effect on the rejection width. For the calculated points that are well distributed along a straight line the least squares method is used to determine the slope.

If we choose to set the iris width to 0.2 mm, the 3 dB rejection bandwidth will, according to the simulations, get 162 MHz broader. The 3 dB rejection bandwidth is less sensitive to the iris width (3.98 GHz/mm) compared with the iris length (-6.13 GHz/mm) as shown in table 5.2. The iris length should not be short compared with the cavity diameter, since otherwise the 3 dB rejection bandwidth will increase. The lowest rejection bandwidth is achieved if the iris length is comparable to the cavity diameter.

The material choice is an important factor when trying to minimize conductor loss.

	Center freq. [GHz/mm]	3 dB bandwidth [GHz/mm]	Shape factor [mm^{-1}]
Cavity length	**-11.32**	**-0.05**	**-0.16**
Iris length	-8.0	-6.13	-1.93
Iris width	**3.3**	**3.98**	0.84

Table 5.2: Sensitivity analysis investigation: impact on key characterization parameters by varying the design lengths (filter geometry). The bold numbers are slopes fitted using least squares method while the others are determined by the largest absolute gradient in the simulation range.
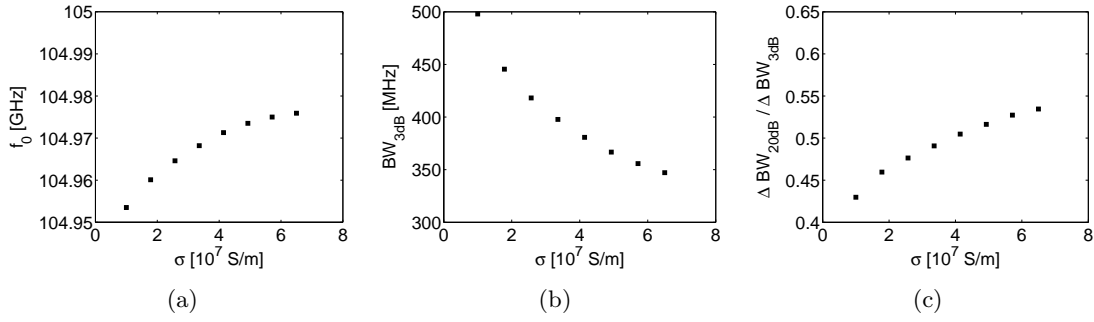
Figure 5.11: Center frequency f_0, 3 dB bandwidth, and shape factor, respectively, are plotted versus material conductivity: (a) Center frequency; (b) 3 dB bandwidth; (c) shape factor.

The insertion loss curve shifts down in level when the conductor loss increases causing broader 3 dB rejection bandwidth, which is not what we aim for. A clear difference of few dBs among conductors appears at the passband shoulders as seen in Fig. 5.11. The lower graphs in Fig. 5.11 have opposite slopes where the 3 dB bandwidth decreases while the shape factor increases with conductivity of the filter body. This implies that the quality factor Q of the resonators improves as expected from theory. This phenomenon is not observed for geometrical parameters such as cavity length and iris width and length, meaning that there is always a trade-off among geometrical parameters in order to achieve the optimum filter characteristics.

Commonly either copper (σ=5.96 · 10^7 S/m) or silver-coating (σ=6.3 · 10^7 S/m) are used as material for frequencies above 110 GHz. We use copper for construction of the filter body and brass for the tuning screws. Brass is a harder metal than copper and thereby useful for the mechanical parts that can wear out quickly, such as tuning screws.

5.2.5   Discussion

A notch filter using T-junction iris coupling (Fig. 5.1), 20 GHz passband coverage, and 1.8 GHz rejection bandwidth has been presented fulfilling the design requirements mentioned in the beginning of section 5.2.1. The key filter parameters such as center frequency f_0, 3 dB rejection bandwidth BW_{3dB}, and shape factor were investigated by adjusting the filter geometry slightly. The center frequency of the filter is found to be sensitive to the cavity length, which is beneficial for the dynamic notch shifting across the spectrum.

The filter parameters are sensitive to small inaccuracies in the milling process or to cavity tuning. From the simulation data compiled in table 5.2 we see that the filter geometry have impact on the filter parameters. How crucial these influences are depends on the filter requirements. A notch filter design should have a low sensitivity to geometrical changes in its center frequency, 3 dB bandwidth, and shape factor. It is clear from the simulations that the iris width is the most critical parameter for the 3 dB rejection bandwidth and thereby also the shape factor.

Changes in the cavity length turned out to be linear in center frequency f_0, 3 dB rejection bandwidth and shape factor. The notch frequency shift of -11.32 GHz per mm is a sensitive response, but flexibility in the dynamic range where to place the notch frequency is large. Tuning the notch filter few GHz up or down is not considered to be a problem in terms of the passband coverage and 3 dB bandwidth. However, the notch depth can vary ±10 dB due to the mechanical imperfections.

A way to improve the notch filter design is to enlarge the cavity diameter D exciting the degenerate TE_{01} mode. Attenuation coefficients of the circular TE_{0n} ($n = 1, 2, \ldots$) modes exhibit a unique property that they monotonically decrease as a function of frequency [73, 2]. Also, TE_{01} mode has higher Q factor than the dominant TE_{11} mode and lower conductor loss because there is no axial current component, i.e. $\mathbf{H}_\phi$=0. Due to disturbance in the passband from other modes, a disadvantage with the TE_{01} mode is a limited passband coverage compared with the dominant TE_{11} mode. However, a practical advantage of trying higher order modes is that the ratio D/pitch (of the tuning screw) becomes larger making adjustment mechanically more stable.

The temperature of the receiver box surroundings, where the notch filter is placed, is expected to be in the range between 22 and 35 °C. By a measurement setup with a convection heat source and a network analyzer it was found that the temperature drift at perturbations around 25 °C is approximately -2.6 MHz/°C. This drift is limited and will downshift the resonance frequency of the notch filter by at most 33.8 MHz which is found acceptable. In nowadays radiometer systems temperature controlled chambers are widely used to minimize temperature drifts.

5.3   140 GHz notch filter for ECE

Here we present a design of a notch filter with a center frequency of 140 GHz, a rejection bandwidth of $\sim$ 900 MHz, and a typical insertion loss below 2 dB in the passband of ± 9 GHz. The design is based on a rectangular waveguide with 8 cylindrical cavities coupled by T-junction apertures formed as thin slits. Parameters that affect the notch performance such as physical lengths and conductor materials are discussed. The excited resonance mode in the cylindrical cavities is the dominant TE_{11}. The performance of the constructed filter is measured using a vector network analyzer monitoring a total bandwidth of 30 GHz. We compare the measurements with numerical simulations. A major part in this part of the thesis will focus on sensitivity analysis on various filter parameters. In Sec. 5.3.1 we discuss background and theory on rectangular and circular waveguides. In Sec. 5.3.2 we discuss numerical methods and simulation results while in Sec. 5.3.3 we focus on experimental results.

5.3.1   Slit-coupled T-junction for waveguides

H.A. Bethe developed a perturbation technique to calculate the power transmission through and reflection by small irises (slits) in standard waveguides [4]. Bethe's approach is based on the following two steps. The first step is to calculate the electric dipole moment, $\bar{\mathbf{p}}$, and the magnetic dipole moment, $\bar{\mathbf{m}}$, induced in the slit by the exciting fields. The next step is to calculate the power radiated due to the electric and magnetic dipole moments. The emanating total fields are calculated from electric and magnetic equivalent sources, a technique also used for aperture antennas. The equivalent sources take the form of short dipoles when the radiating structure/gap/hole is sufficiently small compared with the vacuum wavelength λ_0.

Waveguide notch filters can be designed using several different constellations out of which we consider one. The main waveguide has standard dimensions, and the resonators have circular cross sections. The lengths, depths, and widths of the coupling slits and the cavity resonator lengths are the degrees of freedom. The optimum insertion loss characteristic is found from a trade-off in these parameters.
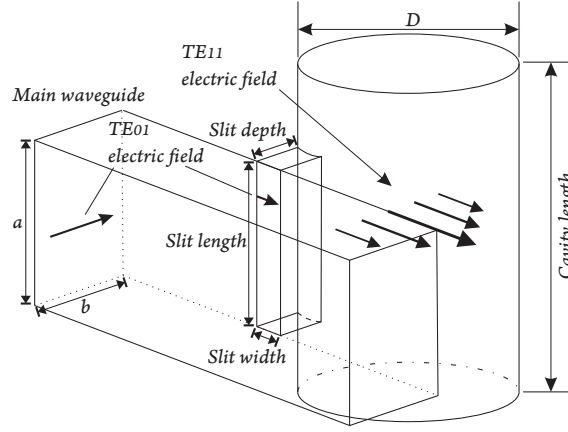
Figure 5.12: T-junction aperture coupling using a thin slit and vertical cavity scheme. The fixed dimensions are $a = 1.651$ mm, $b = 0.826$ mm and $D = 1.31$ mm.

The geometrical layout behind the 140 GHz notch filter is adapted from the resonator-coupling figure presented by Rizzi [65, p.434] and is shown in Fig. 5.12. This notch filter construction is composed of a symmetrical right-angle T-junction of two waveguides which are coupled by a narrow slit in a wall that is electrically thin, i.e. the slit width is much smaller than $\lambda_0 = c/f_0 = 2.1$ mm. The slit widths are restricted to a minimum value for a certain machining technology, usually > 0.1 mm, which is much less than 2.1 mm as required. Later we show that the slit width has large impact on 3 dB rejection bandwidth.

The resonators at the end of each T-junction can be designed using two approaches [51]. The simplest way is to use cylindrical cavities due to the tuning screw mechanism otherwise rectangular cavities can also be used. The resonators with a diameter of $D = 1.31$ mm are placed equidistant along the main waveguide. The electric field component of the dominant TE_{10} rectangular guide mode is coupled to the electric field component of the TE_{11l} circular cavity mode with a thin slit [65, p.431]. The subscript l is a number of $\lambda_g/2$ multiples in the resonator. λ_g is the guide wavelength and l is the cavity length given described in Eq. (5.1). For the circular waveguide, $\lambda_{c,nm} = \pi D/p_{nm}$ where p_{nm} correspond to the m'th root of the derivative of first order Bessel function. For the TE_{11} mode we have $\lambda_{c,11} = 1.31\pi/1.841 = 2.24$ mm and $\lambda_g = 7.4$ mm. This gives the possible cavity lengths $l = \{3.7, 7.4 \ldots\}$ mm. Figure 5.3 would have shown us the same results with the product $D[\text{mm}] \cdot f_{res}[\text{GHz}] = 18.34$ giving the ratio $D/d = 0.348$ defined by the dominant TE_{111} mode. The distance between cavities in Fig. 5.13 is determined as an odd number of quarter wavelengths $\Delta l = \frac{\lambda_g}{4}(1 + 2N)$ where $N = \{0, 1, 2 \ldots\}$ and λ_g is the guide wavelength for the main rectangular guide. We first find $\lambda_c = 2a = 3.30$ mm, where $a = 1.651$ mm is the broad side of the main guide and then using Eq. (5.1) we find $\lambda_g = 2.8$ mm. Due to geometrical limitations we set $N = 1$ (not $N = 0$), that gives $\Delta l = 2.1$ mm which is the value we use in the design phase. A planar cut of the simulated notch filter and photo of the realized notch filter are shown in Fig. 5.13.

5.3.2 Numerical methods and results

Numerical simulations are used to optimize the coupling slit dimensions mentioned in Sec. 5.3.1. Maxwell's equations with boundary conditions describe the electromagnetic field distribution inside a waveguide, the coupling slits, and resonator cavities [65, pp.24-
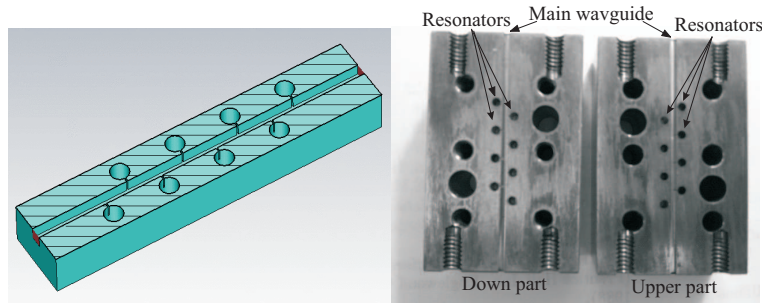
Figure 5.13: 3-D horizontal cut and photography of the 140 GHz notch filter with eight cavities.
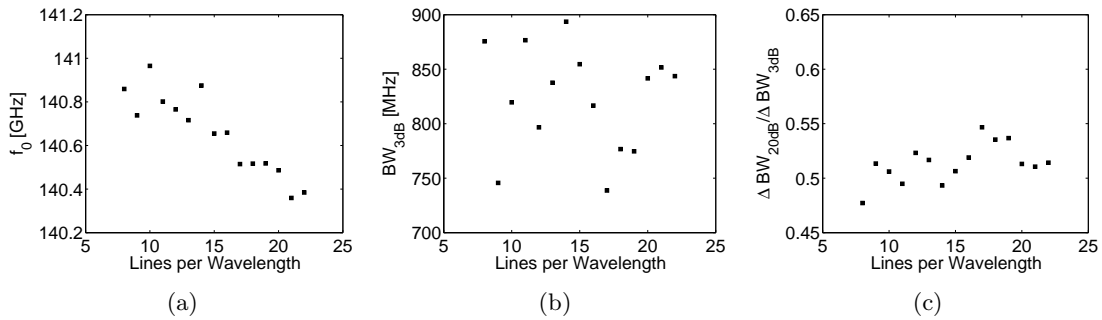

(a)	(b)	(c)

Figure 5.14: Convergence study of the filter parameters plotted as functions of lines per wavelength (L/λ_0): (a) Center frequency; (b) 3 dB bandwidth; (c) shape factor.

28]. CST [1] is a time domain solver based on the finite element method used to calculate the fields existing inside the structure. The output from the solver is the frequency dependent scattering parameter (S-parameter) S_{21}, better known as insertion loss or transmission loss.

We compute the results on various meshes with increasingly finer resolution to test the convergence. Figure 5.14 shows the notch frequency f_0, the 3 dB bandwidth, and the shape factor as a function of mesh size, here calculated as lines per wavelength (L/λ_0) where $L/\lambda_0 = 22$ corresponds to 2.6 million meshcells. The center frequency f_0 shifts down 500 MHz when the grid resolution is increased from 8 to 22 lines per wavelength. The 3 dB bandwidth oscillates between 750 and 900 MHz for low values of lines per wavelength (8 to 18). At 20 lines per wavelength, the 3 dB bandwidth has settled to ~ 840 MHz. The shape factor is a ratio of the bandwidths at two different stopband levels: IL = 3 dB (half power) and IL = 20 dB (1% power transmission), i.e. shape factor = $\text{BW}_{20dB}/\text{BW}_{3dB}$ and is a number between 0 and 1. A desired scenario is that 3 dB points and 20 dB points have equal bandwidths giving ideal selectivity in form of two vertical lines when S_{21} is plotted versus frequency, i.e. shape factor = 1. In Fig. 5.14 the shape factor changes only slightly from 0.48 up to 0.52, so the computed filter selectivity is independent of the grid. Due to 3 dB bandwidth uncertainties in Fig. 5.14 (lower-left), we choose the highest applicable number of lines per wavelength in order to achieve reliable S-parameter values. The simulations shown in this paper will be that of 20 lines per wavelength as a compromise between the calculated filter parameter accuracy and simulation time.

All narrowband mm-wave filters, i.e. $f_0/\text{BW}_{3dB} \gg 1$, are sensitive to mechanical imperfections and therefore should be tunable. In our case, the only adjustable parameter

---

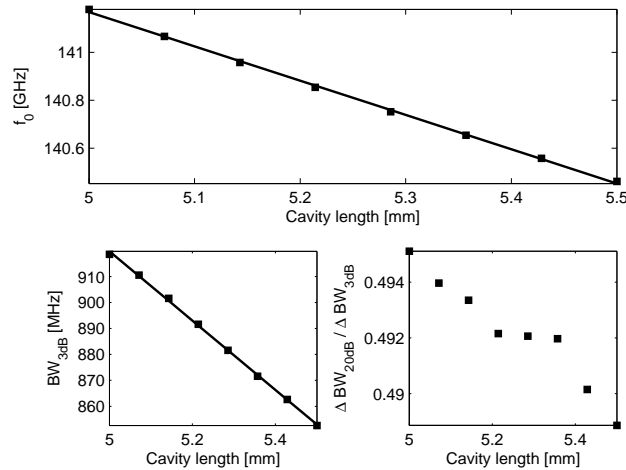[1] Computer Simulation Design, Microwaves & RF, www.cst.com

Figure 5.15: Sensitivity of the center frequency f_0, the 3 dB bandwidth, and the shape factor to changes in the *cavity length*, see Fig. 5.12. Symbols: simulations; line: least squares fit.

is the length of the cylindrical cavities. This filter has eight cavities and their respective lengths are identical for each simulation run. Individual cavity tuning is time consuming. In the following sensitivity analysis of the geometrical parameters will be presented. Some of the data sets are aligned so well that linear least squares fit is applied. Otherwise, the highest absolute gradient among the points is calculated, i.e. the highest sensitivity.

Table 5.2 shows the sensitivity overview of the filter design parameters to the geometrical changes. The center frequency in Fig. 5.15 (upper) varies linearly as a function of cavity length with a slope of -1.43 GHz/mm. The cavity length is 5.8 mm, for all 8 cavities, when centered at 140 GHz. The 3 dB bandwidth, BW_{3dB}, in Fig. 5.15 (lower-left) is also linear in its response and changes with -130 MHz/mm which is an acceptable value. Ideally, we prefer no change in the filter bandwidth (low sensitivity) when the cavities are being tuned. The worst case shape factor in Fig. 5.15 (lower-right) has a relatively small change by -0.026 per mm. The BW_{3dB} bandwidth is linear for small perturbations in cavity length with a slope of 130 MHz per mm. It is possible to improve the selectivity of the filter by tuning cavity lengths individually to slightly different frequencies. This process has not been investigated. The main purpose of cavity tuning is to adjust the center frequency f_0 to the point of resonance.

The slit depth (Fig. 5.16) is a nontunable parameter, so choosing this value carefully is important. The worst case f_0 gradient is -10.71 GHz/mm, which according to table 5.3 is the most sensitive parameter. The 3 dB bandwidth slope is -2.92 GHz/mm. The shape factor slope is low -0.459 per mm, which is considered good. Choosing a slit depth of 0.28 mm results in a 3 dB bandwidth of 900 MHz as required.

Figure 5.17 shows the effect of changing the slit width and is found to be a relatively sensitive parameter in all three categories: center frequency f_0 has a slope of 7.41 GHz/mm, and 3 dB bandwidth has local gradients up to 11.96 GHz/mm in the range of interest. However, the shape factor grows with slit width. The slit width is chosen to be 0.1 mm, which is the the lowest possible value due to machining limitations.

The center frequency and 3 dB bandwidth are very sensitive to the slit length as shown in Fig. 5.18. From Fig. 5.18 (lower-left) we choose the slit height to be equal to side a of the main waveguide, 1.651 mm, otherwise the 3 dB bandwidth will become too large.

Figure 5.16: Sensitivity of the center frequency f_0, the 3 dB bandwidth, and the shape factor to changes in the *slit depth*, see Fig. 5.12.

Figure 5.17: Sensitivity of the center frequency f_0, the 3 dB bandwidth, and the shape factor to changes in the *slit width*, see Fig. 5.12. Symbols: simulations; line: least squares fit.
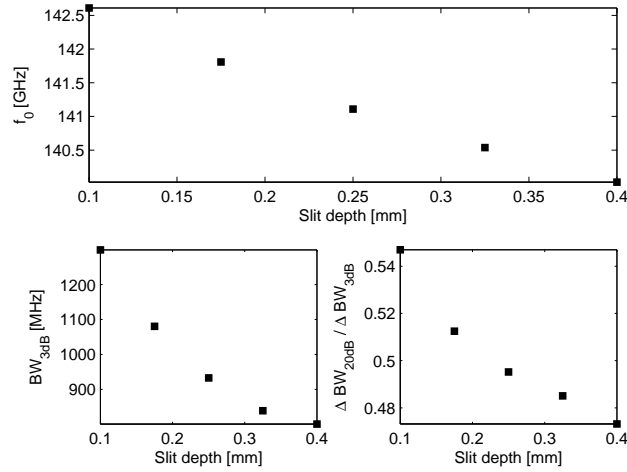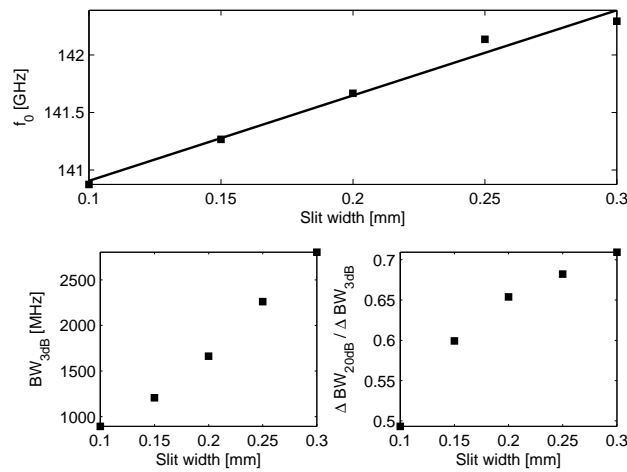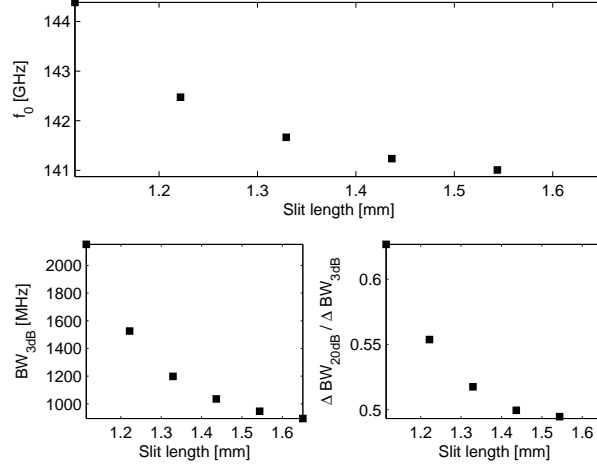
Figure 5.18: Sensitivity of the center frequency f_0, the 3 dB bandwidth, and the shape factor to changes in the *slit length*, see Fig. 5.12.

	f_0 [GHz/mm]	3 dB bandwidth [GHz/mm]	Shape factor [mm^{-1}]
Cavity length	**-1.43**	**-0.13**	-0.026
Slit length	-17.83	-5.85	-0.681
Slit width	**7.41**	11.96	2.121
Slit depth	-10.71	-2.92	-0.459

Table 5.3: Sensitivity analysis: impact on key characterization parameters by varying the design lengths. Bold numbers are found by least squares fit.

The material choice is an important factor when minimizing the overall passband transmission loss, especially at the points around the rejection band. A clear difference in 3 dB bandwidth and shape factor from good to very good conductor is shown in Fig. 5.19. As presented in Fig. 5.19 (lower-left), the 3 dB bandwidth drops by 30% when changing conductivity from 10^7 S/m to $6 \cdot 10^7$ S/m. It is in agreement with microwave theory that the filter quality factor $Q \approx f_0/BW_{3dB}$ improves with conductivity. The shape factor increases accordingly. Commonly either copper- ($\sigma = 5.96 \cdot 10^7$ S/m) or silver-coating ($\sigma = 6.3 \cdot 10^7$ S/m) are used as a construction material for frequencies above 110 GHz. For frequencies between 30 and 110 GHz it is recommended to use gold ($\sigma = 4.52 \cdot 10^7$ S/m) or copper leaving silver-coating as an option.

5.3.3   Experimental Results and Discussion

Eight resonator cavities are found to be a good compromise between filter performance and design complexity (see Fig. 5.13). The distance between resonators Δl in Eq. (5.1) was optimized to $\Delta l \simeq \lambda_g/4 \simeq 2.1$ mm which fulfilled the requirement that the cylindrical resonators should be placed closely together to minimize insertion loss without any geometrical conflict. The eight cavities were tuned one at a time until their respective resonances were positioned at the center frequency of 140 GHz.

Based on the simulation findings, a notch filter with the following coupling geometry has been designed and built from copper: slit width of 0.1 mm, slit depth of 0.28 mm, and slit length of 1.651 mm. The tiny slit width was milled out in copper using a 0.1 mm diamond mill removing only 0.05 mm copper from the top in each run. After final adjust-
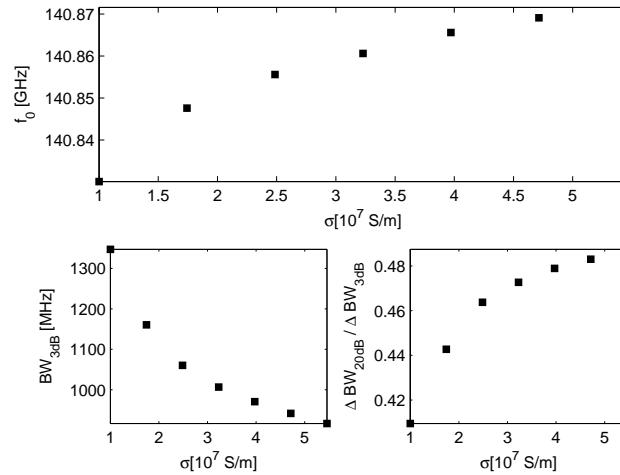
Figure 5.19: Center frequency (upper), 3 dB bandwidth (lower-left), and shape factor (lower-right) are plotted versus conductivity corresponding to good conductors.

ments using a network analyzer from AB millimetre, cavity lengths were spread from 4.92 to 5.6 mm. Figure 5.20 compares the measured insertion loss with simulations. The typical loss in the passband is below 2 dB. However, spurious notches appear at ~ 145 GHz. The cavity lengths discrepancy of $5.6 - 4.92 = 0.68$ mm can only explain 1 GHz offset according to Tab. 5.3, which is not enough to explain the extra notches that show up. One likely explanation for these spurious notches is that the tuning screws leak a small portion of the electric field between the thread and the filter housing. The electric field inside the cavity therefore sees an electrically larger cavity than suggested in the simulated design. The notch filter performance can thus be improved by increasing the number of threads per axial distance or by increasing the cavity diameter, without changing the mode. Another more likely explanation is the interaction between the fringing fields around the coupling apertures of resonators close to each other [51, p.754]. Therefore a second version of a notch filter was constructed, but this time with $3\lambda_0/4$ spacings between resonators and no spurious notches were observed. However, the simulated value (5.8 mm) is close to the measured one (~ 5.4 mm), showing good accuracy of the simulations. A way to avoid spurious notches is to improve the tuning screws using an alternative construction [26] or exciting the TE_{01} mode in the cavities. The current flow in this mode has only an azimuthal component, so the fields are not disturbed by poor electrical contact between the tuning screws and the cavity housing. TE_{01} is the third higher order mode with reduced passband coverage which is, however, still useful for CTS experiments and possibly for ECE. Another possible explanation to the spurious notches is an imperfect facing of the upper and bottom halves since both sides are milled individually.

The network analyzer dynamic range of approximately 60 to 90 dB, depending on the analyzer settings such as IF bandwidth and average factor, is the limiting factor when components with deep rejections are tested. Therefore, notch filters who are specified to reject more than 90 dB should be designed as two components and then connected in a cascade. In the CTS lab, we have succeeded to construct a low-cost insertion loss analyzer just to monitor basic S_{21} or S_{12} parameter, see Fig. 5.21. The analyzer is based on the principle of using a commercial low-frequency (e.g. 20 GHz) VNA adding an external up-converter stage. The new analyzer is controlled by a fixed LO plus the output signal from the VNA, producing the RF output test signal. The two mixers do the frequency
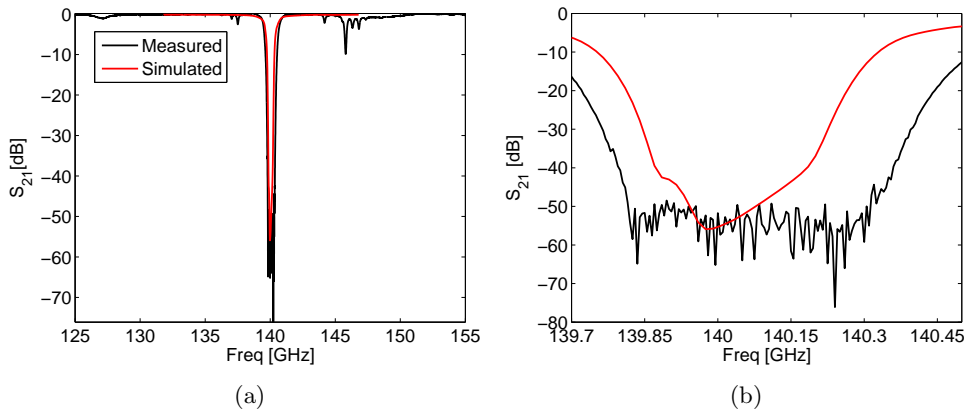
Figure 5.20: The 140 GHz notch filter measurements and simulations: (a) The full band; (b) Zoom around the notch.
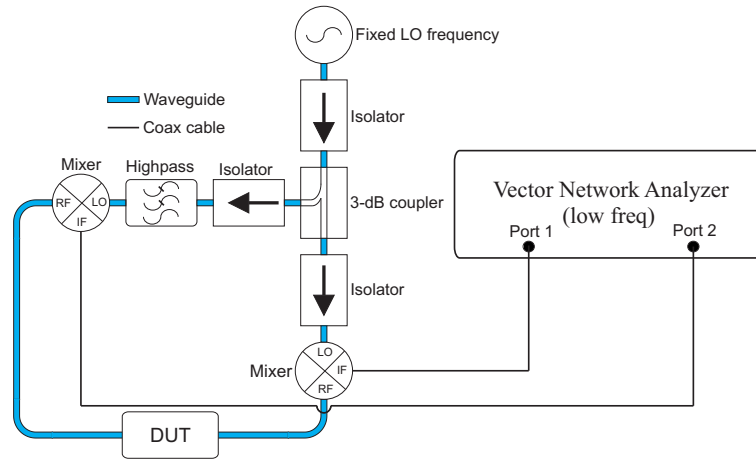

Figure 5.21: Diagram for measurement of parameter S_{21} or S_{12}

shifting where the IF ports of the mixers are connected to the VNA and the LO ports are fed with a signal from a fixed frequency LO through a 3 dB coupler. Between the mixer RF ports we place the DUT using straight pieces of a WR-10 waveguide and two E-bends in order to keep the total waveguide length short. Isolators are recommended to use in order to avoid back-reflections and self-mixing, while a high-pass filter ensures that leakage of the low frequency signals from the VNA will be rejected before it reaches the fixed frequency LO. For a passive device test it is sufficient to implement only one high-pass filter, for instance in Fig. 5.21 we measure only S_{12}. If both S_{21} and S_{12} parameters are required then the two mixers must be able to mix up- and down in frequency and additional high-pass filter is required in front of the other mixer LO port. The measured data is viewed and stored by exploiting the facilities integrated in the low-frequency VNA. Measurements from this test set-up have been compared with the commercial 110 GHz VNA from Anritsu. Successful results are achieved as seen from Fig. 5.22 where dynamic range of more than 60 dB was observed. The disadvantages with this measurement set-up are several, where the most crucial ones are sensitivity to temperature drifts, LO with no phase-lock technique, and difficulties in achieving good calibration standards.
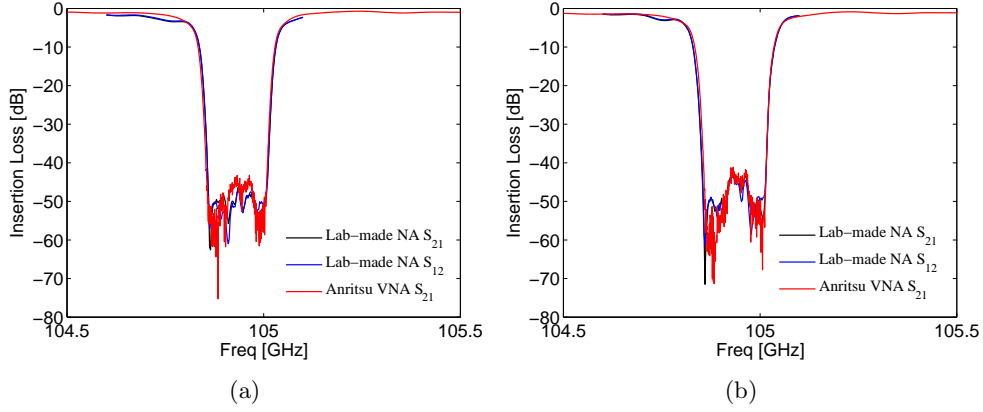
Figure 5.22: The two notch filters from the CTS receiver installed at ASDEX Upgrade are mea-
sured using lab-made set-up (black and blue lines) and compared with a commercial
110 GHz VNA from Anritsu (red line): (a) Filter A; (b) Filter B.

5.4   New designs based on thin slit coupling

The design principle based on T-junction thin slits, described in Sec. 5.3, produced good
experimental results with no spurious modes in the spectrum. We decided to use this
approach as a standard for the notch filters needed in further experimental work on CTS.

In Fig. 5.23 we show two designs on notch filters with 7 and 9 resonators. The filters
are designed to cover stray radiation from a single gyrotron, so suppression larger than
80 dB in 120 MHz bandwidth is considered to be sufficient. Both filters are based on
TE_{011} mode, shown in Fig. 5.3, in order to achieve larger Q factor and thereby more
narrow rejection bandwidth. The passband is relatively wide and the closest mode is
TE_{311} appearing around 114 GHz. The distance between the resonators is $5\lambda_g/4$ in order
to avoid the fringing fields discussed in Sec. 5.3.3. The diameter of the cavities is 3.8 mm
and the cavity lengths are approximately 3.7 mm. The number of the cavities is chosen
to be odd since we meet the insertion loss requirements according to the Tchebychev
scheme on frequency response [65]. The resonators have, according to the Fig. 5.4(b), a Q
factor of approximately 9100 which is higher compared with the TE_{111} mode. The TE_{011}
mode is almost sufficient for covering stray radiation coming from a single gyrotron, i.e
the filters are tuned for a slightly different center frequency in order to accommodate the
bandwidth of the gyrotron. The filters show much better performance compared with the
previous design in Sec. 5.2. The final measurement, shown in Fig. 5.23 (right), is achieved
by tuning both filters together in series otherwise we would have a small "bump" in the
middle of the notch. If we compare the measurements from this new design with a similar
filter provided by General Atomics in Fig. 4.5(a) we see considerable improvements of the
insertion loss in the range from 108 to 110 GHz.

A notch filter with rejection bandwidth of 1 GHz centered at 105 GHz has been de-
signed and tested, see Fig. 5.24. The passband coverage is larger than 30 GHz which is
the first time recorded in community for fusion diagnostics. We are using the dominant
TE_{111} mode (see Fig. 5.3) with cavity diameter of 2.1 mm and length of approximately
2.43 mm. The distance between the resonators is, similarly to before, $5\lambda_g/4$. The res-
onators have a Q factor of approximately 3500 which makes the filter sufficiently broad
in the rejection bandwidth to protect the ECE receiver from stray radiation emitted by
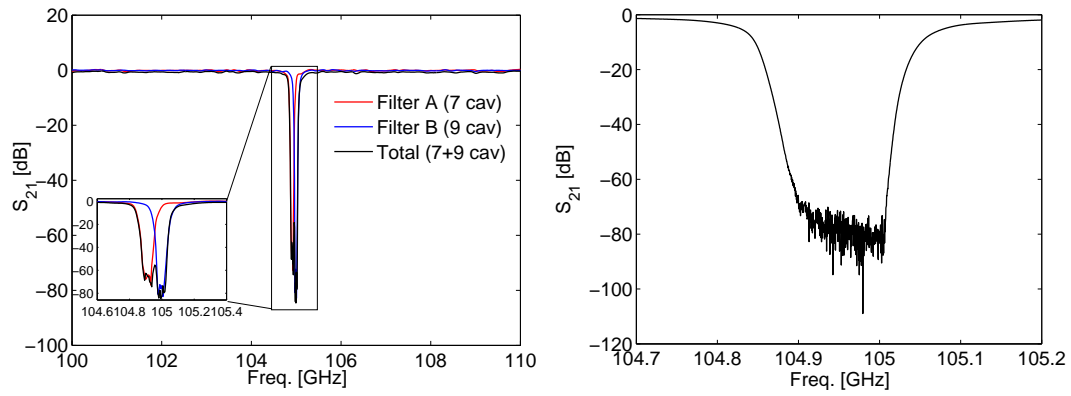several gyrotrons.

Figure 5.23: Two narrowband notch filters for the new CTS receiver installed at ASDEX Upgrade.
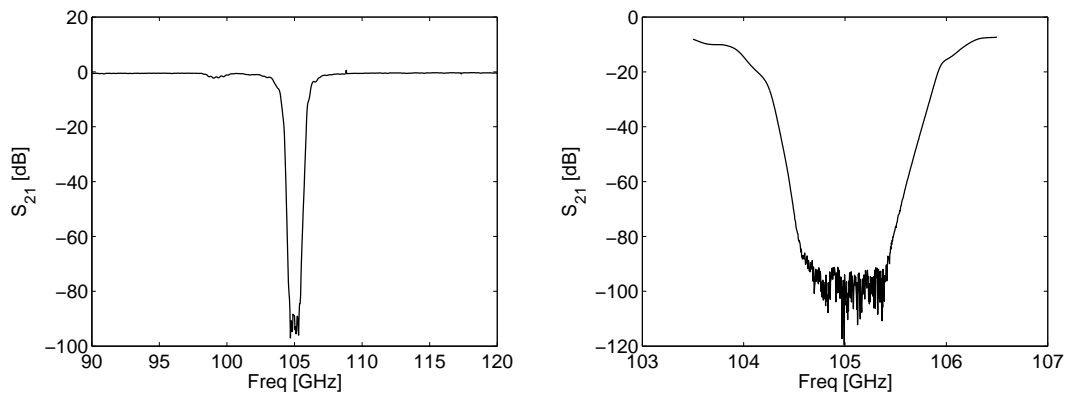

Figure 5.24: A notch filter with wide rejection for the ECE group at ASDEX Upgrade. This filter will protect the ECE receiver during piggy-back experiments where the CTS group is also participating.

f_0 [GHz]	Pass. BW [GHz]	Rej. BW$_{3dB}$ [MHz]	Rej. [dB]	Ref. / name
105	90-110	1300	30	[24]
140	125-155	950	55	[23]
105	90-110	150	65	CTS-AUG2 NF1
105	90-110	150	70	CTS-AUG2 NF2
105	90-120	1000	80	ECE NF1
105	100-108	120	60	CTS-AUG1 A/B
68	53.6-78.3	1500	80	[15]
170	169-173	1100	85	[18]
82.6	82.2-83	500	80	[18]
110	105-112	300	60	[93]
140	139.8-140.2	70	50	[20]

Table 5.4: A list of notch filters designed for fusion experiments. CTS-AUG2 refers to the new CTS receiver installed at AUG, while CTS-AUG1 is the old receiver at AUG. Abbreviations NF1 and NF2 refers to the two notch filters described in Sec. 5.4. The passband bandwidths found in the references are either approximately measured using presented graphs or cited from the text.

We summarize the designed and measured notch filters, known in the fusion community and many of them published, in the Tab. 5.4. The notch filters performed by the CTS group are unique when it comes to the passband bandwidth and attenuation roll-off (shape factor).

5.5 Conclusions

We have presented design and measurements on 5 different notch filters, four of them are centered at 105 GHz and the last one is centered at 140 GHz. Two design approaches based on different geometry are presented, the first uses irises as coupling apertures while the second uses thin slits formed as T-junctions. The latter choice have proven to be more consistent with the theoretical expectations. For the notch filters with narrow rejection bandwidths it is best to use higher order modes such as TE$_{01}$, otherwise for notch filters with broad rejection bandwidths it is best to use the dominant TE$_{11}$ mode. Simulations confirm that narrower rejection bandwidths are achievable by increasing the slit depth, which is relevant for CTS experiments. The key design parameters such as center frequency f_0, 3 dB rejection bandwidth BW$_{3dB}$, and shape factor are estimated by tuning the geometry of the coupling slit and the cavity lengths. The sensitivity of measured insertion loss has been predicted with simulations by changing filter geometry. The simulation data in Tab. 5.3 shows that small geometrical changes have considerable impact on filter parameters such as center frequency f_0, 3 dB bandwidth BW$_{3dB}$, and shape factor. It is also possible to perform insertion loss measurements without a high frequency VNA, but instead just to use a standard low frequency VNA. Components such as two mixers, an LO, some isolators, a high-pass filter, a 3 dB coupler, and waveguide pieces are needed but the overall cost is still much below a commercial VNA.

Chapter 6

Subharmonic Mixer Design

6.1   Short background and introduction

An array of plasma control systems exist for a stable plasma operation. In particular the so called tearing modes, or neoclassical tearing modes (NTMs), form islands in the magnetic topology of the tokamak and can reach a size of several percent of the plasma cross section. This event is sufficient to break the established magnetic confinement in the vessel. Moreover, NTMs grow larger as the pressure in the vessel is raised to the values required for break-even. When NTMs grow too large they can evoke sudden termination of the plasma; a phenomenon known as a disruption. In ASDEX Upgrade a range of successful experiments have been performed with the intention of characterizing and stabilizing NTMs [32, 30]. One promising method is localized current drive controlled by the ECRH or ECCD [97]. A powerful heating source such as an NBI is used to trigger NTMs in the plasma whereas two gyrotrons at 140 GHz, delivering RF power of approximately 800 kW each, are used to stabilize the plasma. The frequency of operation relevant for detection of NTMs in ASDEX Upgrade is therefore set to 140 GHz.

We use a heterodyne receiver architecture with a mixer followed by IF amplifiers to detect electromagnetic radiation at 140 GHz coming from AUG plasmas based on NTM scenarios. In a heterodyne receiver we down-convert high frequency signals, keeping the amplitude and the phase intact, to lower frequencies where filtering and post processing are achieved relatively easy. The process of down-conversion is achieved using a mixer. Several types of mixer topologies exist out of which we will consider the subharmonic mixing principle where harmonics of second- or higher order are used to down-convert RF signals in the high frequency range to the IF in the low frequency range [33, 25, 37]. In this design we choose to use an LO harmonic of second order, i.e. the LO frequency is set to 65 GHz where the second harmonic at 130 GHz converts RF in the range 135 to 145 GHz to IF in the range 5 to 15 GHz. Due to limited availability of the LNAs in the mm-wavelength range there is no option to boost the RF signal before it reaches the mixer IF port. Since the insertion loss in the RF line will increase the system noise figure, the design requirements are low conversion loss during frequency translation, low noise figure, and high isolation between the LO to RF ports and similarly between the LO to IF ports. Presently, there are no mixers based on HEMT technology used in mm wave diagnostics for fusion plasmas. Here we present a proposal for a mixer design to be used in mm-wave diagnostics for fusion plasmas.
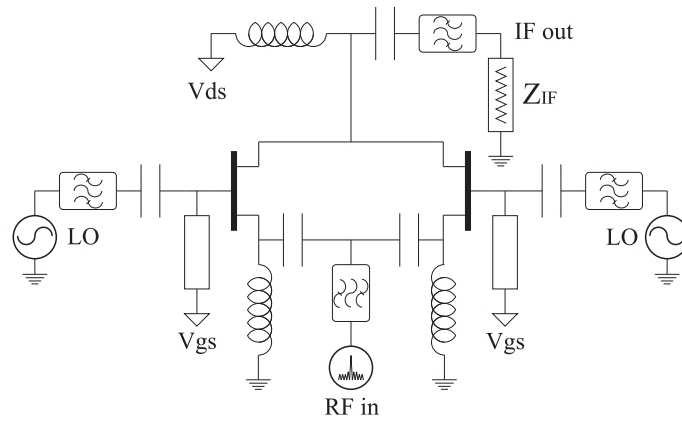
Figure 6.1: Subharmonic mixer topology with the RF signal applied at the common-source node and the IF signal taken across the IF matching impedance Z_{IF}, usually 50 Ω.

6.2   The subharmonic mixer (SHM)

The mixer circuit presented in this paper is based on Gallium Arsenide (GaAs) meta-morphic high electron mobility transistors (mHEMT) technology which has relatively good electrical performance and acceptable cost. From historical aspects, GaAs based pseudomorphic HEMT (pHEMT) technologies have served microwave industry as a true work-horse for MMICs operating in the mm-wave range [31]. The mHEMT technologies were developed in the late 90's and are commercialized at several foundries around the world such as OMMIC, Triquint, UMS and others. Compared to pHEMT technology, the great benefit of mHEMT is high f_T and f_{max} achieved by the increased indium concentration in the channel. Hereby, the transistor parameters (f_T, f_{max}), and noise, and DC performance are close to indium phosphide (InP) based HEMTs which traditionally have been considered most suitable for high-frequency MMIC design. However, they are rarely used for commercial mm-wave receivers due to their fragile nature and high production cost.

The mixer topology, we attempt to explore here, is a differential pair of transistors driven with two LO signals that are 180° out of phase at the two gates, respectively. The LO signal should be sufficiently high in order to drive the transistors as a perfect on-off switch pair with only one transistor conducting at a time, i.e. V_{gs} (gate-to-source voltage) is rapidly changing from a non-conducting stage at $V_{gs} = V_t$ (threshold voltage which is usually negative for mHEMTs) to a full conducting stage at $V_{gs} > 0$ V. The two source nodes are connected with RF signal applied at the common node. The bias circuit at the source (inductor+capacitor) act as high-pass filter preventing LO leakage, so that high power LO signal will not escape through the RF port and cause LO self-mixing. The drain nodes of the transistors are connected, and the output is matched using an IF impedance matching stage. The IF output is terminated using a 50 Ω resistor. A conceptual diagram of a subharmonic mixer of second order is shown in Fig. 6.1 where matching circuits are depicted as bandpass filters.

An optimization parameter in active mixer design is to bias the transistor in such a way that the maximum current $I_{d,max}$ will flow through the drain node. The current squared is proportional to the power, so by obtaining the maximum current flow we also
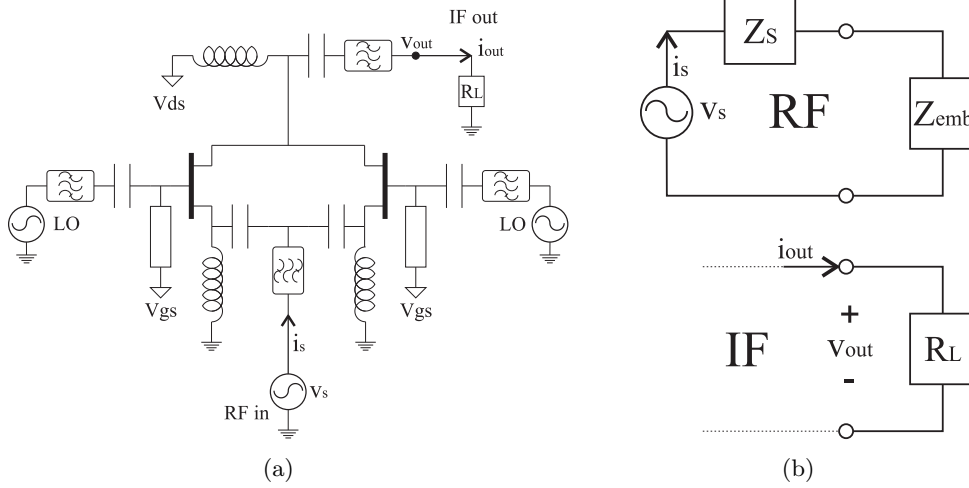
Figure 6.2: Simulation setup of the circuit in ADS: (a) Subharmonic mixer with RF input source and measured IF output as simulated in ADS; (b) The simplified equivalent models to determine the available power at the RF port $P_{av,RF}$ and the power delivered to the IF matching impedance $P_{out,IF}$.

ensure that mixer conversion gain, G_{cnv}, is maximized and determined as [45]

$$G_{cnv} = P_{out,IF} - P_{av,RF} \ [dB], \ \text{where} \tag{6.1}$$

$$P_{av,RF} = 10 \log_{10} \left(\frac{1000 \cdot |V_s|^2}{8 \cdot \Re\{Z_S\}} \right) \ [dBm], \ \text{and} \tag{6.2}$$

$$P_{out,IF} = 10 \log_{10} \left(1000 \cdot \tfrac{1}{2} \cdot |i_{out}|^2 \cdot \Re\{Z_L\} \right) \ [dBm]. \tag{6.3}$$

where the source and load impedances are real $\Re\{Z_S\} = \Re\{Z_L\} = 50$, and the quantities V_s and i_{out} are peak voltage and current, respectively. Equations (6.2) and (6.3) are derived from the parameters used in Fig. 6.2(b). The mixer conversion gain G_{cnv} is also described as transducer power gain G_{tr} but in mixer design conversion gain is the most used term. The value of G_{cnv} is generally the most desired parameter in the mixer design, since mixer noise figure (NF) is close to G_{cnv}. Equation (6.1) reads that G_{cnv} is defined as power delivered to the load (IF) minus power available from the input (RF). Depending on the bias and matching network at the IF port, a portion (preferably all) of the drain current I_d will be delivered to the IF load resistor generating power $P_{out,IF}$ across it. Another important remark is that we do not assume perfect matching, i.e. $P_{in,RF} \neq P_{av,RF}$, at RF port (eq. (6.1)) meaning that G_{cnv} is defined as a worst case power transmission from the RF input to IF output. G_{cnv} does not depend on the RF input signal as long as it is much lower than the applied LO signal, which makes the down-conversion a linear process.

6.3   DC analysis and biasing circuit

The initial step in the mixer design is to find proper DC bias circuitry using transmission lines or inductors as RF blocking components (DC-couplers) and using capacitors as DC blocking components (AC-couplers). The biasing components including transmission lines will change the frequency responses of voltages and currents at all nodes in the circuit and thereby the input impedance Z_{in} at all three mixer ports RF, LO, and IF.
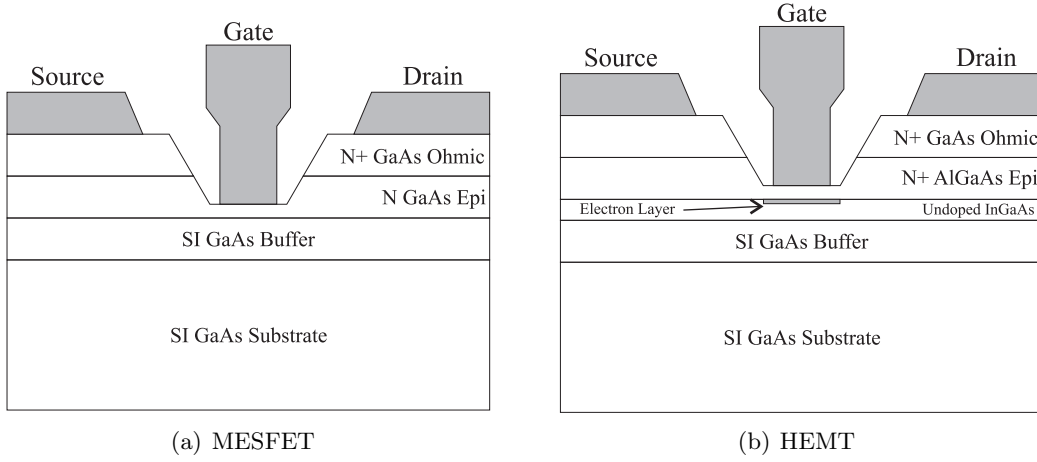
| (a) MESFET | (b) HEMT |

Figure 6.3: Cross-section of two well-known GaAs FET devices using a T-shaped gate. GaAs MESFET transistors are easy to fabricate but f_{max} is at most 30 GHz and the noise figure and power performance are not as good as for the HEMT devices. In HEMT devices the channel material is InGaAs resulting in an extremely low noise figure and f_{max} higher than 100 GHz.

For mHEMT technology we prefer to bias the transistor in the saturation region with the consequence that changes in V_{ds} have limited influence on the drain current I_d. To achieve this we require that the gate voltage is of the same polarity as the drain voltage. An additional requirement, for most mHEMTs, is to increase the drain-to-source voltage so that $V_{ds} > V_{gs} - V_t$. We will later see that the gate-to-source voltage can be omitted ($V_{gs} = 0$) and the bias network requirement is reduced to the optimization of V_{ds}. V_t is the threshold voltage and its value depends on the electrical properties of the substrate layer. The value of V_t can vary a lot between different production batches and is usually specified by the manufacturer in the range -1 to -0.2 V for mHEMTs. A simple high-frequency equivalent electrical model of a MESFET (which has very similar electrical properties as a HEMT) is shown in Fig. 6.5.

The drain current in a mHEMT transistor is a function of voltages across its terminals:

$$I_d = I_d(V_{gs}, V_{ds}), \tag{6.4}$$

where $I_d = I_{DD} + i_d(t)$ is the drain current and a non-linear function of gate-to-source $V_{gs} = V_{GG} + v_{gs}(t)$ and drain-to-source voltage $V_{ds} = V_{DD} + v_{ds}(t)$. Capital letters I and V denote DC current and voltages while small letters such as i and v denotes small-signal sinusoidal RF signals. V_{GG} and V_{DD} are bias voltage supplies at gate and drain, respectively. The first three terms in Taylor series for the function I_d become

$$I_d = I_d(V_{GG}, V_{DD}) + (v_{GS} - V_{GG})\frac{\partial i_D}{\partial v_{GS}} + (v_{DS} - V_{DD})\frac{\partial i_D}{\partial v_{DS}}. \tag{6.5}$$

Equation (6.5) can be written in a short form

$$I_d = I_{D00} + v_{gs}(t)\frac{\partial i_D}{\partial v_{GS}} + v_{ds}(t)\frac{\partial i_D}{\partial v_{DS}}, \tag{6.6}$$

where I_{D00} is the absolute DC drain current assuming $RF = LO = 0$ Hz. Notice that I_{D00} is not necessarily equal to I_{DD}. This form of evaluation is only valid for small signals applied at the gate ($v_{gs} \ll V_{GG}$) and the drain ($v_{ds} \ll V_{DD}$). A qualitative description
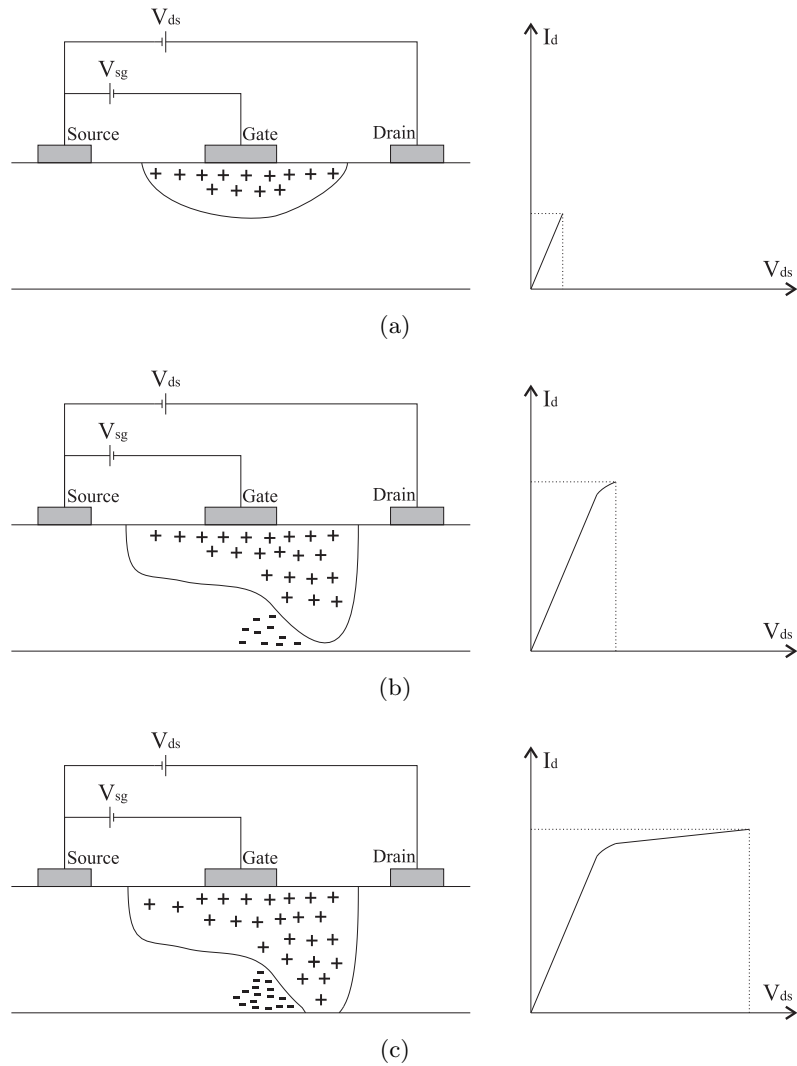
Figure 6.4: GaAs MESFET operation: (a) low V_{ds} but larger than zero; (b) V_{ds} at the saturation point; (c) the transistor is fully conducting, and the current starts to saturate. This is normally region of operation in most mixer designs. The figures depicted are inspired by [49].
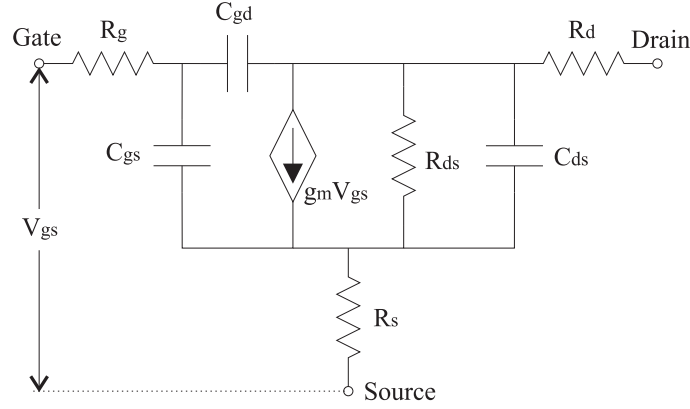
Figure 6.5: Simple high-frequency small signal model of a MESFET. The frequency dependence is distributed among the parasitic capacitances C_{gs}, C_{ds} and C_{gd}. For wideband small-signal modeling the resistors and capacitors in the model will show non-linear frequency dependence.
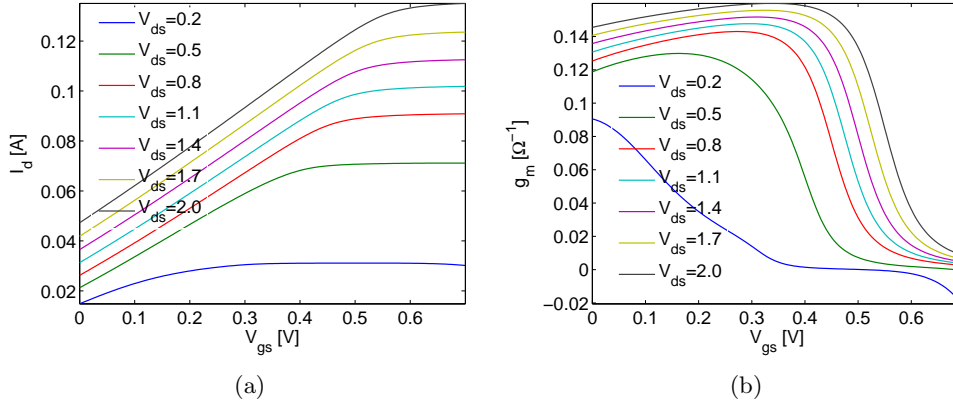

Figure 6.6: DC characteristics for varying gate-to-source voltage V_{gs}: (a) Drain current I_d as a function of V_{gs}; (b) Transconductance g_m as a function of V_{gs}.

of an enhancement MESFET transistor is a voltage-driven current source, i.e. varying the gate-to-source voltage (V_{gs}) from approximately 0 V to 1 V will result in a drain current flow (I_d) from approximately 0 A to $I_{d,max}$. From Eq. (6.6) we find that the voltage-driven current source is characterized by its *transconductance* $g_m = \Delta i_D/\Delta v_{GS}$ which is modeled as the relative change in drain current i_D divided by the relative change in gate-to-source voltage v_{GS}. Usually, we get the largest g_m we get when $V_{gs} > 0$ so that V_{ds} should be positive as well assuming that the transistor source node is grounded in both cases. We here assume that g_m is not dependent on the frequency of the applied signals at the gate or the source. In other words, if we make sure that g_m is maximized at DC, it will give us valuable information where the drain current i_D grows most at all design frequencies.

A similar method to improve the transistor performance is to maximize the output conductance $g_d = \Delta i_D/\Delta v_{DS}$ as expressed in Eq. (6.6). The output conductance is modeled as drain-to-source resistance $r_{ds} = 1/g_d$ as seen in Fig. 6.5.

Varying supply voltages V_{gs} from -3 to 0.5 V and V_{ds} from 0 to 5 V and using terminology for g_m and g_d we get DC characteristics for D007IH mHEMT transistors shown in Fig. 6.6.
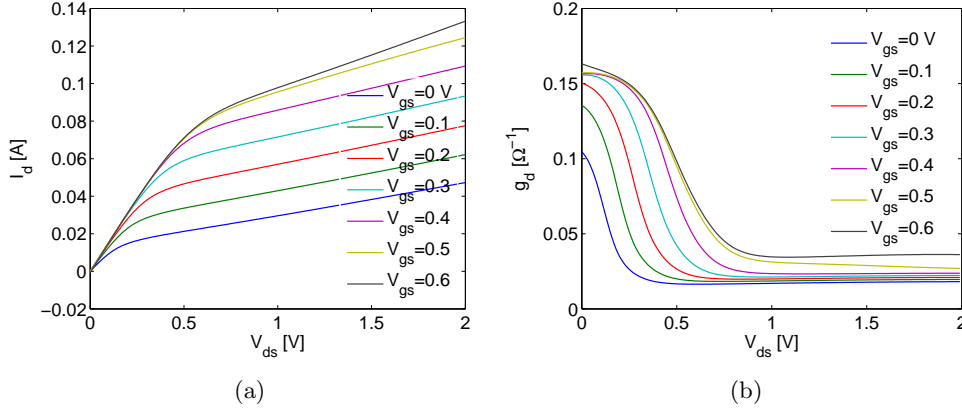
Figure 6.7: DC characteristics varying drain-to-source voltage V_{ds}: (a) Drain current I_d as a function of V_{ds}; (b) The conductance g_d as a function of V_{ds}.

Passive type of mixers using diodes or self-biased transistors are reciprocal meaning we can use RF/IF as the input port and IF/RF as the output port for down/up-conversion, respectively. With a bias at the gate $V_{gs} = 0.3$ V, and the drain $V_{ds} = 4$ V where the source V_s has a DC ground, results in high RF voltage swing at the drain across the 50 Ω load. However, the voltage biasing of the transistors prevents us from using the same mixer as up- and down frequency converter, i.e. the mixer has become directional.

6.4 Concepts of matching

The matching of the mixer is performed at the RF, the LO and the IF ports. Good matching at the RF and IF ports, i.e. return loss less than 10 dB, is necessary for minimizing conversion losses while matching at the LO port is necessary to reduce the LO power drive and thereby the LO leakage. The first matching circuit is designed at the port where the input signal is applied, i.e. the RF port for the down-conversion (our case) and IF port for the up-conversion. In our case we convert 135-145 GHz signals (RF) down to 5-15 GHz signals (IF), we use a down-conversion type of mixer. The second matching circuit is designed at the IF port while LO matching is designed as last step. After the matching circuits are placed at all the three ports, at least one more repetition of matching at all three ports should be performed. This procedure of work does not restrict from other chronological sequences, for instance first match IF then RF and finally LO, but in many cases we get good matching for just one round if we apply the sequence mentioned above (RF->IF->LO).

How to match the mixer ports is an important issue to address. The ideal matching network is a two-port bandpass filter having the mixer output as a reference impedance at port 1 and a load impedance as a reference at port 2. The bandpass filter will remove the unwanted neighbor signal and mixing products, so the signal at the expected frequency band is allowed to pass with minimum loss and signals at different frequencies are absorbed by the filter. At the RF port we detect scattered radiation from the plasma in the range 135 and 145 GHz, while signal at twice the LO frequency should not interfere with the RF signal at the RF port in order to avoid the LO self-mixing. Therefore, the RF matching filter should, ideally, absorb all signals with non RF frequencies.

The impedances at the transistor nodes are frequency dependent and complex while the load associated with the IF port is real and independent of frequency. The mixer
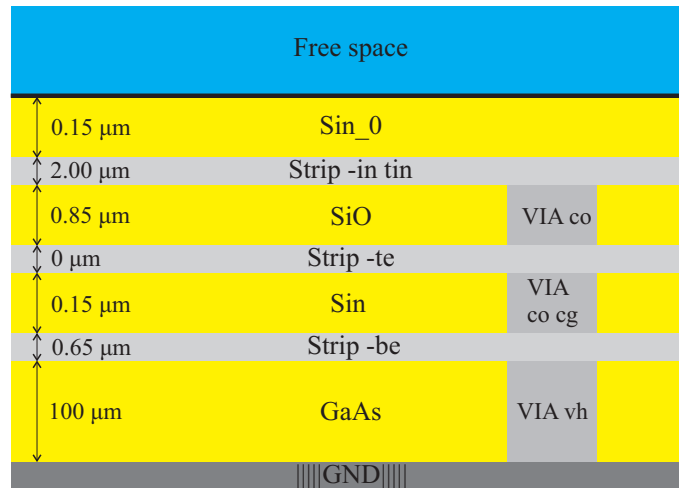
Figure 6.8: Layer structure in the D007 technology; the "te" metal layer has 0 mm thickness and is simulated as a sheet with no expansion. The GaAs layer defines substrate properties of the D007 technology. The layers are not depicted in proportional dimensions.

output impedance has resistance in the range from 5 Ω and up to 200 Ω depending on the biasing values of the transistors. The mixer impedance at the IF port is found by applying a very small test voltage in series with a 50 Ω resistor; then the net current flowing from the voltage source towards the IF matching circuit is measured and hereafter the output impedance is determined by Ohm's law. From network theory, we remember that perfect matching at a single frequency is always possible using a series inductor and a shunt capacitor for loads with a real part less than 50 Ω, and similarly using a series capacitor and shunt inductor for loads with a real part larger than 50 Ω. Therefore, the mixer output requires at least three components in order to obtain matching with fractional bandwidths larger than 50%, i.e. also called broadband matching. The concept of broadband matching is important to address since we need to match IF in the range from 5 to 15 GHz, i.e. fractional bandwidth of 100 %. It is well-known that broadband matching requirements can be met if a sufficient number of components is used. However, at RF frequencies this is not considered as an option due to the limited chip area and parasitics growing with the size of chip area. We have a trade-off between complexity of the matching circuit and the bandwidth requirement. Therefore, in a MMIC design we will mostly tend to aim for a simple matching construction.

6.5   Layout profiles

Layers available in D007 OMMIC technology are shown in Fig. 6.8. There are three metal layers named as: "in", "te", and "be". The "in" metal layer is 2 μm thick and has a conductivity of $2.35 \cdot 10^7$ S/m; the "te" layer is defined without thickness (0 μm); and the "be" layer is 0.65 μm thick and has a conductivity of $2.3 \cdot 10^7$ S/m. There are four dielectric substrate layers named as: "Sin_0", "SiO", "Sin", and "GaAs". The GaAs substrate layer is the one with largest thickness (100 μm) and thereby defines the electrical properties of the transmission lines needed to connect the components on the chip. Details on the substrate layers is given in Tab. 6.1.

	Free Space	$S_{in,0}$	S_iO	S_{in}	GaAs
Thickness [μm]	$Open$	0.15	0.85	0.15	100
ε_r	1	6.8	5	6.8	12.9
μ_r	1	1	1	1	1
Loss Tangent (δ)	0	0	0	0	0.006

Table 6.1: Specification of the dielectric substrate layers available in D007 technology, see Fig. 6.8 for the layout.

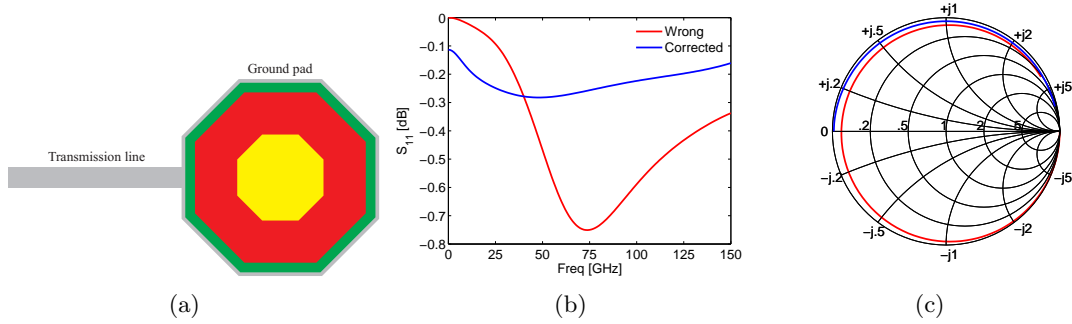(a)   (b)   (c)

Figure 6.9: Octagonal shaped planar via-to-ground: (a) The transmission line is terminated using the via-to-ground built-in component in D007 OMMIC technology. Different colors indicate different composition layers; (b) S-parameter plot; (c) Smith chart plot.

6.6   Simulation of the individual elements in the mixer

The initial step in the design procedure is to characterize the individual elements used in the mixer topology. The simulation results are expected to agree with expectations we have from the fundamental network theory based on components such as capacitors, inductors and resistors. We use a 2.5-D simulation environment called ADS Momentum to calculate S-parameters and thereby validate functionality of the key circuit elements.

6.6.1   Via-to-ground

Before we analyze and tune the component values, transmission line widths and lengths, we will first focus on the individual built-in components from D007 technology which are used in the final mixer design. One of these built-in components is the via-to-ground, which is used to provide electrical ground for the transistor source nodes at RF frequencies. The radius of the via-to-ground nodes is usually larger than the width of the transmission lines and therefore appearing parasitics can limit the frequency of operation. In Fig. 6.9(a) we see a layout drawing of a transmission line, drawn using "in" layer, that is $l = 100$ μm long and $w = 10$ μm wide and which is terminated using a via-to-ground component. We do not have to specify any values for the via-to-ground besides the width w of the connecting transmission line.

In Fig. 6.9 we see a characterization of the via-to-ground component available in D007 technology. It turned out that the component from the D007 package had a missing metal layer called "be" (bottom-electrode), so instead of being a short circuit at zero frequency (start at the most left in the Smith chart) it acted as an open circuit (start at the most right in the Smith chart). This mistake was corrected and a new component was created in order to use it for further circuit simulations.
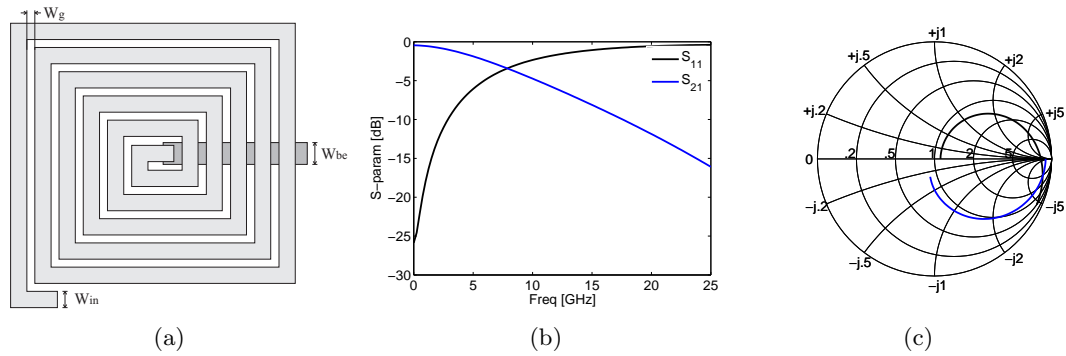
Figure 6.10: Inductor as a two-port device: (a) Outline of square shaped planar inductor; (b) S-parameter plot; (c) Smith chart plot.
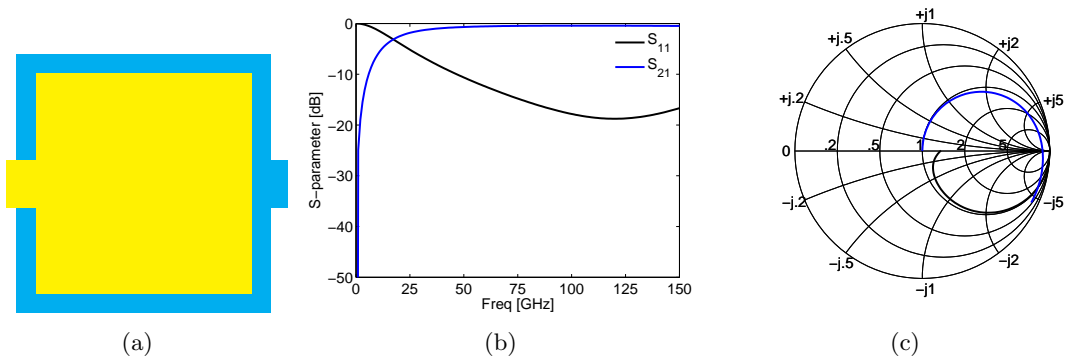

Figure 6.11: TCBEIN capacitor as a two-port device: (a) Outline of TCBEIN capacitor; (b) S-parameter plot; (c) Smith chart plot.

6.6.2   Inductor

For the inductor design we use planar spiral geometry shown in Fig. 6.10(a). In general inductors for MMIC purposes can assume many shapes, such as square, hexagonal, octagonal or circular. In this design we use square shaped inductors since they are available as a standard component. We need to specify four inductor parameters: the inductance (L), the gap width between the "in" lines (W_g) and the line width of the two metal layers W_{IN} and W_{BE}. The corresponding inductor strip length is computed from the inductance L. In Fig. 6.10 we present S-parameters of the inductor treating it as a two-port device. In Fig. 6.10(b) we see that the inductor provides considerable loss (from S_{21}) for frequencies larger than 20 GHz.

6.6.3   Small capacitor

In D007 technology we have two types of capacitors available. The type called TCBEIN can provide relatively small capacitance values in the range 1 fF < C < 1pF and is defined between "in" and "be" layers. The layout is shown in Fig. 6.11(a) and the two-port S-parameters are shown in Fig. 6.11.

6.6.4   Large capacitor

By lowering the dielectric thickness between two metal layers we can enlarge the total capacitance of the component. This is the idea behind the second type of the capaci-
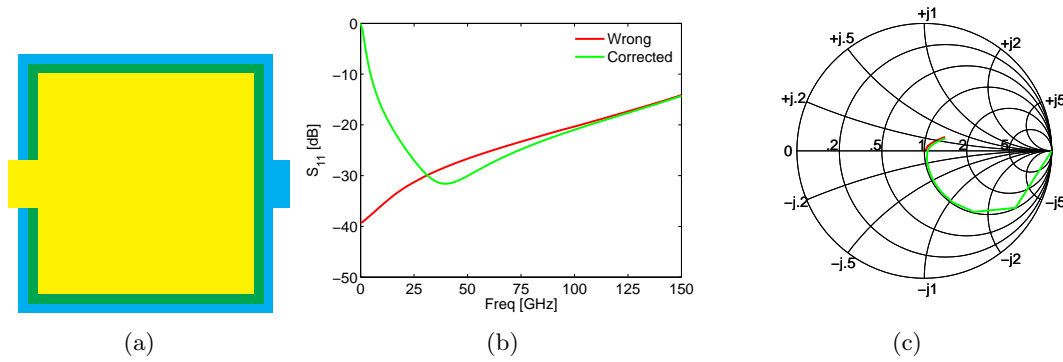
(a)   (b)   (c)

Figure 6.12: S_{11} parameter for TCBETE capacitor as a two-port device: (a) TCBETE capacitor;
(b) S-parameter plot; (c) Smith chart plot.

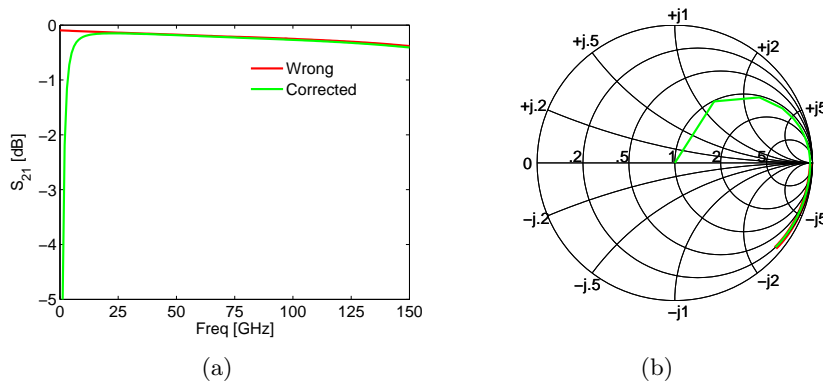(a)   (b)

Figure 6.13: S_{21} parameter for TCBETE capacitor as a two-port device: (a) S-parameter plot;
(b) Smith chart plot.

tor, the TCBETE capacitor, which is defined between "te" and "be" layers as shown in
Fig. 6.12(a). Thereby, the TCBETE capacitor can provide relatively large capacitance
values in the range 0.06pF < C < 50pF. For the TCBETE capacitor we encounter the
similar problem as for the via-to-ground: the capacitor was shorted in the Smith chart
for zero frequency when it was supposed to be an open circuit. This problem was solved
by redefining the layout layers in the ADS substrate layout definition. In Fig. 6.12 we see
wrong and corrected S_{11} parameters and similarly in Fig. 6.13 we see wrong and corrected
S_{21} parameters.

6.6.5   Marchand balun

A Marchand balun is designed and verified by EM simulations performed in ADS Momentum, the same environment as the depicted layout in Fig. 6.14. The analysis and
design procedure is based on the methods described in [36]. The widths and the lengths
of the quarter wavelength lines were optimized, due to their relatively simple geometry
and fast computing. The balun shows low insertion loss and a stable phase difference of
180 degrees, as sown in Fig. 6.15.
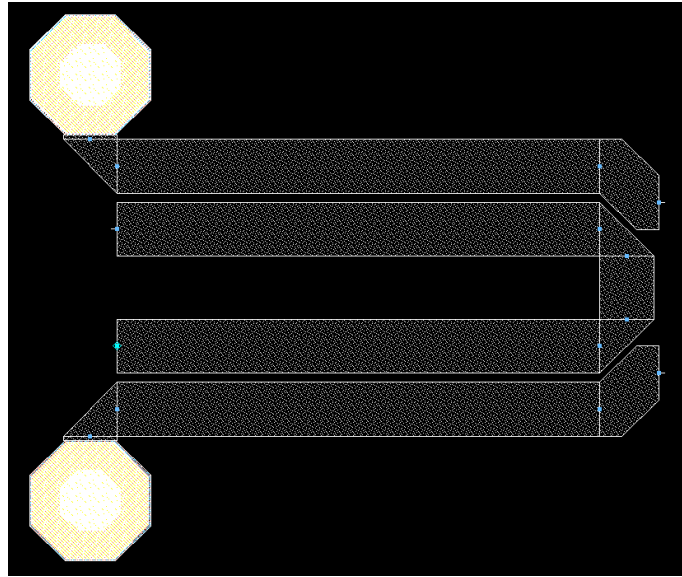
Figure 6.14: Marchand balun depicted from ADS layout window. The ground pads are relatively large compared to the width of the transmission lines.

     (a)   (b)
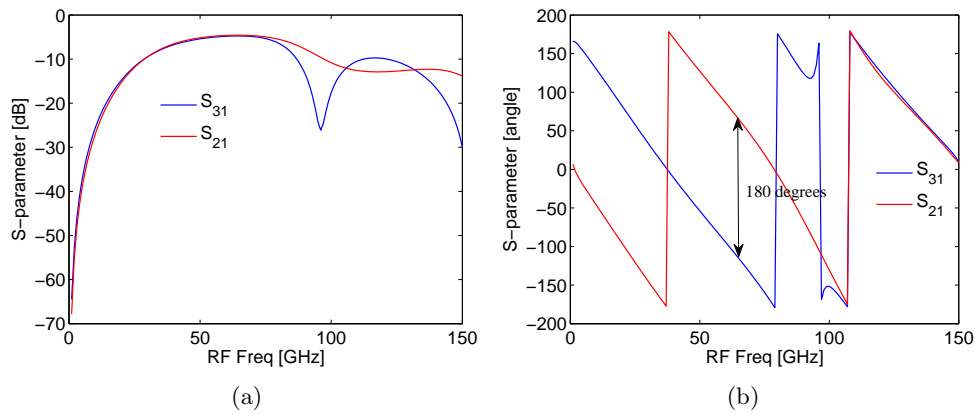
Figure 6.15: Marchand balun simulated in Momentum: (a) The magnitude from port 1 to ports 2 and 3, respectively; (b) The angle from port 1 to ports 2 and 3, respectively. The balun has approximately 4 dB loss at 65 GHz and a phase difference of approximately 180 degrees which we also aimed for.
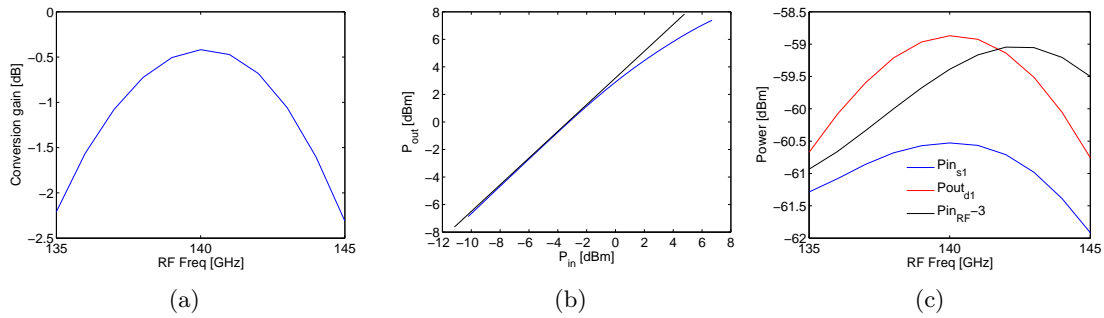
Figure 6.16: Simulations performed in ADS: (a) Conversion gain; (b) 1-dB gain compression; (c) Power balance across the nodes for one transistor.

6.7   Mixer simulations

The mixer design has been sent to OMMIC foundry for fabrication who uses technology based on mHEMT with GaAs compound as the substrate. The simulations of the mixer are performed in schematic window where all the vias and transmission lines are simulated beforehand. The process of frequency translation is calculated on principles of harmonic balance (HB) where we assume that the solution can be represented by a linear combination of sinusoidal functions in order to satisfy Kirchoff's law. This technique is widely used for non-linear elements in electrical circuits, such as diodes, transistors and other types of semiconductor junctions [49]. Furthermore, several optimization routines were applied in order to adjust circuit parameters and thereby get higher conversion gain. We used the corrected model for all vias and TCBETE capacitors during simulations of the mixer as a unit. The key parameters simulated are shown in Fig. 6.16. Conversion gain is, in the worst case, approximately -2 dB, see Fig. 6.16(a). The power starts to deviate from the linear growth at approximately 2 dBm, as shown in Fig.6.16(b). The power balance between the transistor nodes is shown in Fig.6.16(c). The RF input power, Pin_{RF}, is split between the two source inputs, ideally the input power to one of the source nodes is Pin_{RF}-3 [dBm]. We loose no more than 2 dB due to the coupling network at the source nodes. From the source to the drain we have a gain in the range from approximately 1 to 1.5 dB. The final layout of the subharmonic mixer is shown in Fig. 6.17. The mixer is sent to OMMIC for fabrication and the first samples are expected during March 2012.

6.8   Conclusions and further work

The subharmonic mixer design shows good performance in the conversion gain simulated in the range from -2 to 0 dB and 1-dB gain compression point around 2 dBm. Both properties make it suitable for applications in fusion plasma mm-wave diagnostic systems. The isolation between the LO and RF ports is found to be higher than 80 dB. The matching at the RF is mostly based on adjustments of the length and width of the transmission line that goes from source to ground and the AC coupling capacitor. Similarly, at the IF port we use adjustments and tuning of the RF choke inductor and AC coupling capacitor in order to maximize the conversion of the signal from 135 - 145 GHz (RF) to the 5 - 15 GHz (IF) port. Placement of further components at the RF and IF ports resulted in somewhat lower conversion gain while at the same time the flatness of the conversion gain was improved. Further simulations of the subharmonic mixer have shown that a source follower applied at the IF output node was able to boost the conversion gain by ∼3 dB
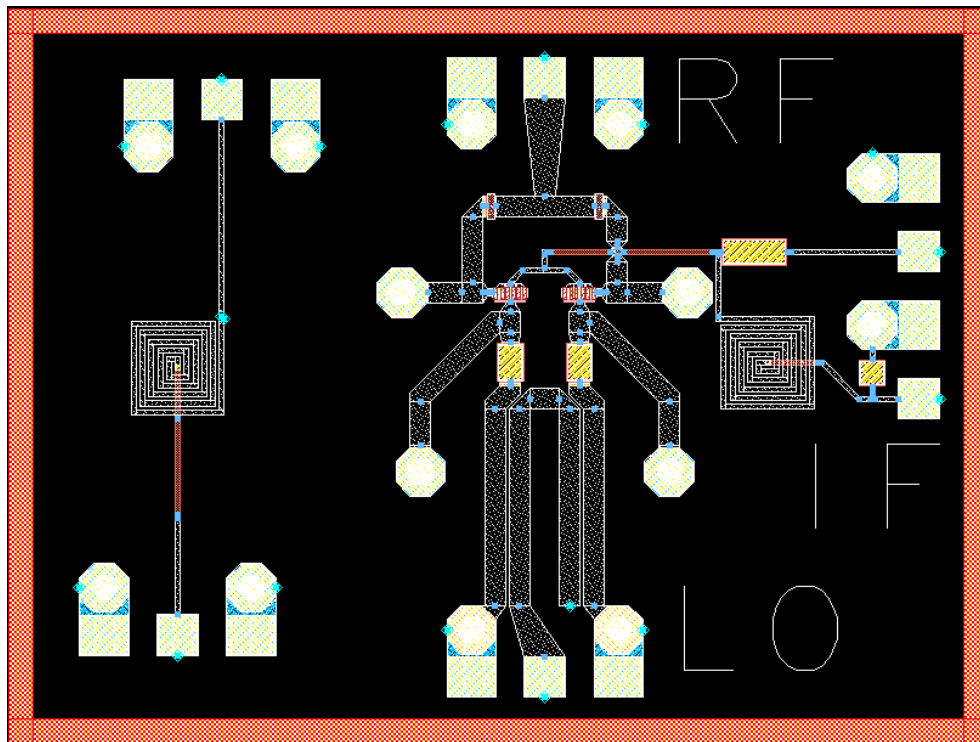
Figure 6.17: The 140 GHz subharmonic mixer topology depicted in ADS layout tool (right part). The blue dots show interface connections of the various components used in the design. There is one DC bias at the IF port where we use a capacitor to short-circuit high frequency noise from the test pad. A test setup to characterize an inductor with 2.6 nH inductance is also shown (left part). The layout has size 2×1.5 mm.

around 140 GHz and by $\sim$1 dB at the edges of the mixer design range 135 - 145 GHz.

Chapter 7

Summary and Future Work

Through this work we have demonstrated functionality and introduced improvements of the millimeter wave receivers used to detect scattered radiation in fusion plasmas. The frequency of operation is mainly in the D band, it spans from 100 to 110 GHz for CTS analysis and up to 145 GHz for NTM analysis. This work was primarily dedicated to millimeter wave receivers with the objective to detect scattered radiation associated to dynamics of fast ions.

Conceptual studies on ITER have shown that 60 GHz probing beam is sufficient to detect fast ions. We find it important to resolve the near parallel velocity components of the fast ion distribution in ITER. We have presented a compact solution of an antenna array that can be accommodated on the ITER HFS. The antenna array, consisting of a mirror assembly accompanied with a test horn, has been verified experimentally with a 1:1 mock-up.

The individual components of the CTS receiver at ASDEX Upgrade and their performance have been presented. The AUG receiver uses a heterodyne scheme, it converts input signals in the RF range from 100 to 110 GHz down to the IF range from 5 to 15 GHz using a mixer. We have measured losses in the range from 10 to 26 dB in the receiver RF line. One of the reasons for high losses is the notch filter that must be integrated into the receiver system in order to reject the strong probing beam. Extensive study on this topic is performed, and we are able to deliver notch filters with 1 GHz rejection bandwidth and more than 25 GHz passband bandwidth for multi gyrotron operations. Similarly, we can deliver notch filters with 150 MHz rejection bandwidth and more than 14 GHz passband bandwidth for single gyrotron operations. Both achievements are reported for the first time in the community of fusion diagnostics.

A mixer with small conversion loss is also desired in fusion experiments, since no amplifiers in the D-band are commercially available for plasma diagnostics. A way to keep the system noise figure low is to design a mixer with low conversion loss. We have designed a mixer for NTM applications with center frequency at 140 GHz, conversion loss simulated in the range from 0 to 2 dB, and 1-dB gain compression point around 2 dBm. The mixer layout proposal is sent to OMMIC foundry for fabrication.

The next step CTS receivers should use custom-made active components such as mixers, amplifiers, and VCVAs integrated in one unit with an interface that is easy to connect with solid structures such as waveguides. The most promising solutions use miniature patch antennas to couple fields from a microstrip line into a waveguide, a large research area at Chalmers University, and possibly, a step closer to supreme CTS receivers. Furthermore, a different way to improve mm-wave receiver is to design all the passive waveguide components in the RF line as a one large component. By this means,

we reduce easily insertion loss by 5 dB, since the imperfect junction interfaces between the components are no longer there. All RF components are needed during experiments, so by using an integrated RF branch flexibility of the receiver will degrade only slightly while modulation of the received signal will improve considerably.

Appendix A

Microwave Two-Port Network

A two-port network presented in the Fig. A.1 is the most common setup to measure electrical wave properties of an RF component, particulary when more complicated circuit systems need to be analyzed. Characterization of a two-port network prescribes that the two-port scattering parameters, S-parameters, are calculated. Dealing with RF circuits there are two basic approaches to two-port parameters, either scattering parameters - also called S-parameters - or the traditional admittance, impedance and hybrid types - Y,Z,H,G - of small-signal parameters. S-parameters relate a set of incident and reflected wave quantities that are defined in terms of port voltages and currents. They have the advantage of being relatively simple to measure at high frequencies. The more traditional parameter types constrain port voltages and currents by terminal conditions that are open or short circuits, and this is somewhat difficult to establish at high frequencies. In the following text we will define basic principles of the *generalized transmission line* and afterwards we will focus on derivation of the S-parameters for some fundamental circuit configurations.

A.0.1 A General Transmission Line

A uniform transmission line is defined by identical dimensions and electrical properties at all planes transverse to the direction of propagation. Also, we are able to apply AC circuit concepts to the lines whose lengths are not negligible compared to the operating wavelength. A general transmission line has both voltage and current waves propagating through the system. Defining the propagation constant as $\gamma = \alpha + j\beta$ we find the voltage and the current waves as

$$\mathbf{V} = \mathbf{V}_0^+ \exp(-\gamma z) + \mathbf{V}_0^- \exp(+\gamma z) = \mathbf{V}^+ + \mathbf{V}^- \tag{A.1}$$

$$\mathbf{I} = \mathbf{I}_0^+ \exp(-\gamma z) - \mathbf{I}_0^- \exp(+\gamma z) = \mathbf{I}^+ - \mathbf{I}^-. \tag{A.2}$$
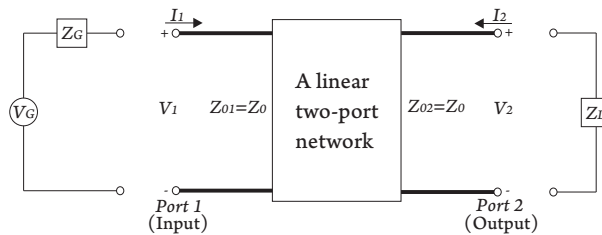

Figure A.1: A linear two-port network and its associated input and output quantities.
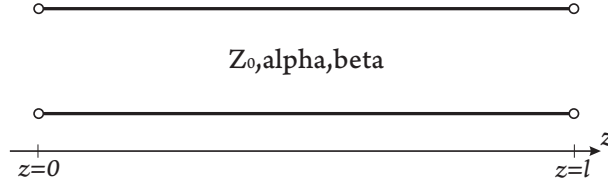
Figure A.2: A transmission line with length $z = l$.

The notation $\mathbf{V}^+(z = 0) = \mathbf{V}_0^+$ is the forward traveling voltage wave and $\mathbf{V}^-(z = 0) = \mathbf{V}_0^-$ is the backward traveling voltage wave, see Fig. A.2. Similarly, we have the same designation for the current traveling waves. Notice that both $\mathbf{V}$ and $\mathbf{I}$ are vectors and typically have a direction along the z-axis. The ratio of the forward to the backward voltage (or current) is defined as the reflection coefficient Γ

$$\Gamma \equiv \frac{\text{Backward voltage(or current) at pt. } z}{\text{Forward voltage(or current) at pt. } z} = \frac{\mathbf{V}^-}{\mathbf{V}^+} = \frac{\mathbf{I}^-}{\mathbf{I}^+} \tag{A.3}$$

The power across the transmission line is given as

$$P = \Re(\mathbf{V}\mathbf{I}^*). \tag{A.4}$$

Using the fact that $\mathbf{V}^+ = \mathbf{I}^+ Z_0$ and $\mathbf{V}^- = \Gamma\mathbf{V}^+$ then we find that

$$P = \Re\left[(1 - |\Gamma|^2 + \Gamma - \Gamma^*)\frac{(V^+)^2}{Z_0^*}\right], \tag{A.5}$$

where we used complex conjugate formalism $\Gamma\Gamma^* = |\Gamma|^2$ and $\mathbf{V}^+\mathbf{V}^{+*} = (V^+)^2$. In high frequency lines Z_0 can be considered as pure real and the above expression reduces to

$$P = P^+(1 - |\Gamma|^2) = P^+ - P^-, \tag{A.6}$$

since $\Gamma - \Gamma^*$ is imaginary. From the Eq. (A.6) we find that the ratio between the backward and forward power is the absolute voltage (or current) coefficient squared given as

$$P^- = |\Gamma|^2 P^+. \tag{A.7}$$

Another advantage of real Z_0 is the fact that $\mathbf{V}^+$ and $\mathbf{I}^+$ are in phase resulting in

$$P^+ = \frac{(V^+)^2}{Z_0} = \frac{(V_0^+)^2}{Z_0}\exp(-2\alpha z) \tag{A.8}$$

$$P^- = \frac{(V_0^+)^2}{Z_0}|\Gamma|^2\exp(-2\alpha z) \tag{A.9}$$

Using equations Eq. (A.8) and Eq. (A.9) we can determine the two-port scattering parameters from the physical quantities Z_0, Z_G and γ. But we still need to find an expression for the forward traveling voltage wave V_0^+. Applying Kirchhoff's voltage law at the input the forward voltage wave equation may be written as

$$\mathbf{V}_0^+ = \frac{\mathbf{V}_G(1 - \Gamma_G)}{2(1 - \Gamma_G\Gamma_L\exp(-2\gamma l))}. \tag{A.10}$$

The reflection coefficients at the generator Γ_G and the load Γ_L are defined as

$$\Gamma_G = \frac{Z_G - Z_0}{Z_G + Z_0} \text{ and } \Gamma_L = \frac{Z_L - Z_0}{Z_L + Z_0}. \tag{A.11}$$
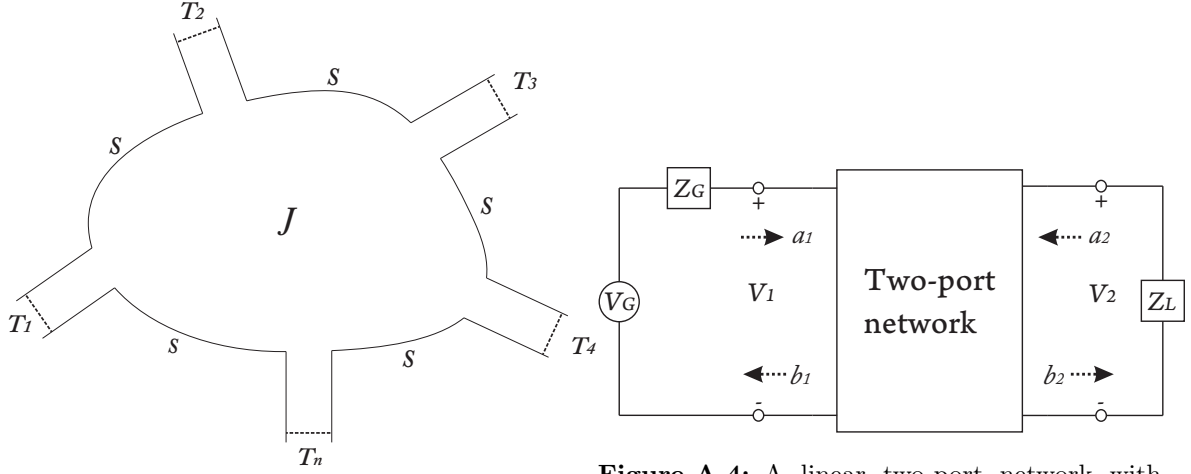
Figure A.3: Junction of n waveguides.

Figure A.4: A linear two-port network with generator and load impedances.

Thus, we can determine an expression for the forward power wave P^+ in terms of available generator power P_A and the reflection coefficients

$$P^+ = \frac{V_G^2}{4Z_0} \left| \frac{1 - \Gamma_G}{1 - \Gamma_G \Gamma_{in}} \right|^2 \exp\left(-2\alpha z\right) \tag{A.12}$$

where we use the *rms* value of the generator voltage $|\mathbf{V}_G|_{rms} = V_G$ which gives us V_0^+ in *rms* as well. Power incident on the input port can be found from the Eq. (A.6)

$$P_{in} = P_{in}^+(1 - |\Gamma_{in}|^2) \tag{A.13}$$

$$= P_A \frac{(1 - |\Gamma_G|^2)(1 - |\Gamma_{in}|^2)}{|1 - \Gamma_G \Gamma_{in}|^2} \tag{A.14}$$

where $P_A = \frac{V_G^2}{4R_G}$ is the available power of the generator. The net power delivered to the load is defined as

$$P_L = P_L^+(1 - |\Gamma_L|^2) \tag{A.15}$$

$$= P_A \frac{(1 - |\Gamma_G|^2)(1 - |\Gamma_{in}|^2)}{|1 - \Gamma_G \Gamma_{in} \exp\left(-2\gamma l\right)|^2} \exp\left(-2\alpha l\right). \tag{A.16}$$

A.0.2   S-Parameters

The importance of the S-parameters will be clarified in this section. The S-parameters are directly measured with a Network Analyzer and thereby extremely suitable to compare theory with practical work. The scattering N-port junction can, in general, be written as

$$\begin{bmatrix} V_1^- \\ V_2^- \\ \dots \\ V_N^- \end{bmatrix} = \begin{bmatrix} S_{11} & S_{12} & S_{13} & \dots & S_{1N} \\ S_{21} & S_{22} & S_{23} & \dots & S_{2N} \\ \dots & \dots & \dots & \dots & \dots \\ S_{N1} & S_{N2} & S_{N3} & \dots & S_{NN} \end{bmatrix} \begin{bmatrix} V_1^+ \\ V_2^+ \\ \dots \\ V_N^+ \end{bmatrix}, \tag{A.17}$$

or as

$$[\bar{V}^-] = [\bar{\bar{S}}][\bar{V}^+]. \tag{A.18}$$

The n-port junction consisting of n waveguides is illustrated in Fig. A.3.

A two-port S-parameter matrix is defined as

$$b_1(l_1) = S_{11}a_1(l_1) + S_{12}a_2(l_2) \tag{A.19}$$
$$b_2(l_2) = S_{21}a_1(l_1) + S_{22}a_2(l_2) \tag{A.20}$$

where the incident a_i and scattered b_i waves are defined as

$$a_i(x_i) = \frac{V_i^+(x_i)}{\sqrt{Z_{0i}}} \quad \text{and} \quad b_i(x_i) = \frac{V_i^-(x_i)}{\sqrt{Z_{0i}}}, \tag{A.21}$$

where V_i^- and V_i^+ represents the reflected and incident terminal voltage at port i, respectively. The input reflection at port 1 may be written as

$$S_{11} = \left.\frac{b_1(l_1)}{a_1(l_1)}\right|_{a_2(l_2)=0} = \left.\frac{V_1^-(l_1)}{V_1^+(l_1)}\right|_{V_2^+(l_2)=0}. \tag{A.22}$$

In terms of circuit impedances the input reflection is mostly known as

$$S_{11} = \frac{Z_{T1} - Z_{01}}{Z_{T1} + Z_{01}}, \tag{A.23}$$

where Z_{T1} is the input impedances at the port 1 of the two-port network considered. In the case where the two-port network is a transmission line with the characteristic impedance of Z_0, the input impedance seen from port 1 would be

$$Z_{T1} = Z_{02}\frac{Z_L + Z_{02}\tanh\gamma d}{Z_{02} + Z_L\tanh\gamma d}, \tag{A.24}$$

where d is the length of the transmission line considered and $\gamma = \alpha + j\beta$ is the propagation constant. Using the *Thévenin equivalent circuit* at port 1 the transmission parameter S_{21} from port 1 towards port 2 can be expressed as

$$S_{21} = \left.\frac{b_2(l_2)}{a_1(l_1)}\right|_{a_2(l_2)=0} = \frac{2\sqrt{Z_{01}}}{\sqrt{Z_{02}}}\frac{V_2(l_2)}{E_{1,TH}}, \tag{A.25}$$

where $E_{1,TH}$ is the *Thévenin equivalent voltage* across port 1.

The results achieved in Eq .(A.23) and Eq. (A.25) can be found for the reflection and transmission parameters at port 2 as well

$$S_{22} = \frac{Z_{T2} - Z_{02}}{Z_{T2} + Z_{02}} \quad \text{and} \quad S_{12} = \frac{2\sqrt{Z_{02}}}{\sqrt{Z_{01}}}\frac{V_1(l_1)}{E_{2,TH}}. \tag{A.26}$$

Since we are considering only two-ports in this thesis we will present few examples on how to calculate the S-parameters for some simple circuit configurations.

A.0.3 Example 1

Consider a series impedance Z as a two-port network, shown in Fig. A.5 and determine the 4 S-parameters S_{11}, S_{21}, S_{22} and S_{12}.

The input reflection at the port 1, S_{11}, can be found from Eq. (A.23) noting that $Z_{T1} = Z + Z_{02}$

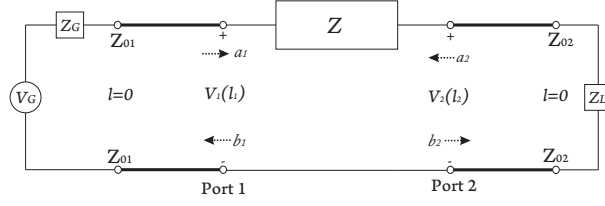$$S_{11} = \frac{Z + Z_{02} - Z_{01}}{Z + Z_{02} + Z_{01}}. \tag{A.27}$$

Figure A.5: Series impedance Z as a two-port network.

Inside a network analyzer all the line characteristic impedances are matched and real $Z_{01} = Z_{02} = Z_0$ and usually equal to 50Ω. If we just consider matched line, we find

$$S_{11} = \frac{Z}{Z + 2Z_0}. \tag{A.28}$$

The reflection at the port 2 S_{22} is similarly found using $Z_{T2} = Z + Z_{01}$

$$S_{22} = \frac{Z + Z_{01} - Z_{02}}{Z + Z_{01} + Z_{02}}, \tag{A.29}$$

$$= \frac{Z}{Z + 2Z_0}. \tag{A.30}$$

In the last expression we used the matched impedance lines $Z_{01} = Z_{02} = Z_0$ and, accordingly, the input reflection at port 1 and port 2 is the same. This is the truth for both the amplitude and phase of S_{11} and S_{22}. The result is obvious since a two-port network consisting of only one component will always be symmetrical with respect to voltages and current across the nodes. This is also the truth for the transmission parameters $S_{12} = S_{21}$. Assuming matched impedance lines at both ports, we will calculate S_{21} with a voltage wave incident on port 1. The voltage at port 2 is found by Ohms law

$$V_2(l_2) = \frac{E_{1,TH} Z_0}{Z + 2Z_0}. \tag{A.31}$$

Using Eq. (A.25) we find

$$S_{21} = \frac{2V_2(l_2)}{E_{1,TH}} = \frac{2Z_0}{Z + 2Z_0}. \tag{A.32}$$

We have now calculated all the S-parameters. If we assume that $Z = Z_0$, we find that

$$S = \begin{pmatrix} 1/3 & 2/3 \\ 2/3 & 1/3 \end{pmatrix} \tag{A.33}$$

These values are actually poor for a S-parameter matrix. A two-port network consisting of an impedance of Z_0 just makes a primitive voltage division with poor transmission and somewhat high reflection. Later we will see that the only way to improve the scattering properties is to lower all the series impedances and all the shunt conductances in the entire two-port network. In current example this would mean that $Z = 0$ so the two-port S-parameters become

$$S = \begin{pmatrix} 0 & 1 \\ 1 & 0 \end{pmatrix}, \tag{A.34}$$

which are the ideal scattering parameters. The voltage wave is fully transmitted, i.e. nothing is reflected from the two-port network.

We can develop further our two-port system by including a shunt conductance and a series impedance. The calculations on this schematic will be presented in the following example.
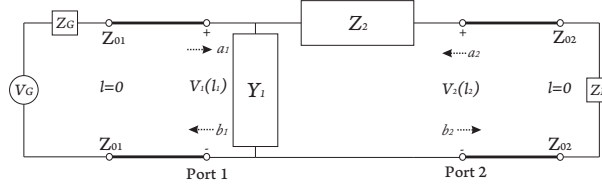
Figure A.6: L-type two-port network.

A.0.4   Example 2

Consider an L-type two-port network consisting of an admittance $Y_1 = \frac{1}{Z_1}$ and impedance Z_2 shown in Fig. A.6. Determine the scattering matrix of this two-port. We can determine the input admittance at port 1

$$Y_{T1} = Y_1 + (Z_2 + Z_{02})^{-1}. \tag{A.35}$$

The current at port 1 is found by voltage division

$$I_1(l_1) = -\frac{E_{1,TH}}{Z_{01} + Y_{T1}^{-1}}. \tag{A.36}$$

Furthermore, the node voltages at port 1 and 2 are found as

$$\frac{V_1(l_1) - E_{1,TH}}{Z_{01}} = I_1(l_1) \quad \text{and} \quad \frac{V_2(l_2) - V_1(l_1)}{Z_2} = \frac{V_2(l_2)}{Z_{02}}. \tag{A.37}$$

The Eq. (A.36) and Eq. (A.37) are sufficient to determine the transmission from port 1 towards port 2, S_{21}. The port 1 voltage $V_1(l_1)$ and current $I_1(l_1)$ can be eliminated leaving $V_2(l_2)$ and $E_{1,TH}$ as a stand alone ratio in terms of impedances in the network. Eliminating the current at the port 1 I_1, we find

$$V_1(l_1) = E_{1,TH}\left(1 - \frac{Z_{01}}{Z_{01} + Y_{T1}^{-1}}\right) \quad \text{and} \quad V_2(l_2) = \frac{V_1(l_1)}{Z_2}\left(\frac{1}{Z_2} + \frac{1}{Z_{02}}\right)^{-1}. \tag{A.38}$$

Eliminating the voltage V_1 at port 1 in the expression above and using Eq. (A.25), we find the transmission parameter from port 1 to port 2 to be

$$\begin{aligned} S_{21} &= \frac{2\sqrt{Z_{01}}}{\sqrt{Z_{02}}}\frac{V_2(l_2)}{E_{1,TH}} \\ &= \frac{2\sqrt{Z_{01}}}{\sqrt{Z_{02}}}\left(1 - \frac{Z_{01}}{Z_{01} + Y_{T1}^{-1}}\right)\left(1 + \frac{Z_2}{Z_{02}}\right)^{-1}. \end{aligned} \tag{A.39}$$

Assuming matched line case $Z_0 = Z_{01} = Z_{02}$, then Eq. (A.39) may be written as

$$\boxed{S_{21} = \frac{2Z_0}{Y_1(Z_2 + Z_0)Z_0 + 2Z_0 + Z_2}.} \tag{A.40}$$

If we assume $Y_1 = 0$ we end up with a single impedance two-port network and this is what we have in Eq. (A.32). Similar calculations can be derived if we apply a Thévenin equivalent circuit at the port 2. The calculations are very similar to those presented above, so we will simply state the result

$$\begin{aligned} S_{12} &= \frac{2\sqrt{Z_{02}}}{\sqrt{Z_{01}}}\frac{V_1(l_1)}{E_{2,TH}} \\ &= \frac{2\sqrt{Z_{02}}}{\sqrt{Z_{01}}}\frac{1}{(Z_{02} + Z_{T2})(Z_{01}^{-1} + Y_1)} \end{aligned} \tag{A.41}$$

where $Z_{T2} = Z_2 + (Z_{01}^{-1} + Y_1)^{-1}$ is the impedance seen from the port 2. Assuming matched transmission lines at input and output $Z_0 = Z_{01} = Z_{02}$, we find that

$$S_{21} = \boxed{\frac{2Z_0}{2Z_0 + Z_2 + Y_1 Z_0 (Z_2 + Z_0)}}. \tag{A.42}$$

Note that $S_{12} = S_{21}$ which tells us that the circuit is reciprocal. This is a fundamental property for all passive circuits not containing any external sources or ferromagnetic materials. The reflection loss at the input S_{11} is calculated using Eq. (A.23)

$$
\begin{aligned}
S_{11} &= \frac{Z_{T1} - Z_{01}}{Z_{T1} + Z_{01}} \\
&= \frac{(Y_1 + (Z_2 + Z_{02})^{-1})^{-1} - Z_{01}}{(Y_1 + (Z_2 + Z_{02})^{-1})^{-1} + Z_{01}}
\end{aligned}
\tag{A.43}
$$

Again, assuming matched line case $Z_0 = Z_{01} = Z_{02}$, Eq. (A.43) becomes

$$S_{11} = \boxed{\frac{Z_2 - Z_0 Y_1 (Z_2 + Z_0)}{Z_2 + 2Z_0 + Z_0 Y_1 (Z_2 + Z_0)}}. \tag{A.44}$$

If we assume $Y_1 = 0$ we find a single component two-port network we expressed in Eq. (A.30). Similarly, the reflection at the port 2 can be found from Eq. (A.26)

$$
\begin{aligned}
S_{22} &= \frac{Z_{T2} - Z_{02}}{Z_{T2} + Z_{02}} \\
&= \frac{Z_2 + (Z_{01}^{-1} + Y_1)^{-1} - Z_{02}}{Z_2 + (Z_{01}^{-1} + Y_1)^{-1} + Z_{02}}
\end{aligned}
\tag{A.45}
$$

Assuming matched line case, the Eq. (A.45) becomes

$$S_{22} = \boxed{\frac{Z_2 + Z_0 Y_1 (Z_2 - Z_0)}{Z_2 + 2Z_0 + Z_0 Y_1 (Z_2 + Z_0)}}. \tag{A.46}$$

If we make a similar evaluation for S_{11} by assuming $Y_1 = 0$, we will find identical reflections at both ports. Another way to confirm our calculation is to assume $Z_2 = 0$. Then we find

$$S_{11}|_{Z_2=0} = S_{22}|_{Z_2=0} = \frac{-Z_0 Y_1}{2 + Z_0 Y_1}. \tag{A.47}$$

This result is also what could be expected due to symmetry when Z_2 is neglected. Notice that the S-parameters S_{11} and S_{22} are in general different in both amplitude and phase regardless of the circuit being lossless or not. Only symmetrical circuits can fulfill $S_{11} = S_{22}$. The results in the boxed equations are convenient to memorize for general circuit analysis using S-parameters.

Further in this thesis the terms such as *Insertion Loss* and *Return Loss* are used. These terms are closely related to the S-parameters, so they are introduced in the following section.

The insertion loss of a two-port network is defined as[65, p.170]

$$IL \equiv 10 \log \frac{P_{Lb}}{P_{La}} \quad [dB], \tag{A.48}$$

where P_{Lb} is the power delivered to a specified load (Z_L) *before* inserting the network and P_{La} is the power delivered to the *same* load after inserting the network. In terms of the S-parameters insertion loss becomes

$$IL = 10\log\{\frac{|(1 - S_{11}\Gamma_G)(1 - S_{22}\Gamma_L) - S_{12}S_{21}\Gamma_G\Gamma_L|^2}{|S_{21}|^2|1 - \Gamma_G\Gamma_L|^2}\} \qquad (A.49)$$

Similarly, return loss is defined by the Eq. (A.7)

$$RL \equiv 10\log\frac{P^+}{P^-} = 10\log\frac{1}{|\Gamma|^2} \quad [dB]. \qquad (A.50)$$

At the input of a two-port network we have $\Gamma = \Gamma_{in}$ and at the output we have $\Gamma = \Gamma_{out}$. The return loss at the input and output ports are found to be[65, p.170]

$$RL_{in} = \log\{|S_{11} + \frac{S_{12}S_{21}\Gamma_L}{1 - S_{22}\Gamma_L}|^{-2}\} \quad \text{and} \quad RL_{out} = \log\{|S_{22} + \frac{S_{12}S_{21}\Gamma_G}{1 - S_{11}\Gamma_G}|^{-2}\}. \quad (A.51)$$

Assuming perfect match at the input and output, i.e. $\Gamma_G = 0$ and $\Gamma_L = 0$, the insertion loss becomes

$$\underline{IL} = 10\log\frac{1}{|S_{21}|^2} = \underline{-20\log|S_{21}|}. \qquad (A.52)$$

For the same conditions $|S_{12}|^2$ represents *reverse* insertion loss and is found by placing the load at the input and source at the output.
Similarly, assuming perfect match at both ports return loss becomes

$$\underline{RL_{in}} = \log\{|S_{11}|^{-2}\} = \underline{-20\log|S_{11}|} \quad \text{and} \qquad (A.53)$$

$$\underline{RL_{out}} = \log\{|S_{22}|^{-2}\} = \underline{-20\log|S_{22}|}. \qquad (A.54)$$

For pure passive circuits the insertion loss is symmetrical ($S_{21} = S_{12}$) if all the ports are perfectly matched. This is not necessarily the case for return loss, but the symmetry can be achieved ($S_{11} = S_{22}$) if electrical properties of the two-port circuit are symmetrical. This has already been discussed in the two previous examples.
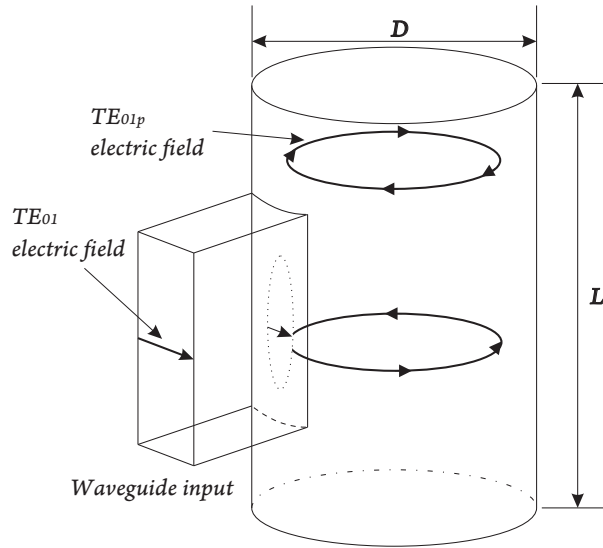
Figure A.7: Aperture coupling for TE_{mnp} cavity modes.

A.1   Representation of Waveguide Discontinuities

Waveguide structures are composite regions containing uniform- and nonuniform waveguides combined with discontinuity regions. The latter are regions wherein there exist discontinuities in cross-sectional shape. The discontinuities may occur along the waveguide structure or at the junction of waveguide regions. The fields within each of the waveguide regions are usually completely described by only a single propagating mode. However, for the discontinuities the complete description of the fields generally requires, in addition to dominant propagating mode, an infinity of non-propagating modes. It is well-known that a single waveguide can be represented by a single transmission line appropriate to the propagating mode, so it might be expected that the discontinuity regions require an infinity of transmission lines. This expectation is true, but also unnecessarily complicated. In the book by Marcuvitz [50] it is shown that the non-propagating nature of the higher-mode transmission lines restricts the complication in the field description to the instant vicinity of the discontinuity. Therefore, the discontinuity fields can be effectively regarded as lumped. Further in the book by Marcuvitz it is shown that voltage-current discontinuities can be represented by means of lumped-constant equivalent circuits. In the following we will use model equations derived in [50]. In the Fig. A.7 we see one approach to couple a transmission line to a resonator structure, here a cylindrical type. In the following two types of discontinuities will be presented. Both types are essential for band-reject waveguide filter construction that is used to remove the stray radiation coming from the gyrotron.

A.1.1   Slit-Coupled T-junction

A slit coupled notch filter is constructed as a symmetrical right-angle T-type junction of two (or more) rectangular guides of unequal heights, but equal widths, coupled by a small slit in a wall of zero thickness [50, pp.351-352]. This kind of very thin wall is also known as *iris*. The geometry is presented in Fig. A.9
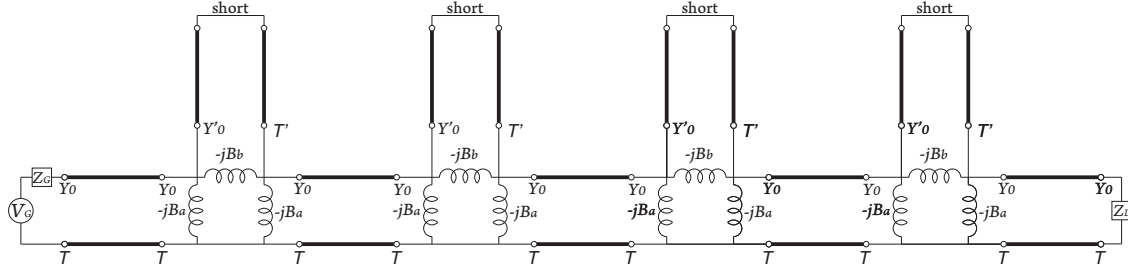
Figure A.8: The equivalent electrical circuit for a 4 pole Band-reject filter.

(a) General view   (b) Side view   (c) Eqivalent circuit
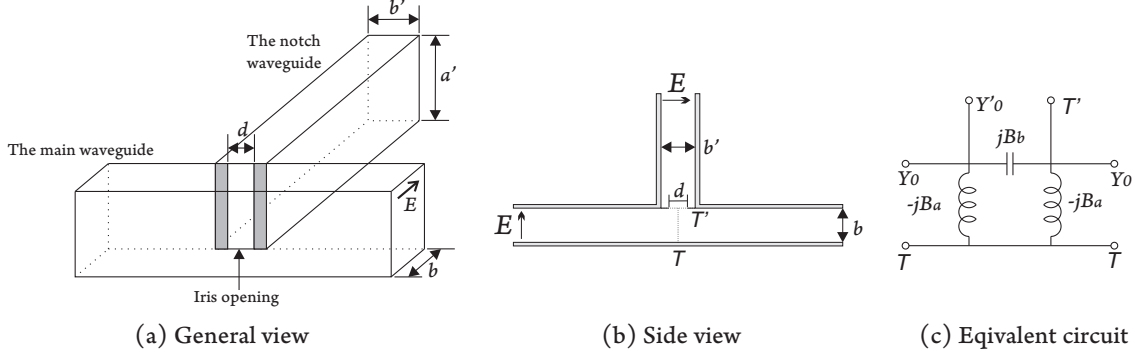
Figure A.9: The capacitive slit coupling mechanism.

$$\frac{B_a}{Y_0} = \frac{\frac{b}{\lambda_g}\left(\frac{\pi d}{4b}\right)^2}{1 + \frac{1}{6}\left(\frac{\pi d}{4b}\right)^2\left\{\left(\frac{b}{b'}\right)^2 + \frac{1}{2} + 6\left[1 - \sqrt{1-\left(\frac{2b}{\lambda_g}\right)^2}\right] + 12\left(\frac{b}{b'}\right)^2\left[\frac{1}{\sqrt{1-\left(\frac{2b'}{\lambda_g}\right)^2}} - 1\right]\right\}}$$
(A.55)

$$\frac{B_a}{Y_0} \approx \frac{b}{\lambda_g}\left(\frac{\pi d}{4b}\right)^2, \quad d \ll b,$$
(A.56)

The guide wavelength λ_g of the rectangular waveguide is given as

$$\lambda_g = \frac{\lambda}{\sqrt{1-\left(\frac{\lambda}{2a}\right)^2}},$$
(A.57)

where a is the waveguide width, so that $a > b$. Similarly, for B_b we have

$$\frac{B_b}{Y_0} - \frac{B_a}{2Y_0} = \frac{4b}{\lambda_g}\left\{\ln\frac{2\sqrt{2bb'}}{\pi d} + \frac{1}{2}\sum_{n=1}^{\infty}\left[\frac{1}{\sqrt{n^2-\left(\frac{2b}{\lambda_g}\right)^2}} - \frac{1}{n}\right]\right\},$$
(A.58)

$$\frac{B_b}{Y_0} \approx \frac{4b}{\lambda_g}\left[\ln\frac{2\sqrt{2bb'}}{\pi d} + \left(\frac{b}{\lambda_g}\right)^2\right], \quad b \ll \lambda_g$$
(A.59)

The restrictions using the results shown above is that equivalent circuit is applicable in the wavelength range $2b/\lambda_g < 1$ provided the slit dimension d is small compared with the wavelength. All the equivalent circuit parameters are derived by an integral equation method.
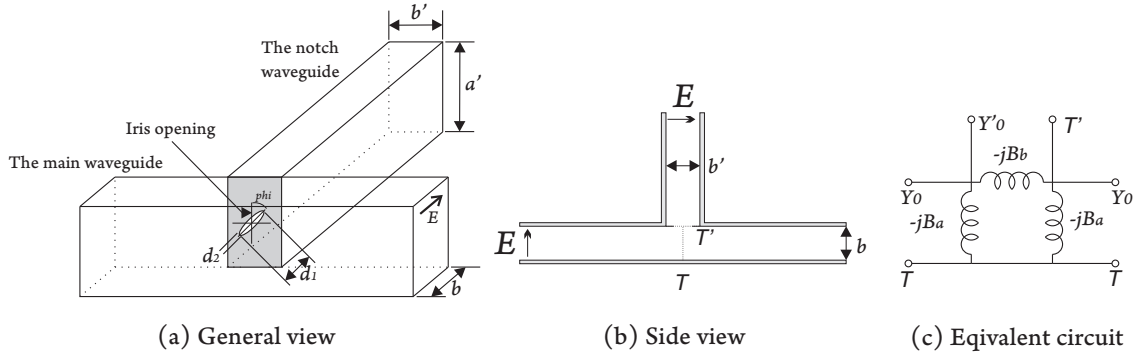
(a) General view   (b) Side view   (c) Eqivalent circuit

Figure A.10: The inductive iris aperture coupling mechanism.

A.1.2   Aperture-Coupled T-junction

Instead of coupling two waveguides with a slit, which is elongated with the height of the original waveguide, there is also possibility of coupling with an elliptical or circular aperture that is electrically smaller than slit-coupler. The aperture coupling has a nature of an iris, so that the metallic wall between the waveguides has zero thickness[50, pp.365-366].

At the reference planes T and T' for the case of coupling by a centered elliptical aperture oriented as shown in Fig. A.10, we find following parameters

$$\frac{Y_0'}{Y_0} = \frac{\lambda_g ab}{\lambda_g' a'b'} \tag{A.60}$$

$$\frac{B_a}{Y_0} = \frac{\frac{2\pi P}{\lambda_g ab}\left(\frac{\lambda_g}{\lambda}\right)^2}{1 - \frac{2\pi P}{\lambda_g ab}} \tag{A.61}$$

$$\frac{B_a}{Y_0} \approx \frac{2\pi P}{\lambda_g ab}\left(\frac{\lambda_g}{\lambda}\right)^2, \quad \text{if } \frac{d_1}{\lambda} \ll 1, \tag{A.62}$$

$$\frac{B_b}{Y_0} = \frac{\lambda_g ab}{4\pi}\left[\frac{1}{M} - \left(\frac{\pi}{a^2 b} + \frac{2\pi}{a'^2 b'}\right)\right], \tag{A.63}$$

$$\frac{B_b}{Y_0} \approx \frac{\lambda_g ab}{4\pi M}, \quad \text{if } \frac{d_1}{\lambda} \ll 1, \tag{A.64}$$

where

$$M = M_1 \cos^2\phi + M_2 \sin^2\phi, \tag{A.65}$$

$$P = \frac{d_1 d_2^2}{12} \cdot \frac{\pi}{2}\frac{1}{E(\epsilon)}, \tag{A.66}$$

$$P \approx \frac{\pi}{24}d_1 d_2^2, \quad \text{if } \frac{d_2}{d_1} \ll 1, \tag{A.67}$$

while the expressions for λ_g and λ_g' with $a = a'$ are given in eq.(A.57). The expressions

for M_1 and M_2 are defined by

$$M_1 = \frac{d_1^3}{6} \frac{\pi}{4} \frac{\epsilon^2}{F(\epsilon) - E(\epsilon)}, \tag{A.68}$$

$$M_2 = \frac{d_1 d_2^2}{6} \frac{\pi}{4} \frac{\epsilon^2}{E(\epsilon) - (1 - \epsilon^2)F(\epsilon)} \tag{A.69}$$

$$\epsilon = \sqrt{1 - \left(\frac{d_2}{d_1}\right)^2}, \tag{A.70}$$

and $F(\epsilon)$ and $E(\epsilon)$ are complete elliptic integrals of the first and second kinds, respectively. For the special case of a circular aperture $d_1 = d_2 = d$ we have from (A.65) and (A.66)

$$M = \frac{d^3}{6} \quad \text{and} \quad P = \frac{d^3}{12}. \tag{A.71}$$

The equations describing both coupling methods have some restrictions too. In the small-aperture range $d_1/\lambda \ll 1$ the equivalent circuit of Fig. A.9 is applicable at wavelengths for which only a single dominant H_{10}-mode can be propagated in both waveguides. Also, it should be emphasized that the above results apply to apertures in walls of zero thickness. For any waveguide coupling mechanism the maximum aperture dimension should be half compared to the guide wavelength λ_g.

Appendix B

List of AUG CTS channels

Detailed information on center IF, RF and 3-dB bandwidth BW_{3dB} for all 50 channels available in the CTS receiver at ASDEX Upgrade.

Channel no.	IF [GHz]	RF [GHz]	Specified 3-dB bandwidh [MHz]
1	5.0	100.5	1000
2	5.75	101.25	500
3	6.25	101.75	500
4	6.75	102.25	500
5	7.25	102.75	500
6	7.55	103.05	100
7	7.65	103.15	100
8	7.75	103.25	100
9	7.85	103.35	100
10	7.95	103.45	100
11	8.05	103.55	100
12	8.15	103.65	100
13	8.25	103.75	100
14	8.35	103.85	100
15	8.45	103.95	100
16	8.55	104.05	100
17	8.65	104.15	100
18	8.75	104.25	100
19	8.85	104.35	100
20	8.95	104.45	100
21	9.05	104.55	100
22	9.15	104.65	100
23	9.25	104.75	100
24	9.35	104.85	100
25	9.45	104.95	100
26	9.55	105.05	100
27	9.65	105.15	100
28	9.75	105.25	100
29	9.85	105.35	100
30	9.95	105.45	100

Channel no.	IF [GHz]	RF [GHz]	Specified 3-dB bandwidth [MHz]
31	10.05	105.55	100
32	10.15	105.65	100
33	10.25	105.75	100
34	10.35	105.85	100
35	10.45	105.95	100
36	10.55	106.05	100
37	10.65	106.15	100
38	10.75	106.25	100
39	10.85	106.35	100
40	10.95	106.45	100
41	11.05	106.55	100
42	11.15	106.65	100
43	11.25	106.75	100
44	11.35	106.85	100
45	11.45	106.95	100
46	11.75	107.25	500
47	12.25	107.75	500
48	12.75	108.25	500
49	13.25	108.75	500
50	14.0	109.50	1000

Bibliography

[1] C. A. BALANIS. *Advanced Engineering Electromagnetics*. John Wiley & Sons, 111 River Street, Hoboken, NJ 07030, 1989.

[2] C. A. BALANIS. *Antenna Theory*. John Wiley & Sons, 111 River Street, Hoboken, NJ 07030, 3 edition, 2005.

[3] R. BEHN *et al.* Ion temperature-measurement of tokamak plasmas by collective Thomson scattering of d2o laser-radiation. *Phys. Rev. Lett.*, 62:2833–2836, 1989.

[4] H. A. BETHE. Lumped constants for small irises. *M.I.T. Radiation Laboratory, Cambridge, Massachusetts*, Report 43-22, 1943.

[5] H. BINDSLEV. Three wave mixing and thomson scattering in plasmas. *Plasma Phys. Control. Fusion*, 35:1615–1640, 1993.

[6] H. BINDSLEV *et al.* Fast-ion velocity distributions in JET measured by collective Thomson scattering. *Phys. Rev. Lett.*, 83:3206–3209, 1999.

[7] H. BINDSLEV *et al.* Feasibility study of fast ion diagnosis in ITER by collective Thomson scattering millimeter waves to co2 laser. *Rev. Sci. Instrum.*, 75:3598–3600, 2004.

[8] H. BINDSLEV *et al.* Fast-ion dynamics in TEXTOR measured by collective Thomson scattering. *Phys. Rev. Lett.*, 97:205005, 2006.

[9] A. A. BOGDASHOV, G. G. DENISOV, D. A. LUKOVNIKOV, Y. V. RODIN, and A. N. PANIN. Resonant notch filters based on rectangular waveguide extensions. *Int. J. Infrared Millimeter Waves*, pages 1029–1032, 2002.

[10] T. J. M. BOYD and J. J. SANDERSON. *The Physics of Plasmas*. Cambridge University Press, The Edinburgh Building, Cambridge CB2 8RU, UK, 2005.

[11] Kai CHANG. *Handbook of Microwave and Optical Components*, volume 1. John Wiley & Sons, Brooklyn, N.Y., 1989.

[12] E. M. CHOI *et al.* Megawatt power level 120 GHz gyrotrons for ITER start-up. *J. Phys.: Conf. Series*, 25(1):1, 2005.

[13] A.E. COSTLEY *et al.* Measurement requirements and the diagnostic system on iter: Modifications following the design review. *Proc. 22nd IAEA Conf.*, 2008.

[14] E. de la LUNA and JET-EFDA contributors. Physics of ECE temperature measurements and prospects for ITER. In *An International Conference on BURNING PLASMA DIAGNOSTICS*, pages 63–72. American Institute of Physics, September 2007.

[15] G. G. DENISOV, A. A. BOGDASHOV, A. N. PANIN, and YU. V. RODIN. Design and test of new millimeter wave notch filter for plasma diagnostics. In *33rd International Conference on Infrared, Millimeter and Terahertz Waves*, pages 1–2. Int. J. Infrared Millimeter Waves, September 2008.

[16] G. G. DENISOV, S. V. KUZIKOV, and D. A. LUKONIKOV. Simple millimeter-wave notch filters based on rectangular wave-guide extensions. *Int. J. Infrared Millimeter Waves*, 16(7):1231–1238, 1995.

[17] G. G. DENISOV, S. V. KUZIKOV, and M. Y. SHMELYOV. Quasi-optical narrow-band notch filters. *Int. J. Infrared Millimeter Waves*, 2104:353–354, 1993.

[18] G. G. DENISOV *et al.* Millimeter wave multi-mode transmission line components. *Int. J. Infrared Millimeter Waves*, 32(3):343–357, 2011.

[19] N.J. DOBBE *et al.* Control and RF-transmission in the ECW system on TEXTOR-94. *Fusion Eng. Des.*, 56-57:599–604, 2001.

[20] YU. DRYAGIN, N. SCALYGA, and T. GEIST. A notch filter for 140 GHz microwave radiation. *Int. J. Infrared Millimeter Waves*, 17(7):1199–1204, 1996.

[21] J. EGEDAL, H. BINDSLEV, R.V. BUDNEY, and P. WOSKOV. Impact of beam ions on alpha-particle measurements by collective Thomson scattering in ITER. *Nucl. Fusion*, 45(3):191–200, 2005.

[22] K. FELCH *et al.* Recent ITER-relevant gyrotron tests. In *Third IAEA Technical Meeting on ECRH Physics and Technology in ITER*, pages 13–23. J. Phys.: Conf. Series, May 2005.

[23] V. FURTULA *et al.* Broadband notch filter design for millimeter-wave plasma diagnostics. *Rev. Sci. Instrum.*, 81:10D913, 2010.

[24] V. FURTULA *et al.* 105 GHz notch filter design for collective Thomson scattering. *Fusion Sci. Tech.*, 59:670–677, 2011.

[25] V. FURTULA *et al.* Design and performance of the collective thomson scattering receiver at ASDEX Upgrade. *Rev. Sci. Instrum.*, 83:013507, 2012.

[26] T. GEIST and M. BERGBAUER. Waveguide band-stop filters for 70 and 140 GHz. *Int. J. Infrared Millimeter Waves*, 15(12):2043–2049, 1994.

[27] P. F. GOLDSMITH and H. SCHLOSSBERG. A quasi-optical single sideband filter employing a semiconfocal resonator. *IEEE Transactions on Microwave Theory and Techniques*, 28(10):1136–1139, 1980.

[28] V. L. GRANATSTEIN and I. ALEXEFF. *High-Power Microwave Sources*. Artech House, Norwood, MA 02062, 1987.

[29] J. P. GRAVES *et al.* Control of magnetohydrodynamic stability by phase space engineering of energetic ions in tokamak plasmas. *Nature Communications*, 3(624), 2012.

[30] A. GUDE, S. GÜNTER, S. SESNIC, and ASDEX Upgrade Team. Seed island of neoclassical tearing modes at ASDEX Upgrade. *Nucl. Fusion*, 39(1):127, 1999.

[31] STEN E. GUNNARSSON. *Mixers and Multifunctional MMICs for Millimeter-Wave Applications*. PhD thesis, Chalmers University of Technology, Gothenburg, Sweden, 2008.

[32] S. GÜNTER *et al.* and the ASDEX Upgrade Team. Neoclassical tearing modes on ASDEX Upgrade: improved scaling laws, high confinement at high β_N and new stabilization experiments. *Nucl. Fusion*, 43(3):161, 2003.

[33] H. J. HARTFUSS, T. GEIST, and M. HIRSCH. Heterodyne methods in millimetre wave plasma diagnostics with applications to ECE, interferometry and reflectometry. *Plasma Phys. Control. Fusion*, 39(11):1693–1769, 1997.

[34] D. van HOUTTE *et al.* Recent fully non-inductive operation results in Tore Supra with 6 min, 1 GJ plasma discharges. *Nucl. Fusion*, 44(5):L11–L15, 2004.

[35] Heating ITER Physics Expert Group on Energetic Particles and Current Drive. ITER physics basis, ch. 5: Physics of energetic ions. *Nucl. Fusion*, 39(12):2471–2495, 1999.

[36] T. K. JOHANSEN and V. KROZER. Analysis and design of lumped element marchand baluns. In *17th International Conference on Microwaves, Radar and Wireless Communications (MIKON)*, pages 1–4. IEEE Micr., Radar and Wireless Com., May 2008.

[37] T. K. JOHANSEN *et al.* A high conversion-gain Q-Band InP DHBT subharmonic mixer using LO frequency doubler. *IEEE Trans. on Micr. Th. and Tech.*, 56(3):613–619, 2008.

[38] A. KASUGAI *et al.* Steady-state operation of 170 GHz 1 MW gyrotron for ITER. *Nucl. Fusion*, 48(5):054009, 2008.

[39] S. B. KORSHOLM *et al.* Fast ion collective Thomson scattering diagnostic for ITER - progress of design. In *BURNING PLASMA DIAGNOSTICS: An International Conference, September 2007*, pages 118–122. American Institute of Physics, September 2007.

[40] S. B. KORSHOLM *et al.* Collective Thomson scattering capabilities to diagnose fusion plasmas. *Nucl. Instr. and Methods in Phys. Res.*, 623:677–680, 2010.

[41] S. B. KORSHOLM *et al.* Measurements of intrinsic ion Bernstein waves in a tokamak by collective Thomson scattering. *Phys. Rev. Lett.*, 106:165004, 2011.

[42] S. B. KORSHOLM *et al.* Current fast ion collective Thomson scattering diagnostics at TEXTOR and ASDEX Upgrade, and ITER plans. *Rev. Sci. Instrum.*, 77(10):10E514, 2006.

[43] A. KRÄMER-FLECKEN, W. PYSIK, and G. CZYMEK. 110 GHz notch-filter development at TEXTOR-94. *Fusion Eng. Des.*, 56-57:639–643, 2001.

[44] S. KUBO *et al.* Collective Thomson scattering of a high power electron cyclotron resonance heating beam in LHD (invited). *Rev. Sci. Instrum.*, 81:10D535, 2010.

[45] THOMAS H. LEE. *The Design of CMOS Radio-Frequency Integrated Circuits*. Cambridge, University Press, The Pitt Building, Trumpington Street, Cambridge, UK, 2004.

[46] F. LEIPOLD *et al.* Antenna design for fast ion collective Thomson scattering diagnostic for the international thermonuclear experimental reactor. *Rev. Sci. Instrum.*, 80:093501, 2009.

[47] F. LEUTERER *et al.* Status of the new ECRH system for ASDEX upgrade. *Fusion Eng. Des.*, 74:199203, 2005.

[48] N. C. LUHMANN *et al.* Microwave diagnostics. *Fusion Sci. Tech.*, 53(2):335–396, 2008.

[49] S. A. MAAS. *Nonlinear Microwave and RF Circuits.* Artech House, Inc., Norwood, MA 02062, 2003.

[50] N. MARCUVITZ. *Waveguide Handbook.* Peter Peregrinus Ltd., London, UK, Brooklyn, N.Y., 1986.

[51] G. MATTHAEI, L. YOUNG, and E. M. T. JONES. *Microwave Filters, Impedance-Matching Networks, and Coupling Structures.* Artech House, 685 Canton Street, Norwood, MA 02062, 1980.

[52] F. MEO *et al.* Design of the collective Thomson scattering diagnostic for international thermonuclear experimental reactor at the 60 GHz frequency range. *Rev. Sci. Instrum.*, 75:3585–3588, 2004.

[53] F. MEO *et al.* Commissioning activities and first results from the collective Thomson scattering diagnostic on ASDEX Upgrade. *Rev. Sci. Instrum.*, 79:10E501, 2008.

[54] F. MEO *et al.* First results and analysis of collective Thomson scattering (CTS) fast ion distribution measurements on ASDEX Upgrade. *J. Phys.: Conf. Series*, 227(1):012010, 2010.

[55] D. MOSEEV *et al.* Comparison of measured and simulated fast ion velocity distributions in the TEXTOR tokamak. *Plasma Phys. Control. Fusion*, 53(10):105004, 2011.

[56] S. K. NIELSEN. *Fast ion dynamics in TEXTOR plasmas measured by means of collective Thomson scattering (CTS).* PhD thesis, Forskningscenter Risø, Technical University of Denmark, August 2007.

[57] S. K. NIELSEN *et al.* Temporal evolution of confined fast ion velocity distributions measured by collective Thomson scattering in TEXTOR. *Phys. Rev. E*, 77:016407, 2008.

[58] S. K. NIELSEN *et al.* Fast-ion redistribution due to sawtooth crash in the TEXTOR tokamak measured by collective Thomson scattering. *Plasma Phys. Control. Fusion*, 52:092001, 2010.

[59] S. K. NIELSEN *et al.* Dynamics of fast ions during sawtooth oscillations in the TEXTOR tokamak measured by collective Thomson scattering. *Nucl. Fusion*, 51(6):063014, 2011.

[60] G. S. NUSINOVICH. *Introduction to the Physics of Gyrotrons.* The John Hopkins University Press, 2004.

[61] J. ONGENA and G. van OOST. Energy for future centuries - prospects for fusion power as a future energy source. *Fusion Sci. Tech.*, 49(2T):3–15, 2006.

[62] F.P. ORSITTO *et al.* Requirements for fast particle measurements on ITER and candidate measurement techniques. *Nucl. Fusion*, 47(9):1311–1317, 2007.

[63] G. PEREZ, T. ESTRADA, G. VAYAKIS, and C. WALKER. Thermal and mechanical analysis of the ITER plasma-position reflectometry antennas. In *Proceeding of the 25th Symposium on Fusion Technology (SOFT-25)*, pages 1488–1494. Fusion Eng. Des., June 2009.

[64] B. PIOSCZYK *et al.* Towards a 2 mw, cw, 170 GHz coaxial cavity gyrotron for ITER. In *22nd Symposium on Fusion Technology*, pages 481–485. Fusion Eng. Des., September 2003.

[65] P. A. RIZZI. *Microwave Engineering - Passive Circuits*. Prentice-Hall, Inc., Englewood Cliffs, New Jersey 07632, 1988.

[66] Bahaa E.A. SALEH and Malvin Carl TECH. *Fundamentals of Photonics*. John Wiley & Sons, 1991.

[67] M. SALEWSKI *et al.* Comparison of collective Thomson scattering signals due to fast ions in ITER scenarios with fusion and auxiliary heating. *Plasma Phys. Control. Fusion*, 51(3):035006, 2009.

[68] M. SALEWSKI *et al.* Impact of ICRH on the measurement of fusion alphas by collective Thomson scattering in ITER. *Nucl. Fusion*, 49(2):025006, 2009.

[69] M. SALEWSKI *et al.* Investigation of first mirror heating for the CTS diagnostic in ITER. *Rev. Sci. Instrum.*, 79:10E729, 2008.

[70] M. SALEWSKI *et al.* Comparison of fast ion collective Thomson scattering measurements at ASDEX Upgrade with numerical simulations. *Nucl. Fusion*, 50(3):035012, 2010.

[71] M. SALEWSKI *et al.* On velocity space interrogation regions of fast-ion collective Thomson scattering at ITER. *Nucl. Fusion*, 51(8):083014, 2011.

[72] E. E. SALPETER. Electron density fluctuations in a plasma. *Phys. Rev.*, 120:1528–1535, 1960.

[73] S. A. SCHELKUNOFF. Theory of antennas of arbitrary size and shape. *Inst. of Electrical and Electronics Eng.*, 72:1165–1190, 1984.

[74] Z. SHEN *et al.* 2-d passive millimeter wave imaging system for plasma diagnostics. In *Proceedings of Asia-Pacific Microwave Conference 2007*, pages 116–119. IEEE, December 2007.

[75] N. SKOU. *Microwave radiometer systems: design and analysis*. Artech House, 685 Canton Street, Norwood, 1989.

[76] M. STEJNER *et al.* Collective Thomson scattering measurements with high frequency resolution at TEXTOR. *Rev. Sci. Instrum.*, 81:10D515, 2010.

[77] M. STEJNER *et al.* Measurements of plasma composition in the TEXTOR tokamak by collective Thomson scattering. *Plasma Phys. Control. Fusion*, 54(1):015008, 2012.

[78] E. V. SUVOROV *et al.* Ion temperature and beam-driven plasma waves from collective scattering of gyrotron radiation in W7-AS. *Plasma Phys. Control. Fusion*, 37(11):1207–1213, 1995.

[79] E. V. SUVOROV *et al.* Collective Thomson scattering at W7-AS. *Plasma Phys. Control. Fusion*, 39(12B):B337–B351, 1997.

[80] U. TARTARI *et al.* Critical issues highlighted by collective Thomson scattering below electron cyclotron resonance in FTU. *Nucl. Fusion*, 46(11):928–940, 2006.

[81] U. TARTARI *et al.* Evolution of the millimeter-wave collective Thomson scattering system of the high-field tokamak Frascati Tokamak Upgrade. *Rev. Sci. Instrum.*, 78:043506, 2007.

[82] M. THUMM *et al.* MW gyrotron development for fusion plasma applications. *Plasma Phys. Control. Fusion*, 45:A143A161, 2003.

[83] M. TIURI. Radio astronomy receivers. *Inst. of Electrical and Electronics Eng.*, 12(7):930–938, December 1964.

[84] E. TSAKADZE *et al.* Fast ion collective thomson scattering diagnostic for ITER: Design elements. *Fusion Sci. Tech.*, 53(1):69–76, January 2008.

[85] G. VAYAKIS *et al.* ECE diagnostics for rto/rc ITER. *Fusion Eng. Des.*, 53(1-4):221–227, 2001.

[86] G. VAYAKIS *et al.* Status and prospects for mm-wave reflectometry in ITER. *Nucl. Fusion*, 46(9):S836, 2006.

[87] D. H. WAGNER *et al.* Commissioning of the second two-frequency gyrotron in the new multi-frequency ECRH system for ASDEX upgrade. In *Infrared and Millimeter Waves, 15th International Conference on Terahertz Electronics*, September 2007.

[88] D. H. WAGNER *et al.* Present status of the new multifrequency ECRH system for ASDEX Upgrade. *IEEE Trans. Plasma Sci.*, 36(2):324–331, 2008.

[89] D. H. WAGNER *et al.* Status of the new multi-frequency ECRH system for ASDEX Upgrade. *Nucl. Fusion*, 48(5):054006, 2008.

[90] E. WESTERHOF *et al.* Electron cyclotron resonance heating on TEXTOR. *Nucl. Fusion*, 43(11):13711383, 2003.

[91] E. WESTERHOF *et al.* Strong scattering of high power millimeter waves in tokamak plasmas with tearing modes. *Phys. Rev. Lett.*, 103:125001, 2009.

[92] P WOSKOBOINIKOW, W. J. MULLIGAN, and R. ERICKSEN. 385 mu-md2o laser linewidth measurements to -60 db. *IEEE Journal of Quantum Electronics*, 19(1):4–7, 1983.

[93] PAUL WOSKOV. Notch filter options for ITER stray gyrotron radiation. *Proceedings of LAPD-13*, 2007.

[94] P. WOSKOW *et al.* Frequency measurements of the gyrotrons used for collective Thomson scattering diagnostics at TEXTOR and ASDEX upgrade. *Rev. Sci. Instrum.*, 77:10E524, 2006.

[95] R. J. WYLDE. Millimetre-wave Gaussian beam-mode optics and corrugated feed horns. *IEE Proceedings-H (Microwaves, Optics and Antennas)*, 131:258–262, 1984.

[96] H. ZIRATH. High-frequency noise and current-voltage characteristics of mm-wave platinum nn+ GaAs schottky barrier diodes. *J. of App. Phys.*, 60(4):1399–1407, 1986.

[97] H. ZOHM *et al.*, ASDEX Upgrade Team, and ECRH Group. Experiments on neoclassical tearing mode stabilization by ECCD in ASDEX upgrade. *Nucl. Fusion*, 39(5):577, 1999.